Università degli Studi di Pavia
Dipartimento di Scienze della Terra e dell'Ambiente

SCUOLA DI ALTA FORMAZIONE DOTTORALE
MACRO-AREA SCIENZE E TECNOLOGIE

DOTTORATO DI RICERCA IN SCIENZE DELLA TERRA E DELL'AMBIENTE

Davide Berno

Early evolution of mantle melts intruding the lowermost oceanic and continental crust: insights from the troctolite-gabbro association of the Pineto ophiolite (Corsica) and the M. Capio ultramafic sill (Ivrea Verbano Zone, Western Alps)

Anno Accademico 2016-2017
Ciclo XXX

Coordinatore
Prof. Roberto Sacchi

Tutor
Prof. Tribuzio Riccardo

Co-tutor(s)
Prof. Alessio Sanfilippo
Prof. Alberto Zanetti

GENERAL INTRODUCTION

This PhD thesis comprises the petrological and geochemical study of two lower crust intrusive sequences displaying mafic-ultramafic compositions and emplaced in an extensional tectonic setting. The purpose is to obtain information about crustal growth by magmatic underplating in extensional tectonic settings, by identification of: (i) the compositions of the mantle melts intruding the crust, and (ii) the early magmatic evolution experienced by these melts. Recent studies have shown that formation of the lower mafic crust is associated with a magmatic evolution controlled not only by fractional crystallization and magma mixing but also by reaction of crystal mushes with migrating melts and crustal assimilation (e.g., Lissenberg and Dick, 2008; Solano et al., 2012).

The selected rock sequences formed in different geological environments. The Pineto gabbroic massif (central Corsica) belongs to the Alpine Jurassic ophiolites and is considered to represent a fossil analogue of the lowermost oceanic crust (Sanfilippo and Tribuzio, 2013; 2015). The evolution of mantle melts intruding the lowermost continental crust has been investigated by selecting the ultramafic magmatic sequence of Monte Capio-Alpe Cevia (Ivrea-Verbano Zone, northern Italy). The growth of the Monte Capio-Alpe Cevia sequence was associated with the late- to post-collisional, extensional phases of the Variscan orogeny (e.g., Klötzli et al., 2014), or with the rifting evolution leading to opening of the Jurassic Alpine Tethys (Denyszyn et al., 2018).

The Pineto gabbroic sequence exposes a unique 1.5 km-thick transect of Jurassic lower oceanic crust (Sanfilippo and Tribuzio 2013). The sequence essentially consists of chemically primitive troctolites and minor olivine gabbros in its lower sector, and moderately evolved gabbros in the upper part. The association of troctolites and olivine gabbros most likely represents the plutonic foundation of a fossil (ultra-)slow-spreading centre. Sanfilippo et al. (2015) proposed that reactive melt migration was a major evolution process active during the growth of the Pineto lower sector. In this thesis, I analyzed the trace element compositions of whole-rocks and minerals for fifteen samples, which were selected mostly based on mineral proportion variations. The processes leading to the partitioning of trace elements among olivine, plagioclase and clinopyroxene were therefore discussed, thereby implying that reactive melt migration is a major, if not the main, evolutionary process active in the deepest oceanic crust. The manuscript I prepared is entitled “Reactive melt migration controls the trace element budget of the lower oceanic crust: insights from the troctolite-olivine gabbro association of the Pineto ophiolite (Corsica, France)”.

Few are the fossil lower continental crustal sections exposed on Earth that may be used as a natural laboratory to study the intrusion and evolution of mantle melts (e.g., Hildreth and Moorbath, 1988; Jagoutz et al., 2006; 2007; Grant et al., 2016). The ultramafic sequence of Monte Capio-Alpe Cevia is the largest magmatic sequence within the lower continental crust of the Ivrea-Verbano Zone. I have carried out a petrological and geochemical study of about twenty samples from this sequence, which mostly consists of peridotites, minor pyroxenites and subordinate gabbronorites. For both whole rocks and minerals, I analyzed major and trace element concentrations, and Nd-Sr isotopic compositions. The results enabled me to depict a scenario for the formation

of the Monte Capio-Alpe Cevia sequence, including the definition of mantle sources and magmatic evolution. The primary melts feeding the sequence most likely originated from a heterogeneous mantle source that had previously experienced subduction-related metasomatism. The magmatic evolution was mainly controlled by reactive migration of evolved melts relatively rich in SiO_2 and H_2O, and, at least locally assimilation of crustal material. The manuscript I prepared is entitled “Evolution of mantle melts intruding the lower continental crust: constraints from the Monte Capio-Alpe Cevia ultramafic sequences (Ivrea-Verbano Zone, northern Italy)”.

Evolution of mantle melts intruding the lower continental crust: constraints from the Monte Capio-Alpe Cevia ultramafic sequences (Ivrea-Verbano Zone, northern Italy)

Tables of Contents

1. Introduction

Understanding the emplacement and evolution mechanisms of mantle-derived melts into the lower continental crust is crucial to shed light on the debate dealing with the growth of the continental crust. Deep magma chambers are most likely the dominant sources of evolved magmas rising at shallow crustal levels to give rise to granitoid bodies (Annen et al., 2006; Müntener and Ulmer, 2006; Solano et al., 2012; Nandedkar et al., 2014). In these magma chambers, the compositions of ascending mantle-derived magmas are modified through complex evolution processes involving fractional crystallization, magma mixing, crustal assimilation and melt-crystal mush reactions. However, only few ultramafic magmatic sequences were used as natural laboratories to investigate the emplacement of mantle-derived melts in the lower continental crust (e.g., Hildreth and Moorbath, 1988; Jagoutz et al., 2006; 2007; Grant et al., 2016). Because of inaccessibility of the lower continental crust, indeed, these ultramafic sequences were rarely observed in nature. In addition, ultramafic rocks from the deep continental crust may have foundered into the mantle by density driven relationships (Jull and Kelemen, 2001; Müntener et al., 2001).

The Ivrea-Verbano Zone from Italian Alps (Italy) exposes a nearly complete, lower continental crustal section (e.g., Schmid et al., 2017). This section is mostly made up of a km-scale thick gabbro-diorite body of Lower Permian age that intruded a granulite to amphibolite facies basement in response to post-collisional extensional tectonics (e.g., Quick et al., 1994; Peressini et al., 2007). Numerous ultramafic bodies inferred to be of intrusive nature occur in the Ivrea-Verbano Zone (Bertolani and Loschi Ghittoni, 1979; Voshage et al., 1990; Rutter et al., 1993; Garuti et al., 2001; Quick et al., 2003; Klötzli et al., 2014). The ultramafic bodies from the intermediate-upper sector of the Ivrea-Verbano Zone, collectively also known as Ultramafic Pipes, have been recently thoroughly investigated from a geochemical viewpoint (Locmelis et al., 2016; Fiorentini et al., 2018). Conversely, comprehensive petrological and geochemical datasets are lacking for the sill-like, magmatic ultramafic bodies from the deepest levels the Ivrea-Verbano zone. The present study focuses on two of these ultramafic sequences, namely the Monte Capio and the Alpe Cevia bodies, which both mostly consist of peridotites and minor pyroxenites. The main purpose is to elucidate the evolution experienced by primitive mantle melts intruding the lower continental crust. We also wish to acquire new constraints on the compositions of the mantle sources leading to igneous accretion in the Ivrea-Verbano Zone. Hence, we present a petrological-geochemical study of the Monte Capio-Alpe Cevia ultramafic sequences, which comprises: (i) petrographic investigations and whole-rock major element analyses; (iii) major and trace element

analyses of minerals; (iv) Nd-Sr isotope analyses on whole-rocks and amphibole separates.

2. Geological framework

The western-central basement of Southern Alps, also referred to as Massiccio dei Laghi, is an almost complete section of the Variscan continental crust (e.g., Schmid et al., 2017). It is composed of two main units: the Ivrea-Verbano Zone (IVZ) and the Serie dei Laghi, which is also referred to as Strona Ceneri Zone. The IVZ represents the lower sector of the continental crust. It essentially consists of a km-scale gabbro-diorite body (Mafic Complex, mostly dated at ~288 Ma, Peressini et al., 2007) intruding a granulite to amphibolite facies basement locally known as Kinzigite Formation (Fig. 1a). To the northwest, the IVZ is in tectonic contact (Insubric Line) with the basement of the Austro-Alpine domain. To the east, the IVZ is tectonically juxtaposed to the Serie dei Laghi, which represents the upper section of the Variscan continental crust (e.g., Boriani et al., 1990; Boriani and Giobbi, 2004).

The Kinzigite Formation mainly consists of amphibolite to granulite facies metasediments (metapelites with subordinate metagreywackes and impure marbles) including minor metabasites and, locally, mantle peridotite blocks (e.g., Quick et al., 1995; Mazzucchelli et al., 2010). This rock association was presumably originally assembled in an accretionary prism of pre-Ordovician age (Guergoz et al., 2018). The regional metamorphic grade of the Kinzigite Formation gradually increases from southeast to northwest. In the IVZ central sector (Val Strona di Omegna), quantitative phase equilibria modelling confined the pressure-temperature conditions of the Kinzigite Formation ranging from ~11 kbar and ~900 °C near the Insubric Line, to 3.5-6.5 kbar and ~650 °C, near the Cossato-Mergozzo-Brissago line (Redler et al., 2012, 2013; Kunz et al., 2014).

The Mafic Complex intrudes the Kinzigite Formation in the central and southern sectors of the IVZ (e.g., Quick et al., 2003). The Mafic Complex was subdivided into the Lower Mafic Complex, mostly composed of amphibole gabbros, and the Upper Mafic Complex (also referred to as Main Gabbro) that mainly consists of gabbronorites and, towards the stratigraphic top, of diorites. The lowest portion of the Upper Mafic Complex includes abundant metasedimentary septa, which typically experienced considerable extraction of SiO2-rich melts (Sinigoi et al., 1996). Bodies made up of peridotites and/or pyroxenites are locally present and mostly included within the gabbronorites. The main phase of Mafic Complex formation occurred at 288 ± 4 Ma, as defined by U-Pb zircon dates (e.g., Peressini et al., 2007), and caused an episode of high temperature metamorphism and anatexis in a 1-2 km aureole (Barboza and Bergantz, 2000). Early magmatic pulses related to formation of the Mafic Complex probably occurred at ~310 Ma

(see also Klötzli et al., 2014). Based on Nd-Sr isotopic compositions, Voshage et al. (1990) proposed that the Mafic Complex originated by variably fractionated MORB-type melts, which experienced different extents of assimilation of crustal material.

Discordant ultramafic magmatic bodies (up to 300 m wide) are also present towards the top of the Ivrea Mafic Complex and within the Kinzigite Formation. These peridotite-pyroxenite sequences, collectively also known as Ultramafic Pipes, are typically relatively rich in amphibole and phlogopite, and contain accessory apatite and magmatic carbonates (Garuti et al., 2001; Locmelis et al., 2016; Fiorentini et al., 2018). Zircon extracted from the Ultramafic Pipes gave dates ranging from 288 to 249 Ma, which were interpreted as intrusion ages. Fiorentini et al. (2018) inferred that the melts feeding the Ultramafic Pipes formed by partial melting of a continental lithospheric mantle that was previously metasomatized in response to the Variscan subduction.

Along the northern sector of the Ivrea Mafic Complex (Fig. 1b), near the Insubric Line, sill-like peridotite-pyroxenite bodies are exposed (Bertolani and Loschi Ghittoni, 1979; Rutter et al., 1993; Quick et al., 2003). The present study focuses on two of these ultramafic lenses, namely the Monte Capio and the Alpe Cevia bodies. These ultramafic bodies show intrusive relationships with respect to granulite facies metasediments of the Kinzigite Formation, and in places include Ni-Fe-Cu sulphide mineralizations (Ferrario et al., 1983; Zaccarini et al., 2014). Based on geometric relationships, Klötzli et al. (2014) suggested a correlation between these ultramafic sill-like bodies and ultramafic rocks interlayered with the metasedimentary septa of the Mafic Complex. In addition, Klötzli et al. (2014) proposed an intrusion age of 314 ± 5 Ma, based on laser ablation ICP-MS U-Pb analyses of zircons extracted from an amphibole-garnet gabbro considered to be genetically related to the peridotite-pyroxenite sequences. Conversely, Denyszyn et al. (2018) have recently supported an age of ~200 Ma for the Monte Capio sequence, based on U-Pb zircon analyses by isotope dilution TIMS. We cannot exclude, nonetheless, that this age represents the product of zircon recrystallization rather than the age of magmatic crystallization. For other deep sectors of the IVZ, it was shown that prolonged residence at depths produced perturbation of the U-Pb isotope system in zircons, thereby leading to apparent age rejuvenation (e.g., Peressini et al., 2007; Zanetti et al., 2016).

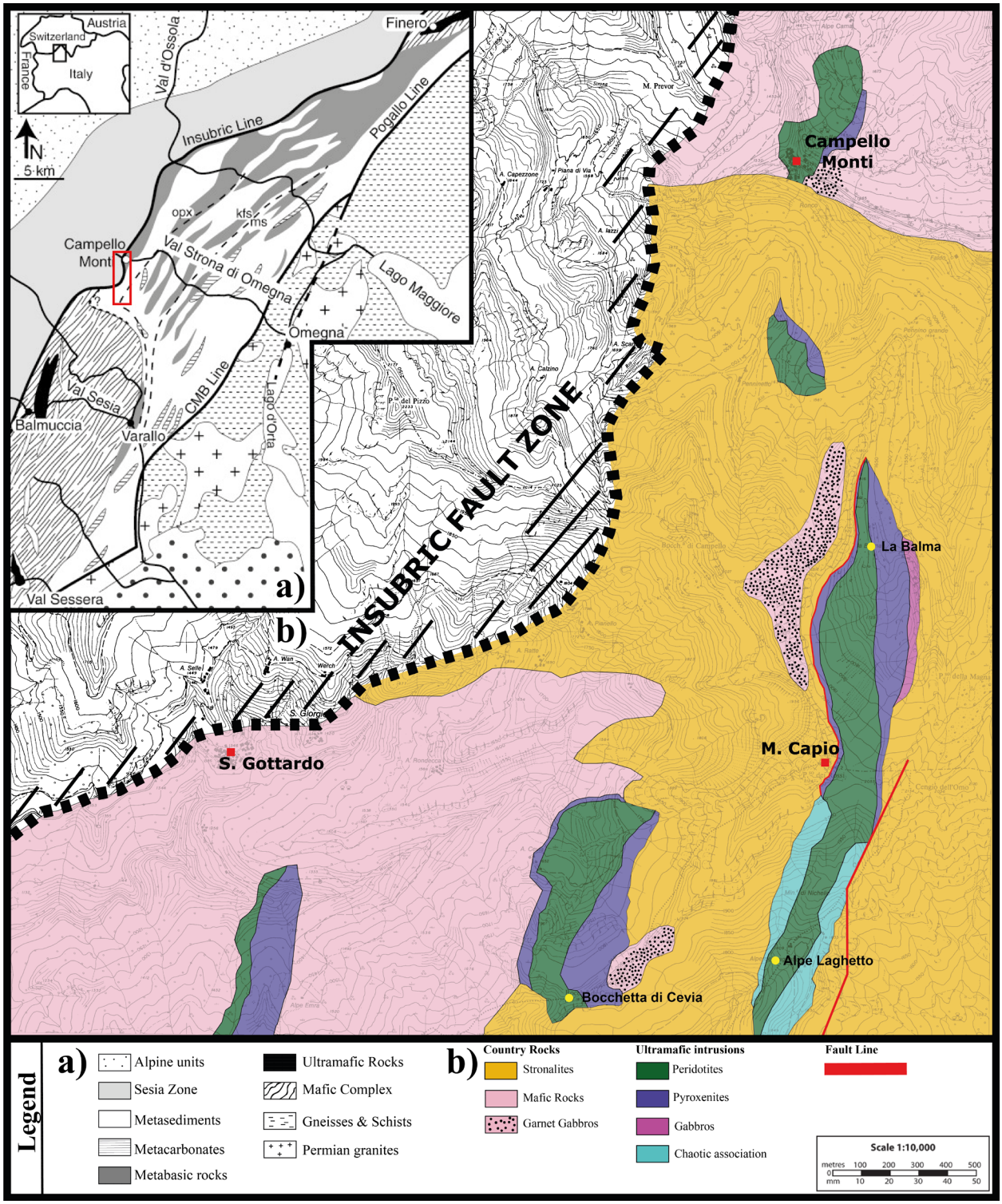

Figure 1: a) Simplified geological map of the Ivrea-Verbano Zone (modified from KUNZ ET AL., 2003). b) Geological sketch map of the Monte Capio area.

3. Field relationships

The Monte Capio body is exposed from La Balma to Monte Capio and Alpe Laghetto localities, with a length of ~2.5 km and an average width of ~0.3 km (Fig. 1b). At La Balma, the Monte Capio body displays a peridotite core bounded by minor pyroxenites (see also Ferrario et al., 1983, and Rutter et al., 1993). The peridotite core consists of up to 30 m thick dunites surrounded by pyroxene-bearing peridotites. In the eastern side of the La Balma sequence, the pyroxenites are typically plagioclase-bearing and grade into minor hornblende gabbronorites that locally intrude the granulite facies basement rocks (see also Denyszyn et al., 2018). The pyroxenites exposed along the western side of the La Balma sequence are in tectonic contact with the granulite facies basement rocks. Near Monte Capio, the width of the pyroxenite edges is reduced to few metres. At Alpe Laghetto, the peridotite core is bounded by a chaotic association of pyroxenites, hornblende gabbronorites and granulite facies basement rocks. The Alpe Cevia peridotite-pyroxenite body has a north-south length of ~300 m and a west-east width of ~200 m. Similar to the Monte Capio body, the Alpe Cevia association of dunites and pyroxene-bearing peridotites has pyroxenite edges.

The peridotites and pyroxenites from both Monte Capio and Alpe Cevia bodies are frequently crosscut by hornblendite veins (typically <2 cm thick) showing sinuous to planar boundaries (Fig. 2). Hornblende-rich gabbros (characteristically 0.1-0.5 m thick) also occur and display sharp planar contacts against host peridotites and pyroxenites. Within the western side of the La Balma sequence, hornblende gabbronorite dykes were also found. Both hornblende-rich gabbro and hornblende gabbronorite dykes in places crosscut the hornblendite veins and possess a magmatic layering defined by amphibole-plagioclase modal variations. The hornblende gabbronorite dykes also show a foliation defined by the preferred orientation of amphibole and plagioclase.

The granulite facies basement rocks exposed in the study area are typically garnet-rich and quartz-rich, and sillimanite- and rutile-bearing, and referred to as stronalites in the literature (e.g., Schnetger, 1994; Redler et al., 2012; Ewing et al., 2013). These metasedimentary rocks in places include metre-scale, impure marble layers. The basement rocks at the western side of the La Balma sequence host a body (up to tens of metres in scale in thickness) made up of amphibole-garnet gabbros. Amphibole-garnet gabbros were also found in contact with the pyroxenites at the eastern border of the Alpe Cevia body.

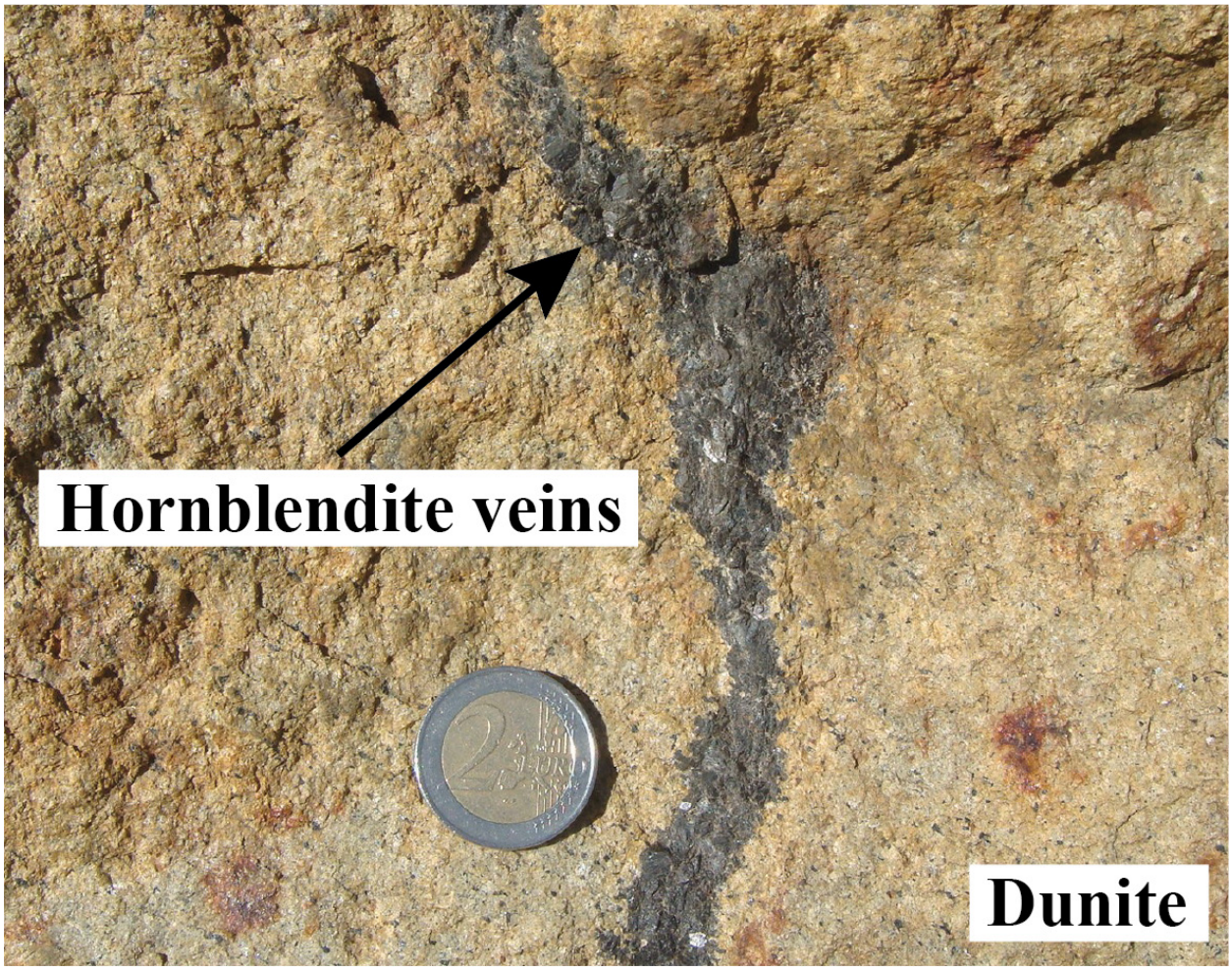

Figure 2: Sinuous hornblendite vein crosscutting dunite from the Monte Capio body (45°54'51.90"N and 8°14'32.53"E).

4. Selected samples and their whole rock major element compositions

We did not find any systematic variation in structural, micro-structural or chemical characteristics between samples collected from Monte Capio and Alpe Cevia bodies. Samples selected for the chemical investigations include eight peridotites (four dunites and four pyroxene-bearing peridotites), six pyroxenites, one hornblendite vein, three hornblende-rich gabbro dykes and two hornblende gabbronorite dykes. Table 1 reports the main petrographic characteristics and localization (GPS coordinates) of selected samples. Whole-rock major element analyses (Table 2) were carried out by inductively coupled plasma (ICP) optical emission spectroscopy at Activation Laboratories (Ancaster, Ontario). Precision and accuracy are better than 2% for SiO_2, Al_2O_3, Fe_2O_3 and MgO, and better than 5% for other elements. Details about analytical technique and detection limits are available from the company website.

4.1 Peridotites

Dunites (AC1D, BC4A, MC27B and MC27/1A) are characterized by olivine polygonal grains (2-3 mm) defining a granoblastic structure (Fig. 3a). These rocks include up to 5 vol% amphibole, which is interstitial with respect to olivine or develops nearly equant grains forming 120° triple junctions with olivine, and accessory euhedral to subhedral brown spinel and sulphides. Accessory orthopyroxene and clinopyroxene with nearly equant morphology are also locally present in dunites.

Samples collected as pyroxene-bearing peridotites during field investigations (MC8/3, MC8/1, MC25A, BC5B) are indeed dunites to lherzolites according to the IUGS nomenclature (Table 1). For the sake's of simplicity, we continue referring to these samples as pyroxene-bearing peridotites. These rocks display a granoblastic structure defined by olivine and pyroxene (up to 25 vol%) grains with polygonal morphology. Amphibole occurs in relatively high modal amounts (5-15 vol%) in pyroxene-bearing peridotites and has typically nearly equant morphology (Fig. 3b). Amphibole is also present within clinopyroxene grains, as thin lamellae subparallel to clinopyroxene cleavages and as irregular patches that are characteristically hundreds of μm in size (Fig. 3c). Pyroxene-bearing peridotites in addition include euhedral to subhedral brown spinel and sulphides.

Dunites and pyroxene-bearing peridotites show Mg# [molar $Mg/(Mg+Fe^{2+}_{tot}) \times 100$] values of 84-81 and low contents of SiO_2, Al_2O_3, CaO and TiO_2 (Fig. 4). Pyroxene-bearing peridotite BC5B is distinct in the relatively high SiO_2, Al_2O_3, CaO and TiO_2, which reflect the high modal proportions of clinopyroxene and amphibole (both ~15 vol%).

	Sample Initials	Mineral modes (%)						Avarage Grain size (mm)				Opaques	Nomenclature	Location	Coordinates
		Ol	Opx	Cpx	Amp	Pl	Opaques	Ol	Opx	Amp	Pl				
Dunites	AC1D	95	-	-	§	-	5	3	-	0.5	-	Sulphides + Spl	Hornblende-bearing Dunite	Alpe Cevia Body	45°54'21.2"N 8°13'28.3"E
	BC4A	95	-	§	§	-	5	2	-	0.5	-	Sulphides + Spl	Hornblende-bearing Dunite	Alpe Cevia Body	45°54'02.0"N 8°13'22.8"E
	MC27B	90	§	-	5	-	5	3	-	0.5	-	Sulphides + Spl	Hornblende-bearing Dunite	Monte Capio Body	45°54'51.0"N 8°14'32.9"E
Px-bearing peridotites	MC8/3	85	5	-	5	-	5	2	1	1	-	Sulphides + Spl	Hornblende-bearing Dunite	Monte Capio Body	45°55'03.1"N 8°14'25.4"E
	MC8/1	85	-	5	5	-	5	2	1	1	-	Sulphides + Spl	Hornblende-bearing Dunite	Monte Capio Body	45°55'04.7"N 8°14'25.4"E
	MC25A	75	10	5	5	-	5	2	1	0.5	-	Sulphides + Spl	Hornblende-bearing Lherzolite	Monte Capio Body	45°55'06.3"N 8°14'34.8"E
	BC5B	60	10	15	15	-	§	2	1	0.5	-	Sulphides + Spl	Hornblende Lherzolite	Alpe Cevia Body	45°54'02.8"N 8°13'23.2"E
Pl-free pyroxenites	MC8B	10	30	15	40	-	5	1	up to 3	up to 3	-	Sulphides	Hornblende Olivine Websterite	Monte Capio Body	45°55'04.7"N 8°14'25.4"E
	MC22A	5	75	5	10	-	5	1	up to 2	up to 2	-	Sulphides + Spl	Hornblende Olivine Websterite	Monte Capio Body	45°54'16.3"N 8°14'19.8"E
	MC20/1	-	70	20	5	-	5	-	3	0.5	-	Sulphides + Spl	Hornblende Websterite	Monte Capio Body	45°55'08.4"N 8°14'33.1"E
Pl-bearing pyroxenites	BC2A	-	75	5	10	5	5	-	up to 4	0.5	0.5	Sulphides + Spl	Hornblende Plagioclase Orthopyroxenite	Alpe Cevia Body	45°54'03.2"N 8°13'28.3"E
	MC26A	-	70	5	10	10	5	-	up to 4	0.5	0.5	Sulphides	Hornblende Plagioclase Orthopyroxenite	Monte Capio Body	45°55'03.4"N 8°14'35.6"E
	MC24A	-	60	§	25	10	5	-	1	0.5	0.5	Sulphides + Spl	Hornblende Plagioclase Orthopyroxenite	Monte Capio Body	45°55'10.3"N 8°14'36.5"E
Hornblendite vein	MC27/1 B	-	15	-	80	-	5	1	1	2	-	Sulphides + Spl	Plagiolcase-bearing Pyroxene Hornblendite	Monte Capio Body	45°54'51.0"N 8°14'32.9"E
Hbl-rich gabbros	MC20/2	-	-	-	90	10	-	-	-	3	2	Sulphides + Fe-Ti-oxides	Hornblende Gabbro	Monte Capio Body	45°55'08.4"N 8°14'33.1"E
	AC1B	-	-	-	80	20	-	-	-	3	2	Sulphides + Fe-Ti-oxides	Hornblende Gabbro	Alpe Cevia Body	45°54'21.2"N 8°13'28.3"E
	MC4B	-	-	-	85	15	-	-	-	3	2	Sulphides + Fe-Ti-oxides	Hornblende Gabbro	Monte Capio Body	45°55'14.8"N 8°14'30.2"E
Hbl gabbronorites	MC27A	-	15	5	55	25	§	-	1	up to 3	1.5	Sulphides + Fe-Ti-oxides	Hornblende Gabbronorite	Monte Capio Body	45°54'51.0"N 8°14'32.9"E
	MC7/4	-	15	10	45	30	-	-	1	1	1.5	Sulphides + Fe-Ti-oxides	Hornblende Gabbronorite	Monte Capio Body	45°55'08.9"N 8°14'30.9"E

Table 1: Location and main petrographic characteristics of selected samples. Mineral modes are visually estimated (vol%); § <3 vol%, - mineral not present. Mineral abbreviations after WHITNEY AND EVANS (2010) and rock nomenclature after STRECKEISEN (1967). Coordinates are in WSGS. Dunite MC27/1A is physically associated (within the same thin section) to hornblendite vein MC27/1B.

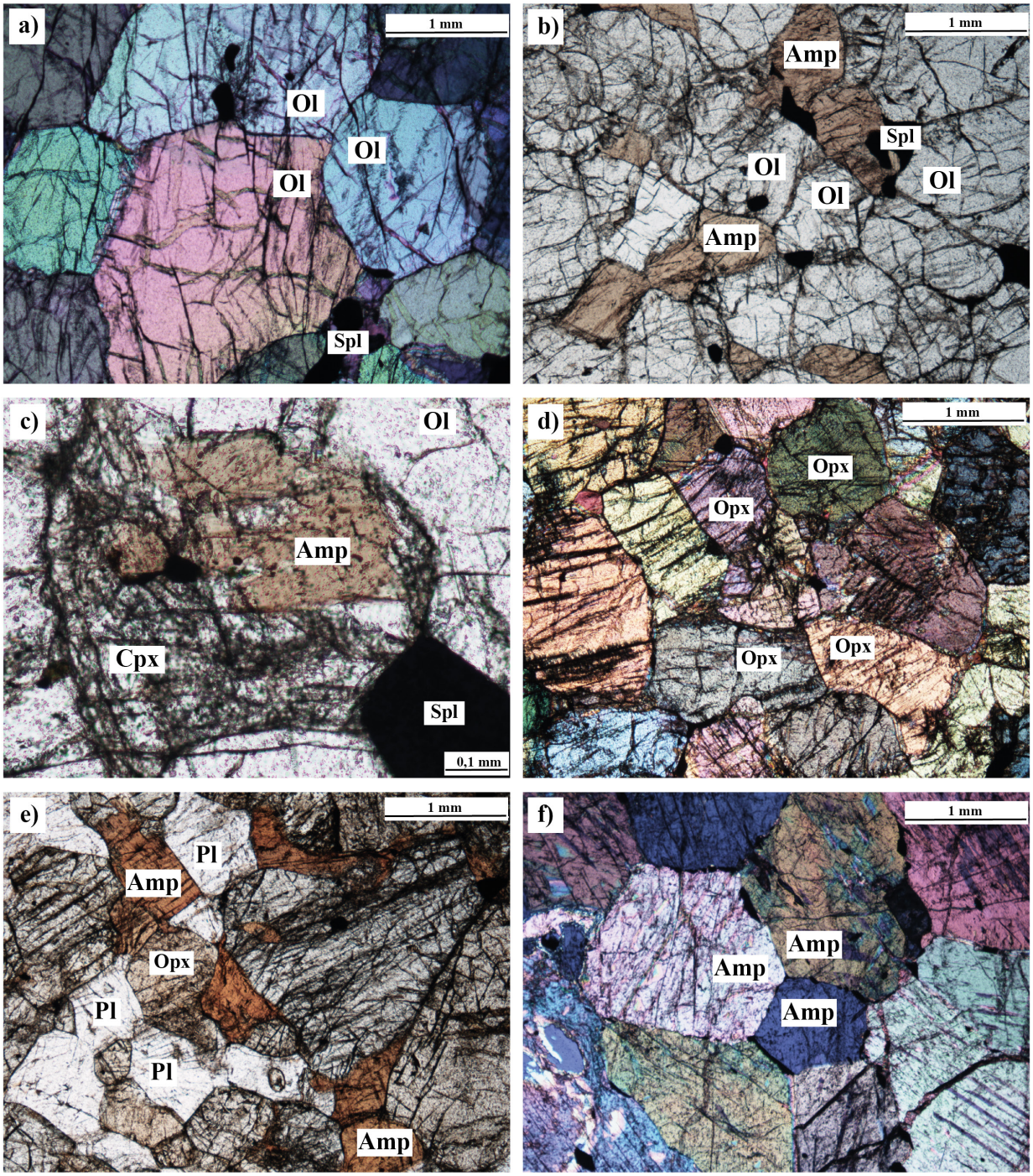

Figure 3: Relevant microstructures. a) olivine-rich matrix displaying granoblastic structure in dunite AC1D. b) olivine and amphibole forming nearly granoblastic structure in pyroxene-bearing peridotite MC25A. c) clinopyroxene grain partially replaced by amphibole in pyroxene-bearing peridotite MC8/1. d) orthopyroxene-rich matrix displaying granoblastic structure in plagioclase-free pyroxenite MC20/1. e) orthopyroxene, amphibole and plagioclase forming nearly granoblastic structure in plagioclase-bearing pyroxenite MC26A. f) amphibole-rich matrix displaying granoblastic structure in hornblende-rich gabbro MC20/2. Mineral abbreviations after WHITNEY AND EVANS (2010).

4.2 Pyroxenites

Pyroxenites were subdivided into two groups based on the presence or absence of plagioclase. Plagioclase-free pyroxenites (MC8B, MC22A and MC20/1) include up to 10 vol% olivine, whereas plagioclase-bearing (up to 10 vol%) pyroxenites (BC2A, MC26A and MC24A) are olivine-free. Taken as a whole, the pyroxenites display a medium grained granoblastic structure (Figs. 3d and 3e), with orthopyroxene and amphibole (30-75 vol% and 5-40 vol%, respectively) more abundant than clinopyroxene. Coarse grained orthopyroxene grains (up to 8 mm in length) are locally present in the pyroxenites, and mantled by granoblastic orthopyroxene aggregates. Brown spinel and sulphides typically occur as euhedral to subhedral mineral accessories.

The pyroxenites typically have slightly lower Mg# (80-77), and higher SiO_2, $Al2O_3$, CaO and TiO_2 than the peridotites (Fig. 4). Plagioclase-free pyroxenite MC8B displays the highest contents of CaO, TiO_2 and Na_2O, in response to the high modal proportion of amphibole (~40 vol%). This sample is also distinct in the relatively low SiO_2, which reflects the relatively high amounts of both amphibole and olivine (10 vol%).

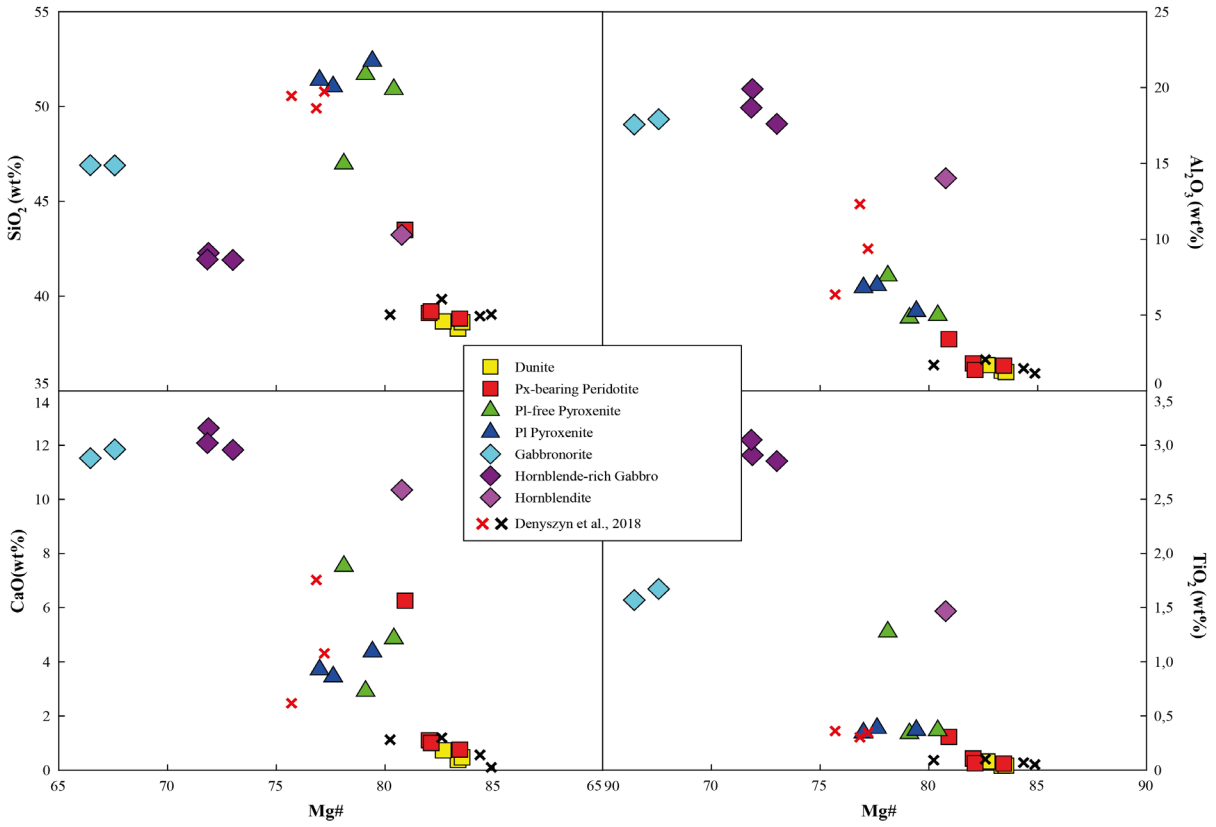

Figure 4: Diagrams showing the whole rock major element variations of selected samples. CaO, SiO_2, Al_2O_3 and TiO_2, calculated on anhydrous basis, versus Mg# [molar $Mg/(Mg+Fe^{2+}_{tot}) \times 100$]. The compositions of dunites and pyroxenites from Monte Capio body reported in DENYSZYN ET AL. (2018) are also plotted.

4.3 Veins and dykes

Selected hornblendite vein (MC27/1B) has Mg# of 81 (Fig. 4) and mostly consists of medium-grained nearly equant amphibole (~80 vol%) and orthopyroxene (~15 vol%), which define granoblastic structure (Fig. 3f). Accessory green spinel and sulphides are also present in the hornblendite. A spinel-bearing orthopyroxenite layer (2 mm thick) separates the hornblendite vein from the host dunite (Fig. 5a).

The hornblende-rich gabbro dykes (MC20/2, AC1B and MC4B) are made up of nearly equant amphibole (up to 90 vol%, 2-3 mm) and plagioclase (10-20 vol%, 1-2 mm) grains forming granoblastic aggregates. At hand sample and thin section scale, plagioclase locally shows an anhedral morphology with respect to amphibole (Fig. 5b), reminiscent of an original hypidiomorphic structure of magmatic origin. The anhedral plagioclases indeed consist of plagioclase polygonal grains defining a granoblastic structure. Accessory Fe-Ti-oxide phases and sulphides are also present in hornblende-rich gabbros. These rocks have Mg# of 73-72 and high contents of Al_2O_3, CaO, TiO_2 and Na_2O (Fig. 4, Table 2).

The hornblende gabbronorite dykes (MC27A and MC7/4) are medium grained and display granoblastic structure (Fig. 5c). These rocks consist of amphibole (~50 vol%), plagioclase (up to 30 vol%), orthopyroxene (~15 vol%) and clinopyroxene (up to 10 vol%), and include accessory Fe-Ti-oxide phases and sulphides. Amphibole and plagioclase locally preserve euhedral to subhedral morphologies. These rocks have lower Mg# (68-66) and TiO_2, and higher SiO_2 than the hornblende-rich gabbros (Fig. 4).

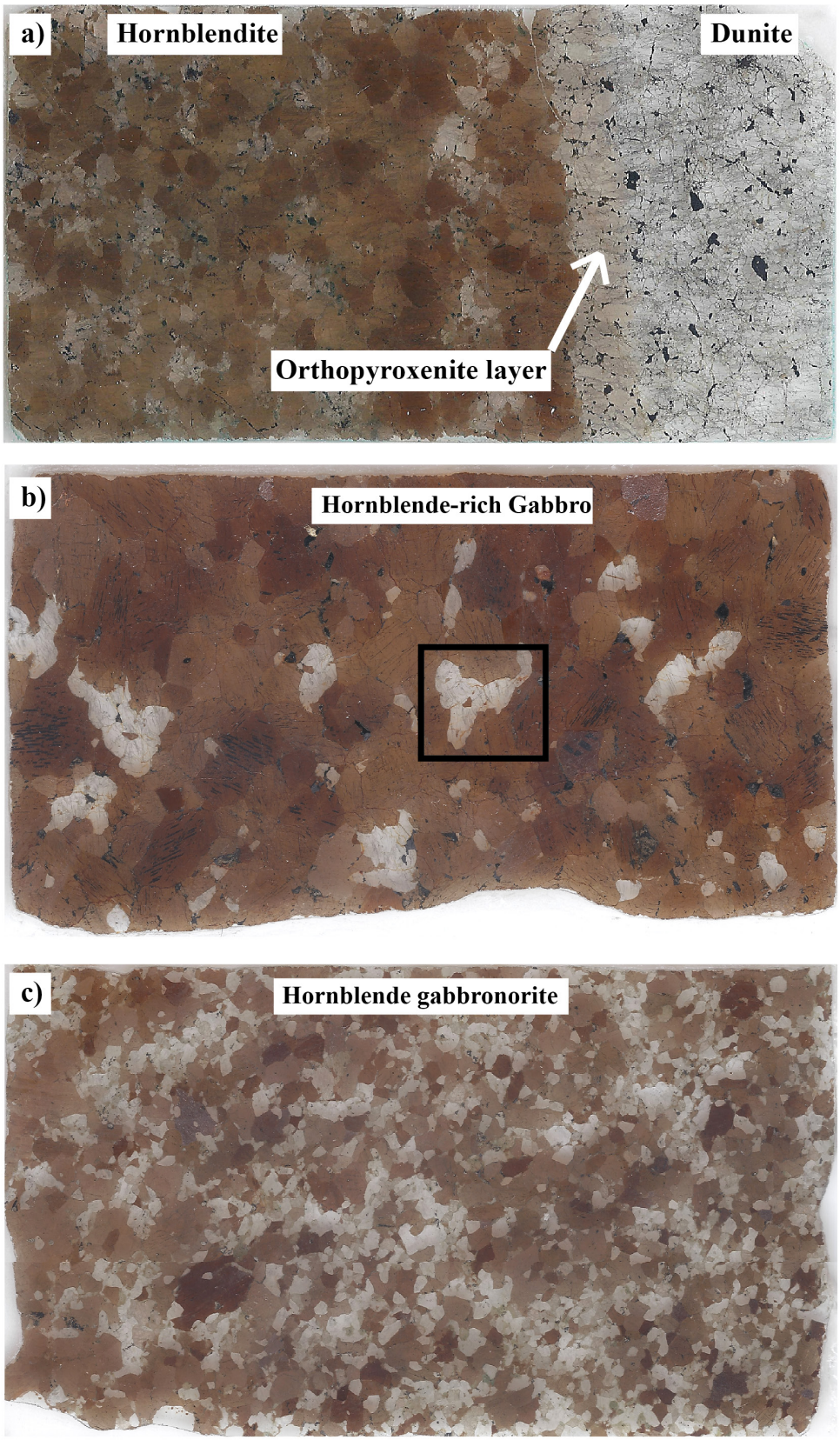

Figure 5: Thin section (2.6 mm x 4.6 mm) images of: a) hornblendite vein MC27/1B and its host dunite; along the contact between the two rock types, a spinel-bearing orthopyroxenite layer occurs. b) hornblende-rich gabbro MC4B, which consists of amphibole and plagioclase forming granoblastic aggregates; the enclosed area shows the original anhedral morphology of magmatic plagioclase. c) hornblende gabbronorite MC27/A displaying granoblastic structure.

5. Major element mineral chemistry

The main mineral phases (olivine, orthopyroxene, clinopyroxene, amphibole, spinel and plagioclase) were analyzed for Si, Ti, Al, Cr, Fe, Mn, Ni, Mg, Ca, Na and K (Table 3) by electron microprobe (JEOL 8200 Super Probe) at Dipartimento di Scienze della Terra, Università degli Studi di Milano, in wavelength-dispersive spectrometry mode. The analyses were carried out at the cores of the grains. Electron microprobe operating conditions were 15 kV accelerating voltage and 15 nA beam current, with counting times of 30 s on the peaks and 10 s on the backgrounds; natural silicates were used as standards.

5.1 Olivine

The forsterite proportion of olivine (Fig. 6) decreases from the dunites (84 to 83 mol%) to the pyroxene-bearing peridotites (83-80 mol%) and the plagioclase-free pyroxenites (78 mol%). The concentrations of NiO and MnO in olivine (≤0.14 wt% and 0.18-0.27 wt%, respectively) do not yield significant correlations with the forsterite proportion; CaO is ≤0.04 wt% (Table 3).

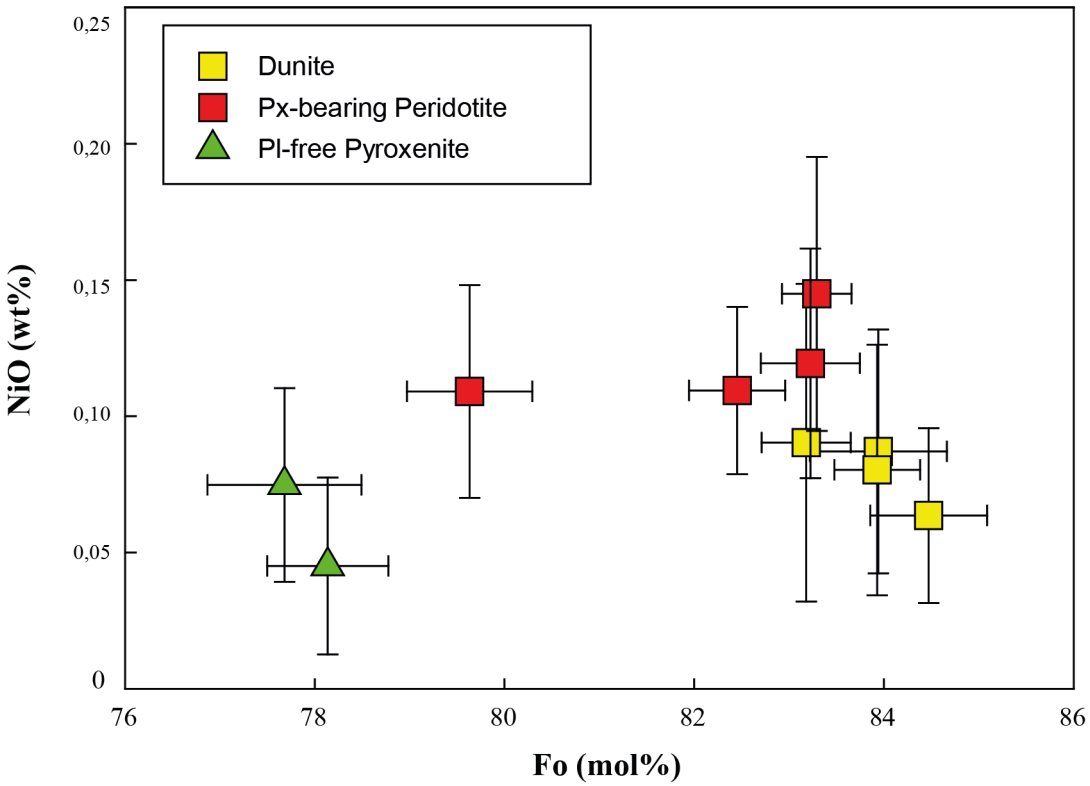

Figure 6: Plot of NiO (wt%) versus forsterite content (mol%) of olivine. Data are averaged per sample. Error bars denote the compositional within-sample variations and represent the standard deviation of the mean value.

5.2 Orthopyroxene

Orthopyroxene has Mg# [100 × Mg/(Mg+Fe2+$_{tot}$)] ranging from 84 to 81 in the dunites and the pyroxene-bearing peridotites, and from 81 to 78 in the pyroxenites (Fig. 7). Orthopyroxene from these rocks shows Al_2O_3 roughly increasing from 1.9 to 5.1 wt% with decreasing Mg#. Within a single pyroxenite, orthopyroxene in granoblastic aggregates and coarse grained orthopyroxene shows similar compositions. Orthopyroxene from the hornblendite vein has higher Mg# and Al_2O_3 (83 and 4.4 wt%) than orthopyroxene from the gabbronorite dykes (73-68 and 3.1-2.2 wt%). The CaO content in all orthopyroxenes is 0.3-0.5 wt%.

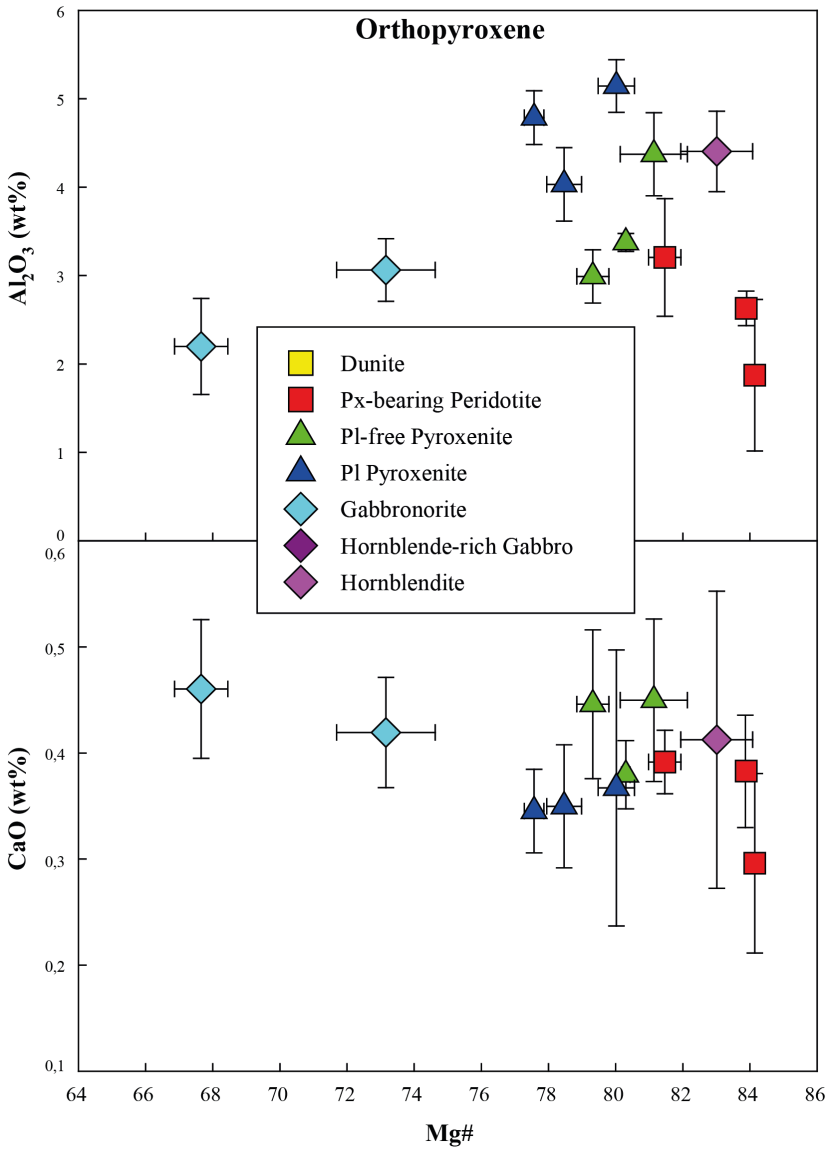

Figure 7: Plot of Al_2O_3 and CaO (wt%) versus Mg# [molar Mg/(Mg+Fe^{2+}_{tot}) × 100] of orthopyroxene. Data are averaged per sample. Error bars denote the compositional within-sample variations and represent the SD of the mean value.

5.3 Clinopyroxene

Clinopyroxene has Mg# ranging from 92 to 88 in the dunites and the pyroxene-bearing peridotites, and from 89 to 85 in the pyroxenites (Fig. 8). The contents of Al_2O_3, TiO_2 and Na_2O in clinopyroxene from these rocks (1.7-5.5 wt%, 0.3-0.9 wt% and 0.1 to 0.4 wt%, respectively) depict rough negative correlations with Mg#; Cr_2O_3 ranges from 0.1 to 0.5 wt%, with no correlation with Mg#. Clinopyroxene from gabbronorite MC7/4 shows the lowest Mg# and Cr_2O_3 (78 and 0.05 wt%) and the highest Na_2O (0.7 wt%).

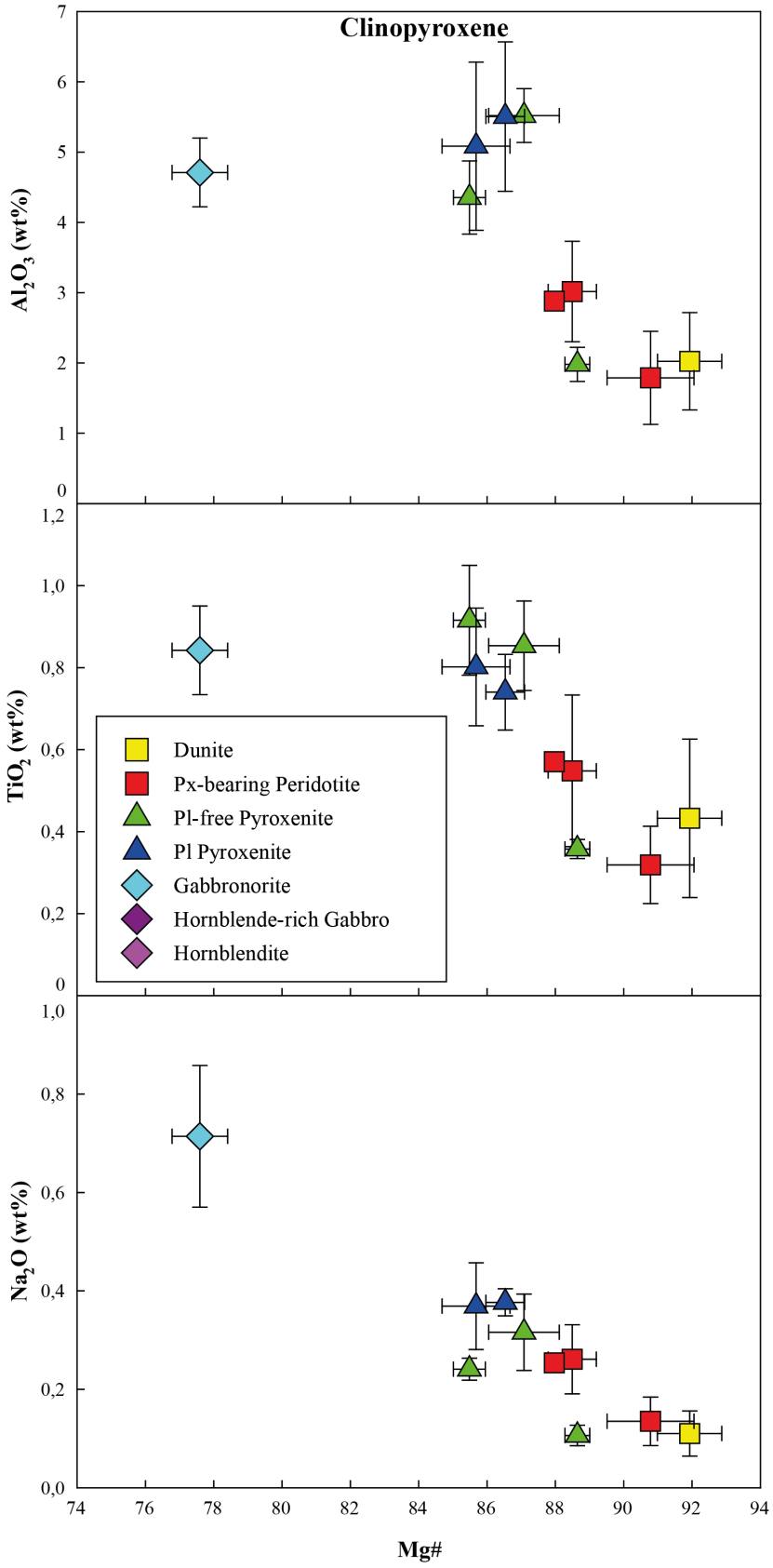

Figure 8: Plot of Al_2O_3, TiO_2 and Na_2O (wt%) versus Mg# [molar Mg/(Mg+Fe^{2+}_{tot}) × 100] of clinopyroxene. Data are averaged per sample. Error bars denote the compositional within-sample variations and represent the standard deviation of the mean value.

5.4 Amphibole

The Mg# of amphibole ranges from 85-82 in the dunites and the pyroxene-bearing peridotites, to 81-77 in the pyroxenites (Fig. 9). Amphibole from the hornblendite vein has higher Mg# (82) than amphibole from hornblende-rich gabbro and hornblende gabbronorite dykes (75-74 and 72-66, respectively). Amphibole from the dunites, the pyroxene-bearing peridotites and the pyroxenites shows Al_2O_3 contents roughly increasing from 12.9 to 15.4 wt% with decreasing Mg#. Conversely, amphibole from the hornblende-rich gabbros and the hornblende gabbronorites depicts a coarse negative correlation between Mg# and Al_2O_3, which in turn ranges from 15.6 to 13.7 wt%. Taken as a whole, TiO_2 and Na_2O contents in amphibole (1.3-3.1 wt% and 1.9-2.8 wt%, respectively) roughly increase with decreasing Mg#. Amphibole from pyroxene-bearing peridotite MC8/1 is distinct in the relatively high K_2O (0.9 wt% vs. 0.2-0.6 wt% in amphibole from other samples).

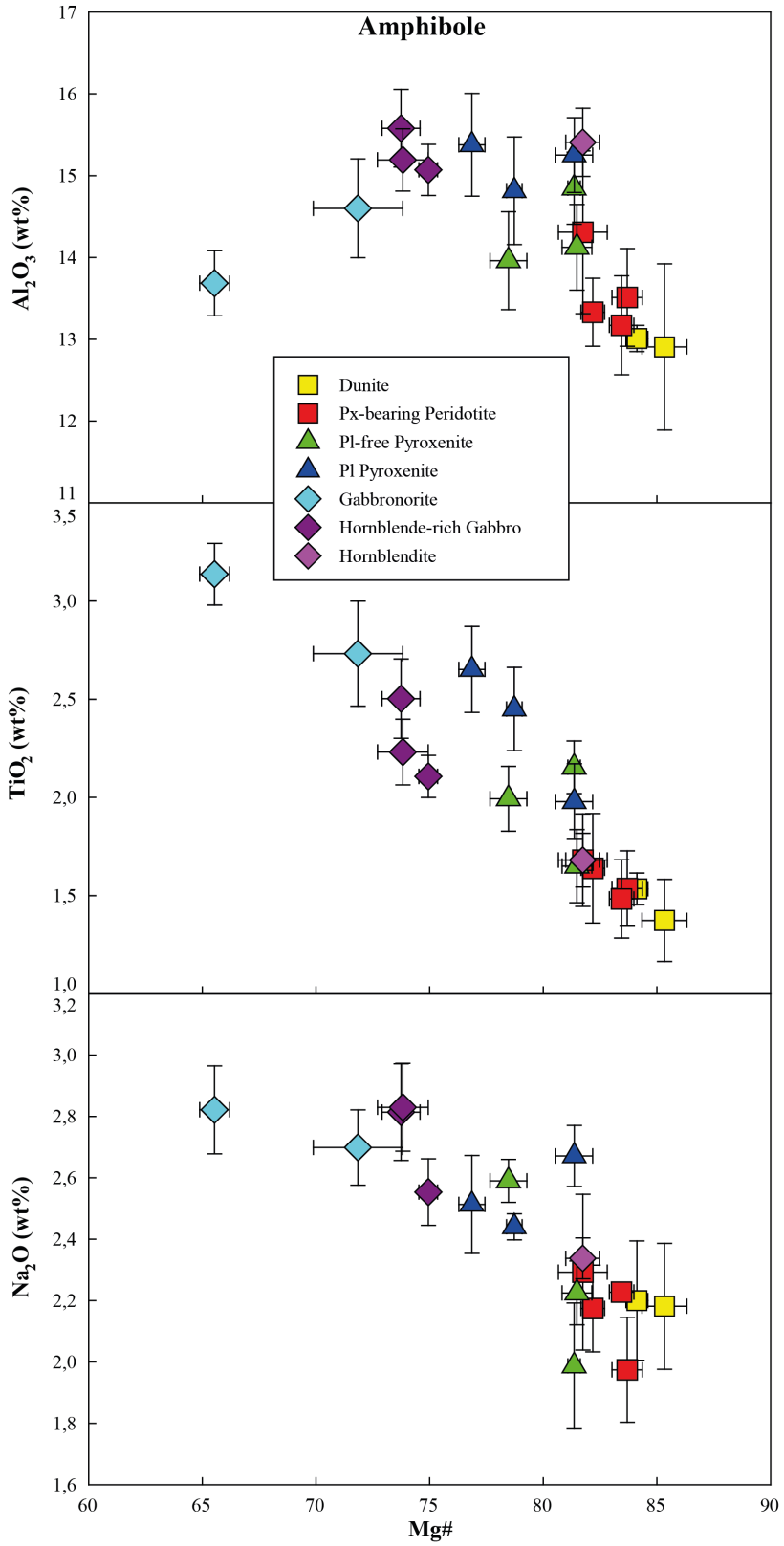

Figure 9: Plot of Al_2O_3, TiO_2 and Na_2O (wt%) versus Mg# [molar $Mg/(Mg+Fe^{2+}_{tot}) \times 100$] of amphibole. Data are averaged per sample. Error bars denote the compositional within-sample variations and represent the standard deviation of the mean value.

5.5 Spinel

Spinel was analyzed in the dunites, the pyroxene-bearing peridotites and the plagioclase-free pyroxenites. It is characterized by low Cr# [100 × Cr/(Cr+Al)] of 7 to 24 (Fig. 10), and Mg# varying from 44 to 58 (Table 3). TiO_2 and NiO contents in spinel are 0.04-0.31 wt% and ≤0.15 wt%, respectively.

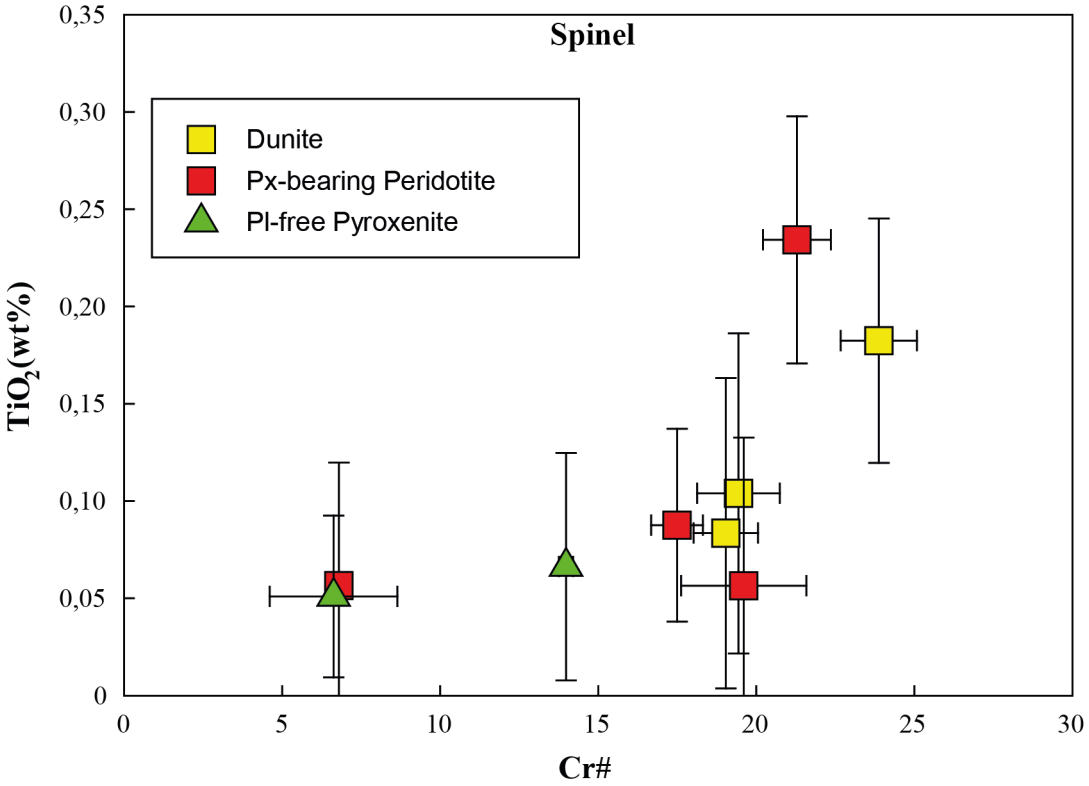

Figure 10: Plot of TiO_2 (wt%) versus Cr# [molar Cr/(Cr+Al) × 100] of spinel. Data are averaged per sample. Error bars denote the compositional within-sample variations and represent the standard deviation of the mean value.

5.6 Plagioclase

Plagioclase from the plagioclase-bearing pyroxenites and the hornblende-rich gabbro dykes have similarly high anorthite proportion (91-88 mol% and 92-84 mol%, respectively; Table 3). Plagioclase from the hornblende gabbronorite dykes shows 76-65 mol% anorthite component.

6. Geothermometric evaluations

We applied the Ca-in-Opx geothermometer of Brey and Kohler (1990) to the four peridotite/pyroxenite samples including orthopyroxene, olivine, clinopyroxene and spinel (Table 4). We obtained *subsolidus* temperature estimates ranging from 803 to 866 °C, which are consistent with the notion that the Monte Capio-Alpe Cevia ultramafic sequences experienced slow cooling in the lower continental crust. We also used the amphibole-plagioclase geothermometer of Holland and Blundy (1994) to the plagioclase-bearing pyroxenites and the hornblende-rich gabbro and hornblende gabbronorite dykes, and we obtained temperature values ranging from 905 to 980 °C. We propose that the Ca-in-Opx geothermometer of Brey and Kohler (1990) has a lower closure temperature than the amphibole-plagioclase geothermometer of Holland and Blundy (1994). We finally applied the amphibole geothermometer of Putirka (2016) to all samples, based on equation 6, thereby yielding relatively high values, ranging from 967 to 1021 °C.

7. Trace element amphibole and clinopyroxene chemistry

Trace element analyses of amphibole and clinopyroxene cores (Tables 4 and 5) were carried out using laser ablation ICP mass spectrometry at Istituto di Geoscienze e Georisorse - C.N.R., Unità di Pavia. The laser probe consisted of a Q-switched Nd:YAG laser, model Quantel (Brilliant), whose fundamental emission in the near-IR region (1064 nm) was converted into 213 nm wavelength using three harmonic generators (Jeffries et al., 1998). Spot diameter was typically ~40 μm. The ablated material was analyzed by using an Elan DRC-e quadrupole mass spectrometer. Helium was utilized as carrier gas and mixed with Ar downstream of the ablation cell. NIST SRM 610 was used as external standard. The CaO content determined by electron microprobe was utilized as internal standard, scaled on the $^{44}Ca^{+}$ signal. Precision and accuracy were assessed from repeated analyses of the BCR2-g standard and resulted better than 10% at ppm concentration level. Detection limits were characteristically in the range of 1.0-0.5 ppm for Cr and Ti, 0.5-0.1 ppm for Sc, 100-10 ppb for Sr, Zr, Ba, Rb, V and Gd, 10-1 ppb for Y, Nb, REE, Hf and Ta.

7.1 Amphibole

Chondrite-normalized REE patterns of amphiboles from the dunites and the pyroxene-bearing peridotites are characterized by nearly flat MREE and HREE (Gd_N/Yb_N = 1.0-1.4, for Yb_N = 22-47), no evident Eu anomaly and LREE that are slightly depleted to slightly enriched with respect to MREE-HREE (e.g., La_N/Sm_N = 0.5-2.0, for Sm_N = 28.5-50.4; Fig. 11). The concentrations of Rb, Th, U and Pb in amphiboles from these rocks vary by up to two orders of magnitude. In particular, amphiboles from dunite BC4A and pyroxenite-bearing peridotite MC8/1 have the lowest and the highest concentrations of Rb, Th, U and Pb, respectively. Normalization of incompatible elements to primordial mantle concentrations shows that amphiboles from the dunites and the pyroxene-bearing peridotites typically displays slight Ba enrichment and slight to moderate Nb and Ta depletion with respect to LREE. The concentrations of Cr, Ni and Sc in amphiboles from the peridotites are 2800-5900 ppm, 160-330 ppm and 110-210 ppm.

Amphiboles from the pyroxenites show nearly homogeneous incompatible trace element compositions, with the exception of amphibole from plagioclase-free pyroxenite MC22A, which is distinct in the high concentrations of Rb, Th, U, Pb and LREE (Fig. 11). Pyroxenite amphiboles typically show slight LREE depletion (La_N/Sm_N = 0.5-0.8, for Sm_N = 25.1-40.7), no evident Eu anomaly and nearly flat MREE-HREE (Gd_N/Yb_N = 0.9-1.4, for Yb_N = 21-28). These amphiboles have incompatible element patterns characterized by positive Ba anomaly with respect to Rb and Th, and slight to moderate depletion of Th, U, Nb and Ta with respect to LREE. Amphibole from

plagioclase-free pyroxenite MC22A mainly differs in weak LREE enrichment with respect to MREE-HREE (La_N/Sm_N = 1.3, for SmN = 40.7) and marked Th-U enrichment with respect to Nb-Ta. The concentrations of Cr, Ni and Sc in amphiboles from the pyroxenites are 2000-6000 ppm, 130-200 ppm and 67-140 ppm.

Amphiboles from the hornblendite vein and the hornblende-rich gabbro and hornblende gabbronorite dykes have relatively homogeneous REE compositions (Fig. 11). Their chondrite-normalized REE patterns exhibit slight LREE depletion (La_N/Sm_N = 0.4-0.7, for Sm_N = 19.3-37.7), no evident Eu anomaly and barely appreciable enrichment of MREE over HREE (Gd_N/Yb_N = 1.2-1.5, for Yb_N = 17-32). Normalization of incompatible elements to primordial mantle shows Ba enrichment with respect to Rb, Th, U, Nb and Ta; in addition, Nb and Ta are slightly or not depleted with respect to LREE. Amphibole from the plagioclase-free hornblendite vein is distinct in the high Pb and Sr concentrations, which depict positive anomalies with respect to LREE. Amphiboles from the hornblendite veins and the hornblende-rich gabbro and hornblende gabbronorite dykes typically display lower Cr, Ni and Sc (≤770 ppm, 41-150 ppm and 56-77 ppm, respectively) than amphiboles from the peridotite-pyroxenite sequence. The lowest Cr amounts were found for amphiboles from the hornblende-rich gabbro dykes (≤130 ppm).

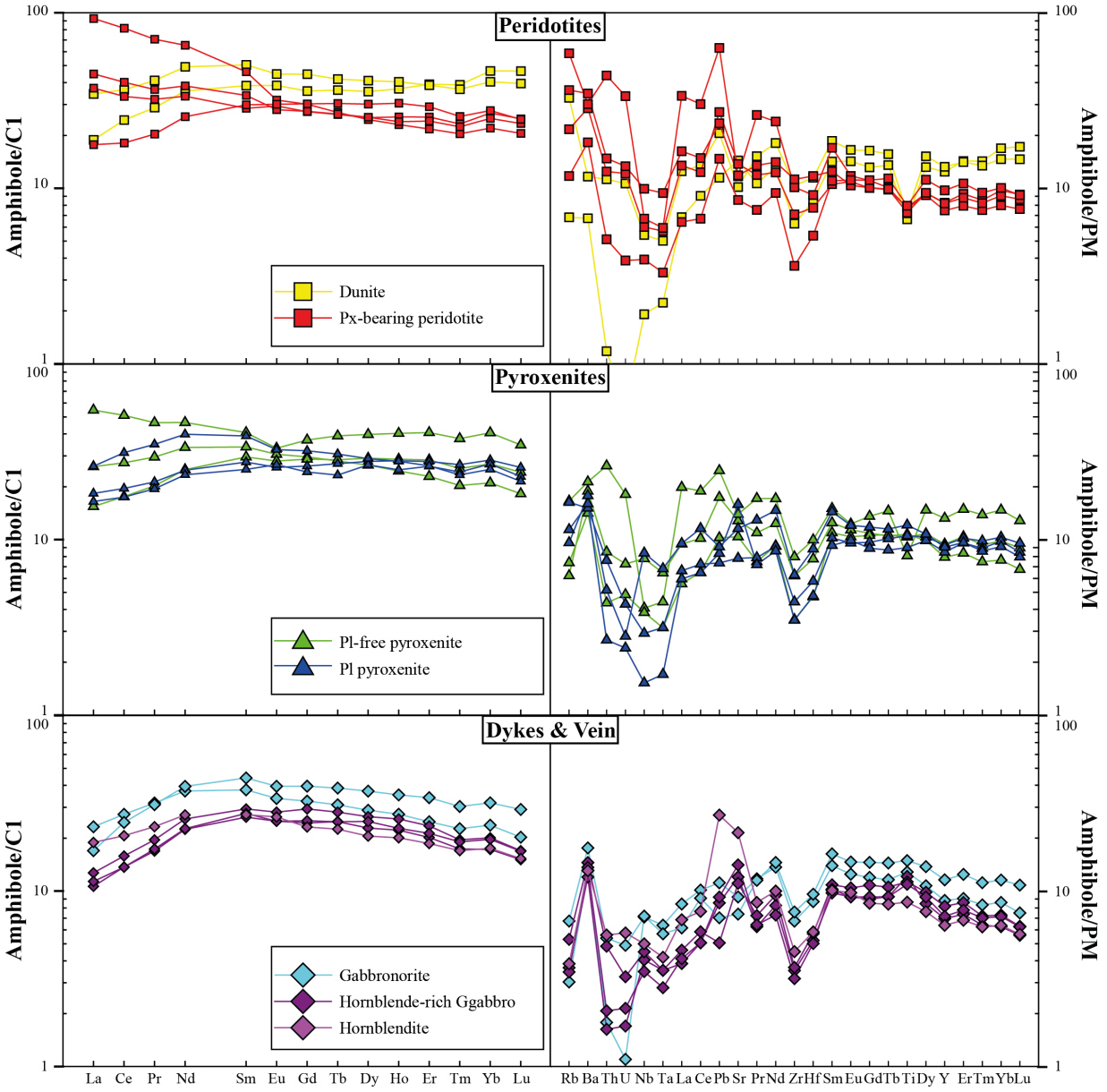

Figure 11: REE and incompatible trace element compositions of amphiboles normalised to C1 chondrite (LYUBETSKAYA AND KORENAGA, 2007) and to Primordial Mantle (SUN AND MCDONOUGH, 1989), respectively.

7.2 Clinopyroxene

Clinopyroxene was analyzed in pyroxenites MC8B, MC20/1 and BC2A, and hornblende gabbronorite dyke MC7/4. The analysis of clinopyroxene from peridotites was precluded by its typical intimate association with amphibole lamellae and patches (e.g., Fig. 3c). Chondrite-normalized REE patterns of pyroxenite clinopyroxenes are characterized by slight LREE depletion with respect to MREE (La_N/Sm_N = 0.5-0.6, for Sm_N = 15-17), no evident Eu anomaly, and nearly flat MREE-HREE (Gd_N/Yb_N = 1.1-1.4, for Yb_N = 10-14). In addition, pyroxenite clinopyroxenes show variable Cr amounts and relatively low Ni concentrations (1100-3600 ppm and 82-90 ppm, respectively). Clinopyroxene from the hornblende gabbronorite is LREE depleted (La_N/Sm_N = 0.3, for Sm_N = 20) and displays the lowest abundances of Cr and Ni (220 ppm and 34 ppm, respectively). Normalization of incompatible elements to primordial mantle concentrations shows that all clinopyroxenes are characterized by Nb and Ta depletion with respect to LREE, and slight Pb-Sr depletion with respect to adjacent REE.

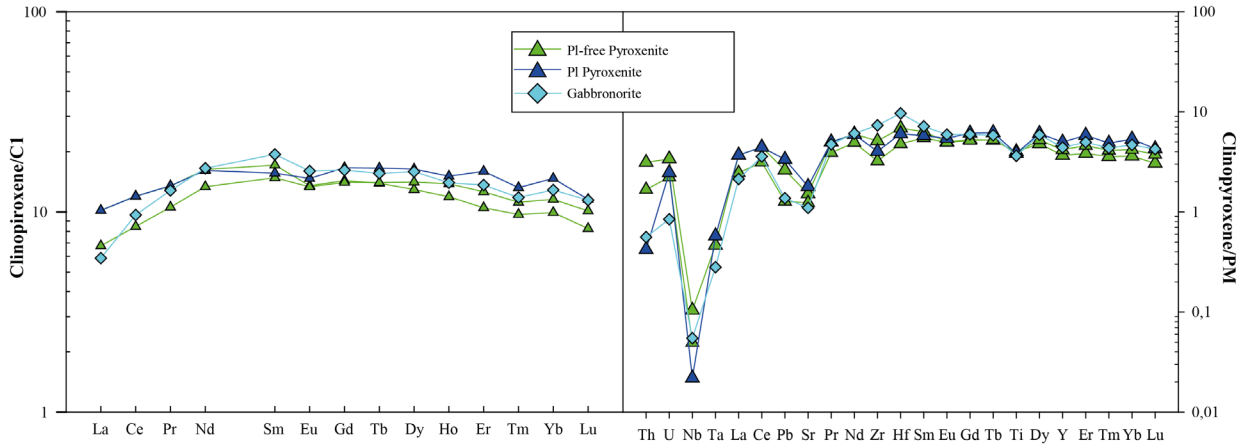

Figure 12: REE and incompatible trace element compositions of clinopyroxenes normalized to CI chondrite (LYUBETSKAYA AND KORENAGA, 2007) and to Primordial Mantle (SUN AND MCDONOUGH, 1989), respectively.

8. Nd-Sr isotopic compositions

The Nd and Sr isotopic compositions and Sm, Nd, Rb, Sr concentrations were measured on eleven whole-rock samples and six amphibole separates. The amphiboles were checked under a binocular microscope and handpicked. The data were obtained at Laboratoire de Geosciences Marines (Université de Brest, France) using a Thermo Scientific Triton mass spectrometer in static mode. Samples were initially dissolved by acid digestion and then processed through columns with HCl and HNO_3 acids for chemical separation. The $^{143}Nd/^{144}Nd$ and $^{87}Sr/^{86}Sr$ were normalized to an $^{86}Sr/^{88}Sr$ ratio of 0.1194 and $^{146}Nd/^{144}Nd$ ratio of 0.7219, respectively, and reported relatively to "La Jolla" Nd standard $^{143}Nd/^{144}Nd = 0.511860$, NBS987 Sr standard $^{87}Sr/^{86}Sr = 0.710248$ and NIST987 $^{87}Sr/^{86}Sr = 0.71034$. The analyses were carried out during multiple analytical sessions. The $^{143}Nd/^{144}Nd$ "La Jolla" standard and the $^{87}Sr/^{86}Sr$ "NBS987-NIST987" standards returned overall mean values during the period of work of 0.710258 ± 0.000011 (2σ) and 0.511849 ± 0.000007 (2σ) respectively. The concentrations of Sm, Nd, Rb and Sr were determined by isotope dilution. The isotope dilution results in amphibole separates are overall consistent with the Sm, Nd, Rb and Sr concentrations obtained in situ by laser ablation ICP mass spectrometry at the core of the amphibole grains.

Because of uncertainties in the crystallization age, calculation of initial Nd-Sr isotopic compositions was carried out at 315, 290 and 200 Ma (Table 6). Results show that these age variations scarcely affect the values of initial Nd-Sr isotopic compositions. In addition, the initial Nd-Sr isotopic compositions of amphiboles and host whole-rocks are similar, independently of age variations. A significant discrepancy was observed for the Sr isotopic compositions of plagioclase-free pyroxenite MC8B, for which the whole-rock and amphibole $^{87}Sr/^{86}Sr$ ratios calculated at 290 Ma are 0.7061 and 0.7069, respectively. This difference could reflect partial replacement of primary amphibole by $^{87}Sr/^{86}Sr$-enriched secondary amphibole.

Figure 13a reports the whole-rock and amphibole Nd-Sr isotopic compositions calculated at 290 Ma. There is no correlation between Nd-Sr isotopic signature and rock type. The peridotites (dunites and pyroxene-bearing peridotites) and the pyroxenites have whole-rock/amphibole ε_{Nd}(290 Ma) values varying from -0.8 to -4.0 and from -2.2 to -4.7, respectively. The hornblende-rich gabbro and hornblende gabbronorite dykes have ε_{Nd}(290 Ma) ranging from +0.1 to -2.8. The whole-rock/amphibole $^{87}Sr/^{86}Sr$ ratios calculated at 290 Ma varies from 0.7066 to 0.7075 for the dunites and the pyroxene-bearing peridotites, from 0.7061 to 0.7071 for the pyroxenites, and from 0.7061 to 0.7070 for the dykes.

Figure 13b shows a comparison between the Nd-Sr isotopic compositions of the Monte Capio-

Alpe Cevia sequences with those of other ultramafic magmatic sequences from the Ivrea-Verbano Zone, namely the ultramafic layers from the Ivrea Mafic Complex and the Ultramafic Pipes from the intermediate-upper sector of the Ivrea-Verbano Zone (Voshage et al., 1990; Garuti et al., 2001; Fiorentini et al., 2018). The Monte Capio-Alpe Cevia rocks fall within the wide Nd-Sr isotopic trend defined by the ultramafic layers from the Ivrea Mafic Complex and the Ultramafic Pipes. This trend may reflect the variability of primary melt compositions (Garuti et al., 2001), and/or record a process of crustal contamination by primary melts with isotopically depleted Nd-Sr isotopic compositions (Voshage et al., 1990). We noted that the Ultramafic Pipes are typically characterized by lower Sm/Nd than the Monte Capio-Alpe Cevia rocks, in agreement with the Ultramafic Pipes amphiboles showing a marked LREE enrichment (Locmelis et al., 2016).

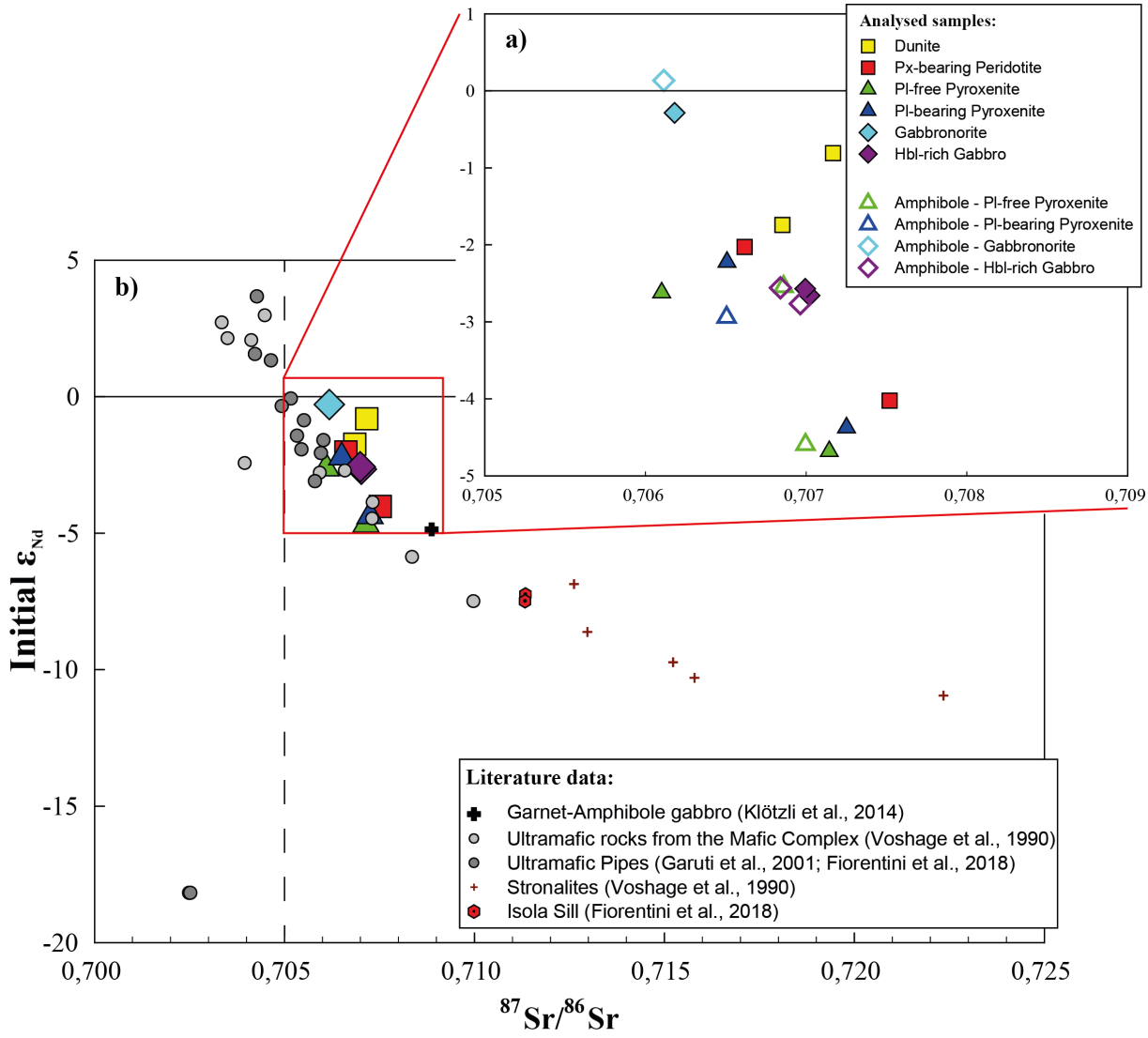

Figure 13: Plot of initial ε_{Nd} versus initial $^{87}Sr/^{86}Sr$. Figure a) illustrates the compositions of whole rocks and amphiboles of the Monte Capio-Alpe Cevia ultramafic associations calculated at 290 Ma (present study). In figure b), the whole-rock Monte Capio-Alpe Cevia compositions are compared with the compositions of relevant rock sequences from the Ivrea-Verbano Zone. Literature data are after: (i) VOSHAGE ET AL. (1990) for the ultramafic rocks from the Mafic Complex and granulite facies metasediments (stronalites), (ii) FIORENTINI ET AL. (2018) for the Isola ultramafic sill within the Mafic Complex, and (iii) GARUTI ET AL. (2001) and FIORENTINI ET AL. (2018) for the Ultramafic Pipes. ε_{Nd} and $^{87}Sr/^{86}Sr$ were calculated at 290 Ma, with the exception of: (i) samples from Valmaggia Ultramafic Pipe calculated at 250 Ma (LOCMELIS ET AL., 2016), and the amphibole-garnet gabbro from the study area calculated at 315 Ma (KLÖTZLI ET AL., 2014).

9. Discussion

The Monte Capio-Alpe Cevia ultramafic bodies (Fig. 1) essentially consist of a peridotite core, with dunite in the center, mantled by minor, orthopyroxene-dominated pyroxenites and subordinate hornblende gabbronorites. Amphibole is ubiquitous in these peridotite-pyroxenite sequences, which is frequently crosscut by amphibole-rich veins/dykes. The ultramafic bodies considered in the present study therefore share several structural and compositional similarities to the Alaskan-type intrusion complexes, which represent deep sectors of oceanic or continental magmatic arcs (e.g., Irvine, 1974; Himmelberg and Loney, 1995). These similarities include: (i) the internal lithological zoning, with an ultramafic core evolving into a compositionally evolved margin, and (ii) the widespread occurrence of amphibole. For instance, the Monte Capio-Alpe Cevia sequences resembles the deep-seated, Neoproterozoic Genina Gharbia complex from South Eastern Desert (Egypt), which is characterized by orthopyroxene modally prevailing over clinopyroxene (e.g., Helmy et al., 2014), and (ii) the Archean Fiskenæsset ultramafic sill from South Western Greenland, which includes hornblendite vein networks (Polat et al., 2012). However, regional geological constraints do argue against formation of the Monte Capio-Alpe Cevia sequences in a supra-subduction zone setting. The sequences were related with the late- to post-collisional, extensional phases of the Variscan orogeny (e.g., Klötzli et al., 2014), or with the rifting evolution leading to opening of the Jurassic Alpine Tethys (Denyszyn et al., 2018). The compositions of the primitive melts involved in the building of the Monte Capio-Alpe Cevia ultramafic bodies, and magmatic evolution experienced by these melts are the main objects of the following discussion sections.

9.1 Do clinopyroxene and amphibole compositions reflect melt compositions?

The Monte Capio-Alpe Cevia ultramafic sequences, as well as the crosscutting hornblendite veins and hornblende-rich gabbro and hornblende gabbronorite dykes, typically display granoblastic structure. The original magmatic mineral assemblages may have therefore experienced re-equilibration by solid state diffusion and/or recrystallization in response to slow cooling in the lower continental crust. Major element mineral compositions sustain this inference. For instance, the Ca-in-Opx geothermometer (Brey and Kohler, 1990), which may be applied to the samples including olivine, spinel and two pyroxenes, gives temperature estimates of 803 to 866 °C (Table 7) corresponding to granulite facies metamorphic conditions. Consistently, the high Mg# of clinopyroxene with respect to associated olivine cannot be reconciled with magmatic conditions (Fig. 14) and may attributed to Mg-Fe^{2+} exchange between clinopyroxene and olivine during

subsolidus slow cooling in the lower continental crust (Loucks, 1996).

Application of the amphibole-plagioclase geothermometer of Holland and Blundy (1994) to the plagioclase-bearing pyroxenites, the hornblende-rich gabbros and the hornblende gabbronorites gave relatively high values ranging from 905 to 980 °C (Table 7). The amphibole geothermometer of Putirka (2016) was also applied to all samples, and we obtained slightly higher values of 967 to 1021 °C. We infer that the amphibole-based geothermometers of Holland and Blundy (1994) and Putirka (2016) have a higher closure temperature the Ca-in-Opx geothermometer of Brey and Kohler (1990). The relatively high temperature evaluations based on amphibole compositions could be associated with near magmatic conditions.

In the Monte Capio-Alpe Cevia pyroxenites, olivine and plagioclase are not observed to coexist, thereby implying a potential metamorphic origin for clinopyroxene in these rocks. A *subsolidus* nature was actually proposed for the spinel-rich pyroxenites at the base of the fossil island arc crust from Talkeetna (Alaska), in response to the following reaction (Hacker et al., 2008):

(1) olivine + plagioclase = orthopyroxene + clinopyroxene + spinel

In the Talkeetna pyroxenites, the petrographic evidence for the occurrence of reaction (1) is given by symplectitic intergrowths made up of spinel and two pyroxenes. The olivine-bearing and the plagioclase-bearing pyroxenites from the Monte Capio-Alpe Cevia ultramafic sequences could record exhaustion of reacting plagioclase and olivine of magmatic origin, respectively, in response to reaction (1). Following this hypothesis, clinopyroxene from these pyroxenites is of metamorphic origin, with the annealing process erasing the symplectitic spinel + two pyroxene intergrowths. However, clinopyroxenes produced by reaction (1) typically show nearly flat, chondrite-normalized REE and positive Eu anomaly (Gregoire et al., 1994; Montanini and Tribuzio, 2001). In these granulite facies clinopyroxenes, in addition, the concentrations of trivalent REE, Y, Zr, Cr, V and Sc are characteristically low, because reactant minerals plagioclase and olivine have low or negligible concentrations of these elements. Furthermore, clinopyroxenes produced by reaction (1) have relatively high Sr and Ni concentrations, because these elements are compatible in plagioclase and olivine, respectively. The clinopyroxenes from Monte Capio-Alpe Cevia pyroxenites do not have this trace element signature. For instance, they have relatively high REE concentrations with chondrite-normalized patterns lacking positive Eu anomaly (Fig. 12), and relatively low Ni contents of 82-90 ppm. We therefore argue against the idea that clinopyroxene from the pyroxenites of the present study is of metamorphic origin.

The original trace element compositions of magmatic clinopyroxene and amphibole could indeed have changed during the high temperature *subsolidus* evolution. In mantle and magmatic ultramafic rocks, olivine and orthopyroxene incorporate substantially lower amounts of incompatible trace

elements than associated clinopyroxene and amphibole. The partitioning of incompatible elements in olivine and orthopyroxene with respect to clinopyroxene typically increases with decreasing temperature conditions (Witt-Eickschen and O'Neill, 2005; Yao et al., 2012). In mantle spinel peridotites, however, *subsolidus* re-equilibration was shown to not significantly alter the REE compositions of clinopyroxene (Hellebrand et al., 2005). Conversely, in plagioclase-bearing mantle peridotites and pyroxenites, a process of slow cooling is associated with development or increasing of negative Eu anomaly in clinopyroxene and amphibole (e.g., Rampone et al., 1993; Bodinier et al., 2008). Plagioclase could also play a major role in incorporating Sr and Pb, because these elements are less compatible in clinopyroxene/amphibole than in plagioclase (e.g., Bindeman et al., 1998; Tiepolo et al., 2007).

In rocks including plagioclase selected for the present study, clinopyroxene and amphibole characteristically show negligible negative Eu anomaly (Figs. 11 and 12). We therefore speculate that *subsolidus* re-equilibration with plagioclase did not substantially change the REE signature of clinopyroxene and amphibole. In rocks where we analyzed the clinopyroxene-amphibole pairs, these two minerals display subparallel REE patterns, with slightly higher total REE concentrations in amphiboles, by a factor mostly ranging between 1.5 and 3.0 (Fig. 15). The REE partitioning between clinopyroxene and amphibole is rather constant, thereby indicating approach of chemical equilibrium conditions between these two phases. For elements having low diffusion coefficients, such as REE and Y (Van Orman et al., 2001), we propose that the high temperature *subsolidus* re-equilibration between clinopyroxene and amphibole may have slightly changed but not obliterated the original magmatic fingerprint of these phases, particularly if the trace element ratios rather than absolute concentrations are considered. Note also that some of the incompatible trace elements analyzed for amphibole (i.e., Th, U, Nb and Ta) are not significantly incorporated in all other coexisting minerals, thereby implying that the concentrations of these elements in amphibole are not substantially affected by high temperature *subsolidus* re-equilibration. Hence, the petrogenetic discussion in the following sections will mostly benefit of amphibole trace element compositions, mostly on the basis of relative ratios among REE, Th, U, Nb and Ta.

9.2 Evidence for migration of H_2O-rich melts into the peridotite-pyroxenite sequences

Amphibole is ubiquitous in the Monte Capio-Alpe Cevia peridotite-pyroxenite sequences (≤15 vol% in the peridotites and 10-40 vol% in the pyroxenites), thereby suggesting involvement of H_2O-rich melts in its formation. This is consistent with the high proportion of anorthite component in plagioclase from the plagioclase-bearing pyroxenites (91-88 mol%), because formation of anorthite-rich plagioclase is favored by increasing H_2O melt contents (e.g., Sisson and Grove,

1993; Panjasawatwong et al., 1995; Hamada and Fujii, 2007). Involvement of H_2O-rich melts is also suggested by the fact that the peridotite-pyroxenite sequences are frequently crosscut by amphibole-rich (45-90 vol%) veins/dykes. Involvement of H_2O-rich melts in the formation of the Monte Capio-Alpe Cevia sequences may be related to former, subduction-related mantle metasomatism, which presumably occurred in conjunction with the Variscan subduction. Mantle sources metasomatized by the Variscan subduction have been recently similarly invoked to explain the origin of the parental melts giving rise to other ultramafic sequences of the Ivrea-Verbano Zone, the so-called Ultramafic Pipes (Locmelis et al., 2016; Fiorentini et al., 2018). In the following sections, we will specifically deal with the origin of the different types of amphibole-rich veins/dykes.

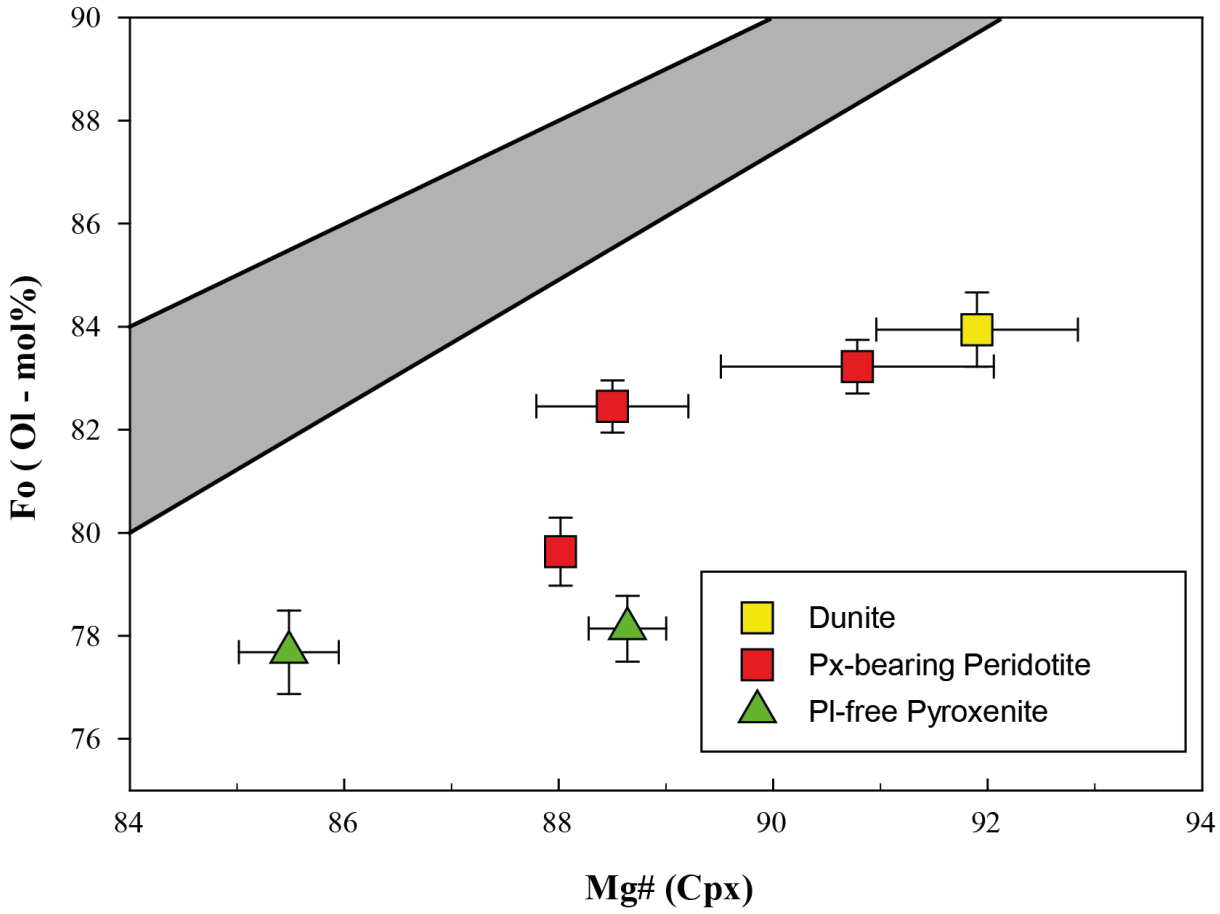

Figure 14: Plot of the forsterite content of olivine versus the Mg# [molar $Mg/(Mg+Fe^{2+}_{tot}) \times 100$] of associated clinopyroxene for the Monte Capio-Alpe Cevia peridotite-pyroxenite sequences. Data are averaged per sample; error bars denote the compositional within-sample variations and represent the standard deviation of the mean value. The grey field corresponds to the field of olivine-clinopyroxene pairs of magmatic origin, which is constrained by 1:1 and 23:30 Fe-Mg olivine-clinopyroxene partitioning (Roeder and Emslie, 1970; Obata et al., 1974).

9.2.1 Formation of hornblendite veins

The hornblendite veins show sinuous to sharp planar boundaries (Fig. 2), are up to centimeter-scale thick and composed of amphibole (Figs. 3f and 5a), minor orthopyroxene and accessory green spinel. The contacts with host peridotites are characterized mm-scale thick, spinel-bearing and amphibole-free orthopyroxenite reaction zones, which most likely formed by a melt-driven substitution reaction leading to olivine replacement by orthopyroxene. The Mg# of the hornblendite vein MC27/1 B is only slightly lower than that of host dunite MC27B (80.8 and 82.7, respectively; Fig. 4), and shows that the whole-rock chemical chemistry of the hornblendite does not represent a frozen melt. We relate the high Mg# of the hornblendite to a process of interaction between the migrating, amphibole-saturated melt and host dunite. Note that the lack of olivine and the development of orthopyroxene in the hornblendites document that the migrating melt was relatively SiO2-rich, in agreement with formation of the orthopyroxenite reaction zone.

The origin of the hornblendite veins is therefore attributed to the following reaction (mineral abbreviations after Whitney and Evans, 2010):

(2) Ol + Cr-Spl + SiO_2- and H_2O-rich melt = Amp + Opx + Al-Spl ± residual melt,

where olivine and Cr-spinel represent the host dunite, melt 1 represents the migrating melt, and amphibole, orthopyroxene and Al-spinel represent the hornblendite. We calculated the SiO_2 of the hornblendite-forming melt based on amphibole compositions, following the method of Putirka (2016) and assuming that amphibole from the hornblendite did not substantially change its major element compositions during the *subsolidus* cooling evolution. We obtained a SiO_2 value of 51 wt%, which is markedly higher than the SiO_2 content of host dunite (39 wt%, Table 2). Note that the hornblendite vein has slightly higher SiO_2 (43 wt%) than host dunite, thereby implying that the potential melt fraction able to migrate out of the local system (i.e., residual melt) was somewhat SiO_2-depleted with respect to the migrating reacting melt. Assuming closed system conditions (i.e., no residual melt), reaction (2) is balanced for SiO_2 with a melt/dunite ratio of 3:7.

9.2.2 Formation of hornblende-rich gabbro dykes

The hornblende-rich (80-90 vol%) gabbro dykes are typically up to ~0.5 m thick and locally crosscut the hornblendite veins. These dykes display sharp contacts against host peridotites and pyroxenites, and an internal magmatic layering, thereby showing injections of H_2O-rich melts through fracture-controlled mechanisms. Whereas the hornblendite veins most likely represent early melt injections, possibly before complete solidification of the peridotite-pyroxenite sequences, the hornblende-rich gabbro dykes formed subsequently, in a melt-dominated system. Notably, these dykes preserve microstructures documenting late crystallization of plagioclase with respect

to amphibole (Fig. 5b), and have high whole-rock TiO_2 contents (Fig. 4) showing formation ruled by amphibole "accumulation".

We calculated the SiO_2 content of the melts forming the hornblende-rich gabbro dykes based on amphibole compositions, following the method of PUTIRKA (2016), and we obtained values of 49-50 wt%, which are closely similar to those calculated for the horneblendite vein (51 wt%). We also computed the Mg# of the melt in equilibrium with amphibole assuming that: (i) the *subsolidus* cooling evolution did not significantly change the original Mg# of magmatic amphibole, in agreement with the fact that amphibole in these rocks is not associated with other mafic silicates, and (ii) an amphibole/melt Fe-Mg partition coefficient of 0.36 (NANDEDKAR ET AL., 2014). Accordingly, the melts feeding the hornblende-rich gabbro dykes had relatively low Mg# of 50-52. The evolved nature of these melts is confirmed by the low Cr contents of amphibole from the hornblende-rich gabbro dykes (5-110 ppm, Table 4).

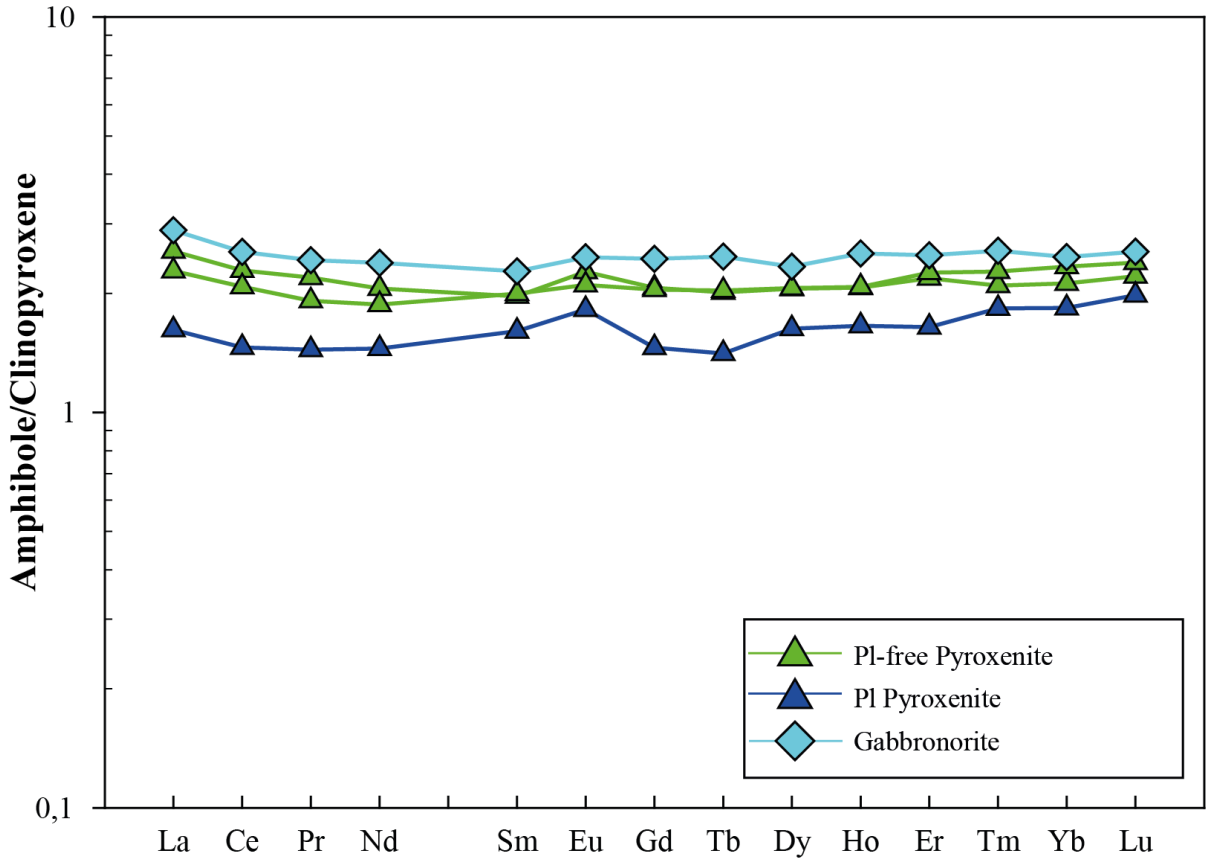

Figure 15: Amphibole/clinopyroxene partition ratios for REE.

9.2.3 Formation of hornblende gabbronorite dykes

Hornblende gabbronorites (amphibole = 45-55 vol%) occur as dykes within the ultramafic sequences and, locally, along the contact with metasedimentary basement rocks. These rocks include significant amounts of orthopyroxene and clinopyroxene (Table 1), and have lower Mg# than the hornblende-rich gabbros (66-68 and 72-73, respectively). Amphiboles consistently have relatively low Mg# (Table 3, Fig. 9) and are associated with plagioclases showing relatively low proportion of anorthite component (65-76 mol% vs. 84-91 mol% in hornblende-rich gabbro dykes). These evolved chemical characteristics are consistent with the relatively low Mg# (Fig. 8), Cr and Ni values (217 ppm and 34 ppm, respectively) of the clinopyroxene analyzed for the hornblende gabbronorite dykes. Assuming that amphibole did not change significantly its major element compositions in response to *subsolidus* re-equilibration, the melts feeding these dykes had SiO2 of 51-53 wt%, based on Putirka's (2016) procedure.

Amphibole from hornblende gabbronorites have lower Mg# (Fig. 9) and higher Cr (Tables 3 and 4) than amphibole from hornblende-rich gabbros. These chemical characteristics are difficult to reconcile with a closed system fractional crystallization process relating the two rock types. This inference is substantiated by whole-rock Nd-Sr isotopic compositions (Table 6, Fig. 13), because analyzed hornblende gabbronorite has higher ε_{Nd}(290 Ma) and lower $^{87}Sr/^{86}Sr$(290 Ma) (-0.3 and 0.7062) than the two selected hornblende-rich gabbros (about -2.6 and 0.7070). Note finally that the different mineralogical compositions of the two rock-types imply involvement of melts having different H_2O contents. In particular, the hornblende gabbronorites include a substantial pyroxene modal proportion (20-25 vol%) and have lower modal amphibole than hornblende-rich gabbros. We conclude the melts feeding the hornblende gabbronorites had lower H_2O than the melts giving rise to the hornblende-rich gabbros.

9.2.4 Origin of melts feeding veins and dykes: inferences from incompatible trace element compositions

The amphibole-rich veins and dykes crosscutting the Monte Capio-Alpe Cevia ultramafic sequences include amphiboles with similar REE signature (Fig. 10). For instance, the La_N/Sm_N and Gd_N/Yb_N values of amphibole are 0.4-0.7 and 1.2-1.5, respectively. The REE compositions of melts in equilibrium with amphibole were calculated using amphibole/melt partition coefficients, which were computed (Table 8) based on amphibole major element compositions and crystallization temperature conditions, following the method of Shimizu et al. (2017) in turn relying on the amphibole-melt trace element partitioning experimentally produced at 0.7 GPa by Nandedkar et al. (2016). For the crystallization temperatures, we assumed those calculated following Putirka (2016), which could be reconciled with magmatic conditions. The melt REE compositions calculated for the hornblendite vein and the hornblende-rich gabbro and hornblende gabbronorite dykes (Fig. 16) are relatively homogeneous (La_N/Sm_N = 2.3-4.0 and Gd_N/Yb_N = 0.9-1.0) and approach those of modern E-MORB (Gale et al., 2013).

The concentrations of Th, U, Pb and Sr in amphiboles from veins and dykes conversely show wide variations (Fig. 10). For instance, the fractionation of Th to Ba and of U to Nb is extremely variable, irrespective of the host rock type. In addition, amphibole from hornblende-rich gabbros is Sr-enriched with respect to adjacent REE, whereas the opposite relationship is observed for amphibole from hornblende gabbronorites. Furthermore, amphibole from the hornblendite vein is distinct in the marked Sr-Pb enrichment with respect to adjacent REE. These Th, U, Pb and Sr variations cannot be overall explained by fractional crystallization and/or *subsolidus* re-equilibration processes. Amphiboles from veins and dykes notably have Th/Nb, U/Ta, Th/Y and LaN/SmN values depicting positive correlations (Fig. 17), with the sample showing the lowest incompatible trace element ratios (gabbronorite MC27A, Table 5) distinct in the highest ε_{Nd}(290 Ma) and the lowest $^{87}Sr/^{86}Sr$(290 Ma) (Table 7). These compositional variations may therefore reflect involvement of different extents of crustal component in the melts feeding the veins and the dykes.

The basement hosting the ultramafic sequences is mostly made up of nearly anhydrous, garnet-rich metasediments (e.g., Redler et al., 2012; Ewing et al., 2013). These rocks are characterized by high concentrations of Th, U, Pb and Sr (Schnetger et al., 1994; see also Fig. 16), and have low Nd and high Sr isotopic ratios (Voshage et al., 1990; see also Fig. 12). Taken as a whole, the different Th/Nb, U/Ta, Th/Y and La_N/Sm_N values of amphibole from the veins and the dykes could therefore be due to assimilation of lower crustal material by the mantle melts. Note that the melts feeding the hornblende-rich gabbro and the hornblende gabbronorite dykes most likely also

had different amounts of H_2O, as documented by the different mineralogical compositions of the two dyke types. We argue that these H_2O melt variations cannot be related to assimilation of lower crustal material, because the basement rocks are typically nearly anhydrous.

In summary, the melts feeding the amphibole-rich veins and dykes show a similar geochemical signature. These melts however concentrated different amounts of Th, U, Pb, Sr and H2O. These variations may be due to a process of assimilation of crustal material but they are at least partly related to involvement of primary melts having different compositions. The latter interpretation is consistent with the idea by LOCMELIS ET AL. (2016) that the mantle sources involved in the origin of the Ivrea-Verbano magmatic sequences were variably contaminated by melts/fluids released by a subducting crust during the Variscan subduction.

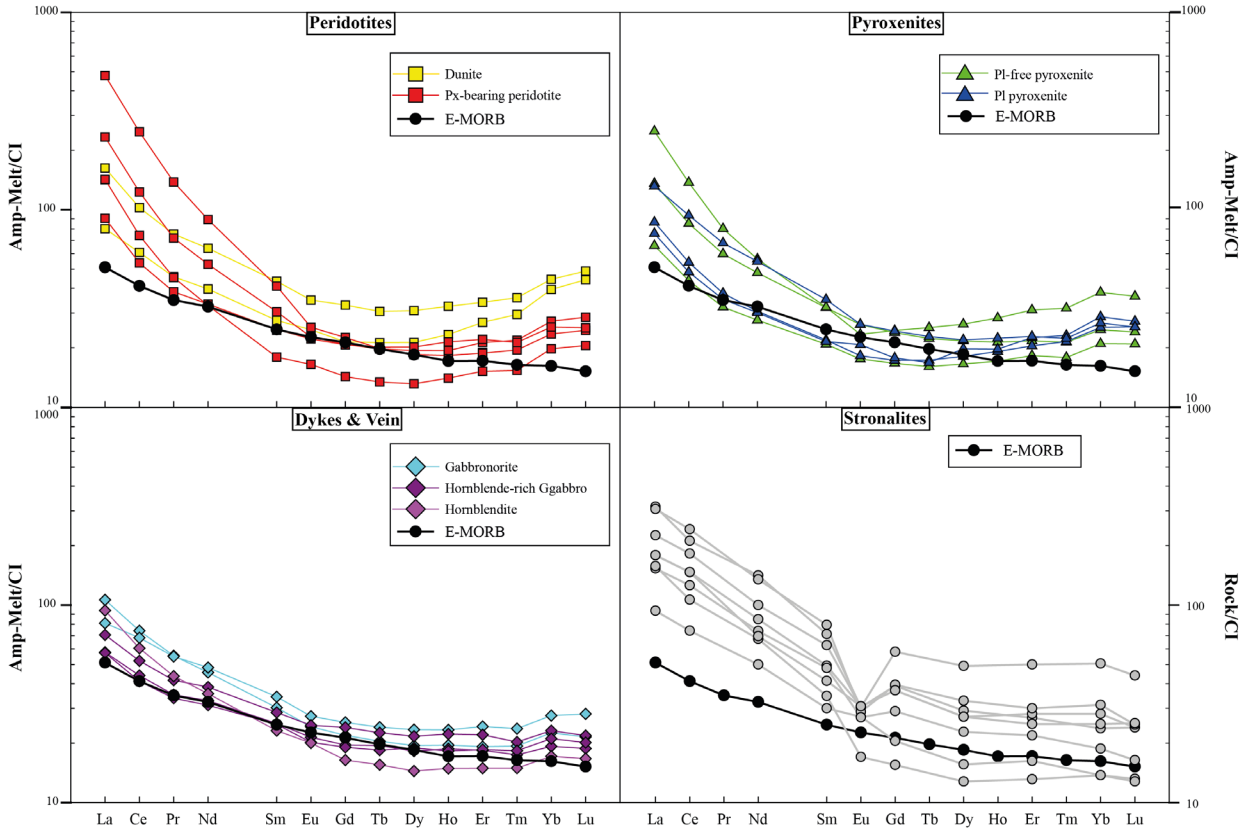

Figure 16: REE compositions of melts in equilibrium with amphiboles. Calculations were carried out using amphibole/melt partition coefficients, which were computed (Table 8) based on amphibole major element compositions and crystallization temperature conditions, following the method of SHIMIZU ET AL. (2017). Melt compositions were normalized to CI chondrite (LYUBETSKAYA AND KORENAGA, 2007). The mean composition of E-MORB (GALE ET AL., 2012) and the composition of granulite facies metasediments of the Ivrea Verbano Zone (stronalites, SCHNETGER ET AL., 1994) are reported for comparative purposes.

9.3 The dunites from the Monte Capio-Alpe Cevia ultramafic sequences are chemically evolved

Olivine from the Monte Capio-Alpe Cevia dunites is relatively poor in forsterite component and NiO (83-84 mol% and 0.06-0.09 wt%), and is associated with spinel having relatively low Cr# (19-24, see also Figs. 10 and 18). To our knowledge, dunites with such an evolved chemical signature are extremely rare (see Su et al., 2015). We computed the Mg# of the melt in equilibrium with the most primitive olivine, assuming an olivine-melt partition coefficient of 0.31 (Toplis, 2005), and we obtained a melt Mg# value of 0.62.

The melt that equilibrated with the dunites could have previously experienced substantial olivine + spinel fractionation, which is expected to diminish the Mg# of the derivative melts and the resulting dunites. This hypothetical process implies that olivine + spinel were the only liquidus phases in a wide temperature range and, ultimately, the presence of chemically primitive dunites at lower crustal levels and/or within the subcontinental mantle. Note that the stability of olivine as the only silicate liquidus phase was experimentally shown to be favored by high H2O melt contents and low fO2 conditions (Müntener and Ulmer, 2006). For instance, in the equilibrium crystallization experiment starting from a hydrous picrobasaltic melt (SiO_2 = 47.6 wt% and H2O = 2.6 wt%) carried out at P =1.5 GPa and fO_2 conditions close to C-CO-CO_2 equilibrium, Müntener and Ulmer (2006) found olivine-only fractionation in the 1350-1230 °C interval. The low Mg# of melts in equilibrium with the dunites could also at least partly reflect a mantle signature, with the primary melts formed by partial melting of material including a substantial proportion of Al-rich and Cr-and Ni-poor mafic rocks, such as pyroxenite heterogeneities genetically related to recycling of crustal mafic rocks (e.g., Allegre and Turcotte, 1986; Kornprobst et al., 1990; Montanini and Tribuzio, 2015).

A wide interval of olivine-only fractionation was proposed (Jagoutz et al., 2006; 2007) to explain the origin of the dunites from the ultramafic sequences of the Chilas Complex (Kohistan), which are frequently characterized by forsterite- and Ni-poor olivines (Fo = 90-81 mol%, NiO ≤0.20 wt%). The Chilas dunite bodies were considered to be mantle diapirs that allowed primary melts to rise up into the lower crust (see also Burg et al., 1998 and Jagoutz et al., 2011). Hence, these bodies were considered to be of mantle replacive origin (e.g., Kelemen et al., 1990), consistently with the occurrence of relict olivine websterite xenoliths within them. In particular, Jagoutz et al. (2006; 2007; 2011) proposed that the Chilas dunite bodies formed by "percolative fractional crystallization", namely continuous melt migration coupled with fractionation of olivine within the dunites.

We did not find any clear evidence for the Monte Capio-Alpe Cevia dunites being of replacive

mantle nature. Hence, these dunites may have a crustal magmatic origin, by cooling of melt lenses intruding the lower continental crust, thereby implying that the chemically evolved signature of the dunite-forming melts was related to earlier olivine + spinel fractionation. We cannot exclude, however, that the dunites acted for conduits for ascending mantle melts, as this lithology represents high porosity material through which melt may flow through grain boundaries under high temperature conditions (e.g., Kelemen et al., 1995). Following this hypothesis, the chemically evolved signature of the dunite equilibrium melts was related to melt migration coupled with fractionation of olivine within the conduits.

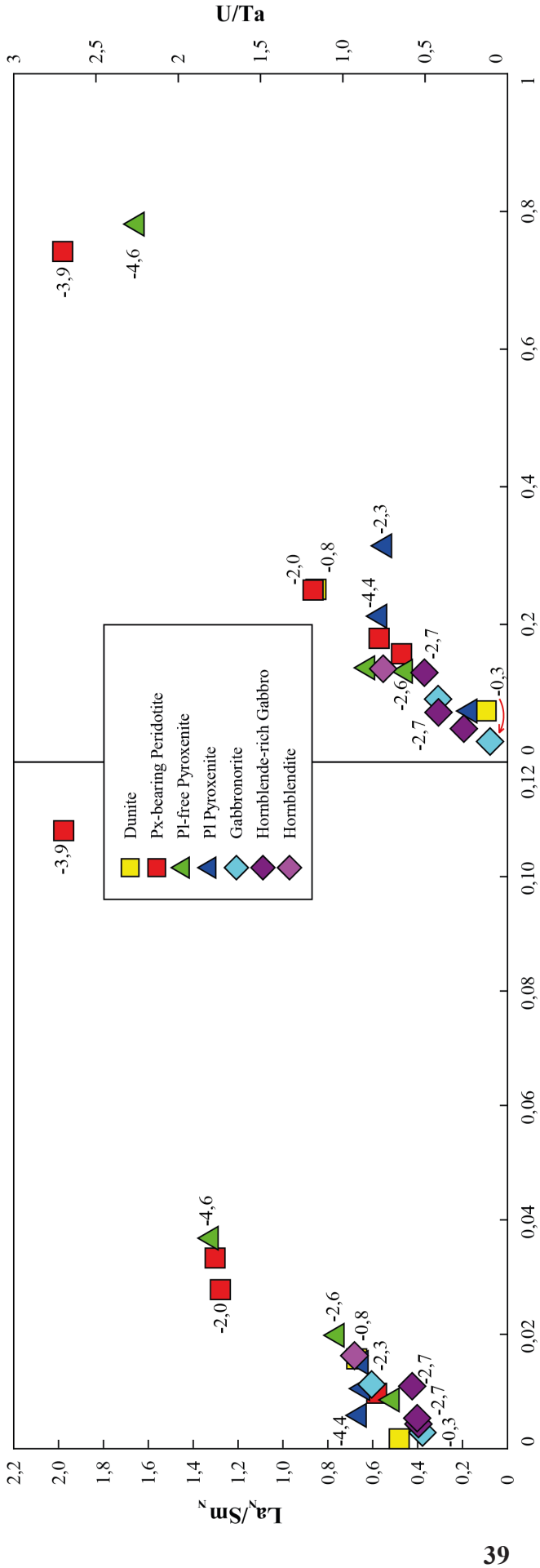

Figure 17: Amphibole trace element compositions: U/Ta versus Th/Nb, and La_N/Sm_N (normalized to CI chondrite of Lyubetskaya and Korenaga (2007) vs. Th/Y. Data are averaged per sample; whole-rock ε_{Nd}(290 Ma) values are also reported.

9.4 Building of the peridotite-pyroxenite sequences: closed vs. open system magmatic conditions

The pyroxene-bearing peridotites from the Monte Capio-Alpe Cevia sequences have up to 15 vol% and 10 vol% clinopyroxene and orthopyroxene, respectively, and 5-15 vol% amphibole (Table 1). The whole-rock Mg# and the forsterite content of olivine (Figs. 4 and 6) overall decrease from the dunites to the pyroxene-bearing peridotites. For instance, the olivine forsterite proportion ranges from 83-84 mol% in dunites to 80-83 mol% in pyroxene-bearing peridotites. The melts forming the dunites and the pyroxene-bearing peridotites could therefore have experienced variable degrees of fractional crystallization according to the following order: (1) olivine + accessory spinel (dunites), (2) olivine + pyroxene + accessory spinel (pyroxene-bearing peridotites). The development of pyroxene associated with slight diminishment of whole-rock and olivine Mg# may indeed also be related to crystallization of interstitial melt trapped among olivine grains (Barnes, 1986). However, NiO olivine compositions (Fig. 6) argue against formation of dunites and pyroxene-bearing peridotites through fractional crystallization and/or melt entrapment. Olivine-driven fractional crystallization is expected to produce a NiO decrease in residual melts and newly formed olivine (e.g., Niida, 1997) and, similarly, the process of melt entrapment should result in a slight NiO decrease in olivine. Conversely, olivine has slightly higher NiO in pyroxene-bearing peridotites than in dunites (0.11-0.14 wt% and 0.06-0.09 wt%, respectively).

The pyroxenites are chemically more evolved than the pyroxene-bearing peridotites. For instance, the forsterite content of olivine decreases (Fig. 6) from the pyroxene-bearing peridotites to the plagioclase-free pyroxenites (80-83 mol% and 78 mol%, respectively). In addition, orthopyroxene and clinopyroxene (Figs. 7 and 8) show Mg# and Al_2O_3 decreasing and increasing, respectively, from the peridotites to the pyroxenites. Furthermore, the Mg# decrease of clinopyroxene is associated with a TiO_2 increase. These olivine and pyroxene chemical variations could overall be related to a fractional crystallization process characterized by progressive replacement of olivine by pyroxenes in the segregating mineral assemblage. However, orthopyroxene is typically markedly more abundant than clinopyroxene in the pyroxenites (60-75 vol% and ≤20 vol%, respectively, in majority of selected samples) and that the high modal percentage of orthopyroxene with respect to clinopyroxene is not expected on the basis of experimental data, even if H_2O-rich basaltic melts and high pressure conditions are considered (e.g., Pilet et al., 2010; Nandedkar et al., 2014). In addition, the variations observed for LREE fractionation of amphiboles from the dunites, the pyroxene-bearing peridotites and the pyroxenites (La_N/Sm_N = 0.5-2.0, see also Fig. 11) argue against the idea that the peridotite-pyroxenite sequences formed by closed system fractional crystallization, even if associated with melt entrapment.

The abundant orthopyroxene crystallization shown by the pyroxenites could be enhanced by a SiO_2 melt increase produced by assimilation of lower crustal material. However, there are no geochemical evidence for the pyroxenites systematically having a higher extent of crustal component than the dunites and the pyroxene-bearing peridotites. For instance, the pyroxenites and the peridotites show overall similar variations in Nd-Sr isotopic compositions (Fig. 13, Table 7) and include amphiboles with similar variations in LREE fractionation (Fig. 11, Table 5). We therefore argue against a process of concomitant fractional crystallization and assimilation of crustal material for the origin of the peridotite-pyroxenite sequences, even if primary melts with different compositions were involved in the building of the peridotite-pyroxenite sequences.

Because the peridotite-pyroxenite sequences are permeated by amphibole-rich veins/dykes (see section 8.2), an alternative petrogenetic hypothesis is here proposed for the development of the peridotite-pyroxenite sequences, with the pyroxene-bearing peridotites and the pyroxenites forming in response to interaction of the dunites with amphibole-saturated melts (relatively rich in SiO_2 and H_2O) before complete solidification, thereby leading to olivine-consuming reactions. A similar petrogenetic scenario was envisaged for the "secondary peridotites" mantling the replacive dunites from the Chilas Complex (Kohistan), a suite of harzburgites, lherzolites, plagioclase-bearing lherzolites and olivine websterites included within gabbronorites and crystallized at ~0.7 GPa (Jagoutz et al., 2006; 2007; 2011). Concentric zoning of the Chilas ultramafic sequences (up to ten-of-meters-scale), expressed by an outward increase of pyroxene proportion mostly at the expenses of olivine, was attributed to infiltration of interstitial melts present in a super-solidus gabbronoritic crystal-mush during emplacement of the ultramafic rocks.

The major element chemical characteristics of Monte Capio-Alpe Cevia peridotite-pyroxenite sequences and the high modal proportion of orthopyroxene in the pyroxenites could therefore reflect a process of reactive migration of melts relatively rich in SiO_2- and H_2O within an olivine-rich matrix. Following this hypothesis, the pyroxenites formed in response to a reaction that developed orthopyroxene and amphibole mostly at the expenses of olivine, similar to what was proposed for the origin of hornblendite veins (reaction 2), and the melts residual after crystallization of the pyroxenites reacted with the olivine-rich matrix to give rise to the pyroxene-bearing peridotites. Because of its high H_2O contents, the migrating melts could have low viscosity, thereby favoring the reactive porous flow (Watson et al., 1990). In particular, the pyroxene-bearing peridotites could originate according to the following reaction:

(3) Ol 1 ± Cpx + SiO_2- and H_2O-rich melt = Ol 2 (Fo-depleted) + Opx + Amp ± residual melt

The change from reaction (2) to reaction (3) is essentially given by the preservation of olivine among products. Reactive migration of the SiO_2- and H_2O-rich melts through dunite grain

boundaries could only partly dissolve the original olivine grains, thereby explaining the relatively high NiO contents of olivine from pyroxene-bearing peridotites with respect to olivine from dunites, because NiO is incorporated into a minor olivine proportion (see also Niida 1997). The change in the product mineral assemblage (from pyroxenites to pyroxene-bearing peridotites) could be due to decreasing melt/rock ratios and decreasing SiO_2 contents of the migrating melts, which eventually led the melt reaction front terminating at the interface between the pyroxene-bearing peridotites and the dunites.

Because amphibole retains replacing relationships with respect to clinopyroxene (Fig. 3c), clinopyroxene was set among the reactants in reaction (3). The hypothetical process of olivine- and melt-consuming reactive porous flow could therefore occur in an olivine-rich matrix including negligible to minor amounts of clinopyroxene. The variability of clinopyroxene modal proportion therefore suggests an earlier magma evolution process controlled by segregation of olivine + accessory spinel, followed by separation of olivine + clinopyroxene + accessory spinel, in agreement with fractional crystallization experiments for H_2O-rich basaltic melts under high pressure conditions (Müntener and Ulmer, 2006). This material could subsequently experience reaction with migrating SiO_2- and H_2O-rich melts, which gave rise to orthopyroxene and amphibole. To conclude, the preferred petrogenetic hypothesis for the development of the Monte Capio-Alpe Cevia peridotite-pyroxenite sequences implies the early formation of an olivine-rich crystal mush and the subsequent reactive migration of SiO_2- and H_2O-rich melts through it. In the next discussion section, we will show that amphibole trace element compositions and whole-rock Nd-Sr isotopic compositions sustain this origin.

9.5 Evolution of the melts forming the peridotite-pyroxenite sequences: constraints from incompatible trace elements and Nd-Sr isotopic ratios

Although amphiboles from the peridotite-pyroxenite sequences show marked variations of incompatible trace elements (Fig. 11), they collectively yield rough positive correlations among La_N/Sm_N, Th/Y, Th/Nb and U/Ta values (Fig. 17). Because the basement metasedimentary rocks typically have high abundances of LREE, Th and U (Schnetger et al., 1994; see also Fig. 16), these correlations may be related to mantle melts experiencing different extents of crustal contamination. The rough correlations observed for amphibole incompatible trace element ratios may indeed also be reconciled with the hypothetical process of reactive melt migration, which implies consumption of olivine (and melt) and crystallization of orthopyroxene and amphibole. Olivine dissolution is expected to play a minor role in fractionating incompatible trace elements, because of the low olivine-melt partition coefficients (e.g., Zanetti et al., 2004; Spandler and O'Neill, 2010). Conversely, the concentrations of incompatible trace elements with respect to the segregating orthopyroxene-amphibole assemblage should increase in the residual melts with progression of the melt/rock reaction process, namely with decreasing melt/solid ratio. Hence, a melt residual after orthopyroxene and amphibole crystallization (i.e., residual melt 2 in equations 1 and 2) is expected to be LREE-enriched, because LREE are more incompatible than MREE in both orthopyroxene and amphibole (e.g., Davidson et al., 2013), and to have lower Th/Nb and U/Ta values in response to the compatibility of Nb and Ta in amphibole (cf. Tiepolo et al., 2007). Similarly, the Th/Y ratios should increase in the evolving melts, because Th is more incompatible than Y in the segregating orthopyroxene-amphibole assemblage.

There is no clear correlation between incompatible trace element amphibole ratios, rock-type and Nd-Sr isotopic compositions (Figs. 13 and 17). The two samples including amphiboles with the highest La_N/Sm_N, Th/Y, Th/Nb and U/Ta values (pyroxene-bearing peridotite MC8/1 and plagioclase-free pyroxenite MC22A, Table 5) have relatively low ε_{Nd}(290 Ma) and high $^{87}Sr/^{86}Sr$(290 Ma) (-4.0 to -4.7 and 0.7075 to 0.7071). These chemical characteristics collectively support the interpretation of these rocks recording a process of crustal contamination, because the basement metasediments typically show high concentrations of LREE, Th and U, and unradiogenic Nd and radiogenic Sr isotopic compositions (Voshage et al., 1990; Schnetger et al., 1994). However, plagioclase-bearing pyroxenite BC2A displays Nd-Sr isotopic compositions (ε_{Nd}(290 Ma) = -4.4 and $^{87}Sr/^{86}Sr$(290 Ma) = 0.7073) similar to those of pyroxene-bearing peridotite MC8/1 and plagioclase-free pyroxenite MC22A, but it includes an amphibole with relatively low La_N/Sm_N, Th/Y, Th/Nb and U/Ta values. Hence, the Monte Capio-Alpe Cevia peridotite-pyroxenite sequences have Nd-Sr isotopic variations that cannot be related to crustal contamination alone,

thereby suggesting involvement of primary melts with different Nd-Sr compositions.

Calculated REE compositions of melts in equilibrium with amphibole from the peridotite-pyroxenite sequences (Fig. 16) have chondrite-normalized patterns with LREE variably enriched over MREE (La_N/Sm_N = 2-12) and slight enrichment of HREE over MREE (Dy_N/Yb_N = 0.5-0.9). The latter geochemical characteristic is difficult to reconcile with a process of bulk assimilation of adjacent metasediments alone, because these rocks are characterized by nearly to flat MREE-HREE or by slight depletion of MREE with respect to HREE (Dy_N/Yb_N = 0.9-1.2). Bulk assimilation is also inconsistent with the four peridotite/pyroxenite samples including amphiboles with marked LREE enrichment (Fig. 17), because computed equilibrium melts are more LREE-enriched than the metasediments (La_N/Sm_N = 8-12 and 3-4, respectively). Note also that the enrichment of HREE over MREE in amphibole equilibrium melts cannot be achieved by melts derived by partial melting of the metasediments, which are expected to have Dy_N/Yb_N >1, because of the garnet stability in the residue (e.g., Hermann and Rubatto, 2009; Davidson et al., 2013). Amphibole fractionation conversely increases the Dy_N/Yb_N values of evolving residual melts, because MREE are more compatible in amphibole than HREE (see also Nandedkar et al., 2016). Note that the amphibole equilibrium melts show variable Dy_N/Yb_N irrespective of the rock type, thereby arguing once more against a process of closed system fractional crystallization leading to dunites and subsequently to pyroxene-bearing peridotites and pyroxenites. We conclude that the MREE-HREE variability of computed amphibole equilibrium melts supports the idea that the peridotite-pyroxenite sequences experienced, at least locally, reactive migration with melts that consumed olivine and crystallized amphibole and orthopyroxene.

10. Summary and conclusions

The Monte Capio-Alpe Cevia sequences are exposed in the lowermost continental crust of the Ivrea-Verbano Zone. They essentially consist of a peridotite core, with dunite in the center, mantled by minor orthopyroxene-dominated pyroxenites and subordinate hornblende gabbronorites. The growth of these sequences was associated with the late- to post-collisional, extensional phases of the Variscan orogeny (e.g., Klötzli et al., 2014), or with the rifting evolution leading to opening of the Jurassic Alpine Tethys (Denyszyn et al., 2018).

The Monte Capio-Alpe Cevia dunite cores show a chemically evolved signature. We did not find any clear evidence for the Monte Capio-Alpe Cevia dunites being of replacive mantle nature, thereby suggesting dunite formation by cooling of olivine-saturated melt lenses intruding the lower continental crust. Nonetheless, the dunites may have acted as conduits for ascending mantle melts. The chemically evolved signature of the melts in equilibrium with the dunites (Mg# ≤0.62) reflects earlier crystallization of chemically primitive dunites at lower levels, or olivine fractionation within the dunites during melt ascent.

The edges of the Monte Capio-Alpe Cevia sequences were most likely formed by reaction of a semi-consolidated olivine-rich crystal mush with migrating melts relatively rich in SiO_2 and H2O, which developed orthopyroxene and amphibole at the expenses of olivine. These melts may be reconciled with those feeding the amphibole-rich veins and dykes crosscutting the peridotite-pyroxenite sequences, which had 49-53 wt% SiO_2, low Mg# (about 51), and a REE signature similar to modern E-MORB.

The melts involved in the building of the Monte Capio-Alpe Cevia peridotite-pyroxenite sequences show significant variations in Nd-Sr isotopic compositions and in the fractionations of LREE, Th and U with respect to Y, Nb and Ta. The amphibole-rich veins and dykes also indicate that melts had different H_2O contents and variable Pb and Sr fractionations with respect to LREE-MREE. Taken as a whole, these melt compositional variations at least partly reflect multiple injections of primary melts derived from a compositionally heterogeneous source, most likely a subcontinental lithospheric mantle variably metasomatized during the Variscan subduction. In addition, the Monte Capio-Alpe Cevia mantle melts probably experienced, at least locally, assimilation of material released by metasedimentary rocks in response to melt-basement interaction during melt ascent and/or emplacement.

11. References

Allègre, C. J., & Turcotte, D. L. (1986). Implications of a two-component marble-cake mantle. Nature, 323(6084), 123.

Annen, C., Blundy, J. D. & Sparks, R. S. J. (2006). The genesis of intermediate and silicic magmas in deep crustal hot zones. Journal of Petrology 47,505-539.

Barboza SA, Bergantz GW (2000). Metamorphism and anatexis in the Mafic Complex contact aureole, Ivrea zone, northern Italy. J. Petrol 41:1307–1327

Bertolani, M., & Loschi-Ghittoni, A. G. (1979). La zona a ultrabasiti della Rocca D'Argimonia nelle Prealpi Biellesi. La petrografia. Rend Soc Ital Mineral Petr, 35, 791-813.

Bindeman, I. N., Davis, A. M., & Drake, M. J. (1998). Ion microprobe study of plagioclase-basalt partition experiments at natural concentration levels of trace elements. Geochimica et Cosmochimica Acta, 62(7), 1175-1193.

Bodinier, J. L., Garrido, C. J., Chanefo, I., Bruguier, O., & Gervilla, F. (2008). Origin of pyroxenite–peridotite veined mantle by refertilization reactions: evidence from the Ronda peridotite (Southern Spain). Journal of Petrology, 49(5), 999-1025.

Boriani A, Burlini L, Sacchi R (1990) The Cossato–Mergozzo–Brissago Line and the Pogallo Line (Southern Alps, Northern Italy) and their relationships with the late-Hercynian magmatic and metamorphic events. Tectonophysics 182:92–102

Boriani, A., and Giobbi, E., (2004), Does the basement of western southern Alps display a tilted section through the continental crust? A review and discussion: Periodico di Mineralogia, v. 73, p. 5–22.

Brey, G. P., & Köhler, T. (1990). Geothermobarometry in four-phase lherzolites II. New thermobarometers, and practical assessment of existing thermobarometers. Journal of Petrology, 31(6), 1353-1378.

Burg, J. P., Bodinier, J. L., Chaudhry, S., Hussain, S., & Dawood, H. (1998). Infra-arc mantle-crust transition and intra-arc mantle diapirs in the Kohistan Complex (Pakistani Himalaya): petro-structural evidence. Terra Nova-Oxford, 10(2), 74-80.

Denyszyn, S. W., Fiorentini, M. L., Maas, R., & Dering, G. (2018). A bigger tent for CAMP. Geology, 46(9), 823-826.

Ewing, T. A., Hermann, J., and Rubatto, D. (2013). The robustness of the Zr-in-rutile and Ti-in-zircon thermometers during high-temperature metamorphism (Ivrea-Verbano Zone, northern Italy), Contrib. Mineral. Petr., 165, 757-779.

Ferrario, A., Garuti, G., Rossi, A., & Sighinolfi, G. P. (1983). Petrographic and metallogenic outlines of the "La Balma-M. Capio" ultramafic-mafic body (Ivrea-Verbano basic complex, NW Italian Alps). In Mineral Deposits of the Alps and of the Alpine Epoch in Europe (pp. 28-40). Springer, Berlin, Heidelberg.

Fiorentini, M. L., LaFlamme, C., Denyszyn, S., Mole, D., Maas, R., Locmelis, M., & Bui, T. H. (2018). Post-collisional alkaline magmatism as gateway for metal and sulfur enrichment of the continental lower crust. Geochimica et Cosmochimica Acta, 223, 175-197.

Garuti, G., Bea, F., Zaccarini, F., & Montero, P. (2001). Age, geochemistry and petrogenesis of the ultramafic pipes in the Ivrea Zone, NW Italy. Journal of Petrology, 42(2), 433-457.

Godard, M., Awaji, S., Hansen, H., Hellebrand, E., Brunelli, D., Johnson, K., Yamasaki T., Maeda J., Abratis M., Christie D., Kato, Y., Mariet C. & Rosner M., (2009). Geochemistry of a long in-situ section of intrusive slow-spread oceanic lithosphere: Results from IODP Site U1309 (Atlantis Massif, 30 N Mid-Atlantic-Ridge). Earth and Planetary Science Letters, 279(1), 110-122.

Grégoire, D. C., Miller-Ihli, N. J., & Sturgeon, R. E. (1994). Direct analysis of solids by ultrasonic slurry electrothermal vaporization inductively coupled plasma mass spectrometry. Journal of Analytical Atomic Spectrometry, 9(5), 605-610.

Guergouz, C., Martin, L., Vanderhaeghe, O., Thébaud, N., & Fiorentini, M. (2018). Zircon and monazite petrochronologic record of prolonged amphibolite to granulite facies metamorphism in the Ivrea-Verbano and Strona-Ceneri Zones, NW Italy. Lithos, 308, 1-18.

Hacker, B. R., Mehl, L., Kelemen, P. B., Rioux, M., Behn, M. D., & Luffi, P. (2008). Reconstruction of the Talkeetna intraoceanic arc of Alaska through thermobarometry. Journal of Geophysical Research: Solid Earth, 113(B3).

Hamada, M., & Fujii, T. (2007). H2O-rich island arc low-K tholeiite magma inferred from Ca-rich plagioclase-melt inclusion equilibria. Geochemical Journal, 41(6), 437-461.

Hellebrand, E., Snow, J. E., Mostefaoui, S., & Hoppe, P. (2005). Trace element distribution between orthopyroxene and clinopyroxene in peridotites from the Gakkel Ridge: a SIMS and NanoSIMS study. Contributions to Mineralogy and Petrology, 150(5), 486-504.

Helmy, H. M., El-Rahman, Y. M. A., Yoshikawa, M., Shibata, T., Arai, S., Tamura, A., & Kagami, H. (2014). Petrology and Sm-Nd dating of the Genina Gharbia Alaskan-type complex (Egypt): insights into deep levels of Neoproterozoic island arcs. Lithos, 198, 263-280

Hermann, J., Rubatto, D., (2009). Accessory phase control on the trace element signature of sediments melts in subduction zones. Chemical Geology 265, 512–526.

Hildreth, W., & Moorbath, S. (1988). Crustal contributions to arc magmatism in the Andes of central Chile. Contributions to mineralogy and petrology, 98(4), 455-489.

Himmelberg, G. R., & Loney, R. A. (1995). Characteristics and petrogenesis of Alaskan-type ultramafic-mafic intrusions, southeastern Alaska (Vol. 56). US Government Printing Office.

Holland, T., & Blundy, J. (1994). Non-ideal interactions in calcic amphiboles and their bearing on amphibole-plagioclase thermometry. Contributions to mineralogy and petrology, 116(4), 433-447.

Irvine, T. N. (1974). Petrology of the Duke Island ultramafic complex, southeastern Alaska (Vol. 138). Geological Society of America.

Jagoutz, O., Müntener, O., Burg, J. P., Ulmer, P., & Jagoutz, E. (2006). Lower continental crust formation through focused flow in km-scale melt conduits: The zoned ultramafic bodies of the Chilas Complex in the Kohistan island arc (NW Pakistan). Earth and Planetary Science Letters, 242(3-4), 320-342.

Jagoutz, O., Müntener, O., Schmidt, M. W., & Burg, J. P. (2011). The roles of flux-and decompression melting and their respective fractionation lines for continental crust formation: Evidence from the Kohistan arc. Earth and Planetary Science Letters, 303(1-2), 25-36.

Jagoutz, O., Müntener, O., Ulmer, P., Pettke, T., Burg, J. P., Dawood, H., & Hussain, S. (2007). Petrology and mineral chemistry of lower crustal intrusions: the Chilas Complex, Kohistan (NW Pakistan). Journal of Petrology, 48(10), 1895-1953.

Jeffries, T. E., Jackson, S. E., & Longerich, H. P. (1998). Application of a frequency quintupled Nd: YAG source (λ= 213 nm) for laser ablation inductively coupled plasma mass spectrometric analysis of minerals. Journal of Analytical Atomic Spectrometry, 13(9), 935-940.

Jull, M., & Kelemen, P. Á. (2001). On the conditions for lower crustal convective instability. Journal of Geophysical Research: Solid Earth, 106(B4), 6423-6446.

Klötzli US, Sinigoi S, Quick JE, Demarchi G, Tassinari CCG, Sato K, Günes Z (2014) Duration of igneous activity in the Sesia Magmatic System and implications for high-temperature metamorphism in the Ivrea-Verbano deep crust. Lithos 206–207:19–33

Kornbrost, J., Piboule, M., Roden, M., & Tabit, A. (1990). Corundum-bearing garnet clinopyroxenites at Beni Bousera (Morocco): original plagioclase-rich gabbros recrystallized at depth within the mantle?. Journal of Petrology, 31(3), 717-745.

Kunz, B. E., Johnson, T. E., White, R. W., & Redler, C. (2014). Partial melting of metabasic rocks in Val Strona di Omegna, Ivrea Zone, northern Italy. Lithos, 190, 1-12.

Locmelis, M., Fiorentini, M. L., Rushmer, T., Arevalo Jr, R., Adam, J., & Denyszyn, S. W. (2016). Sulfur and metal fertilization of the lower continental crust. Lithos, 244, 74-93.

Loucks, R. R. (1996). A precise olivine-augite Mg-Fe-exchange geothermometer. Contributions to Mineralogy and Petrology, 125(2-3), 140-150.

Lyubetskaya, T., & Korenaga, J. (2007). Chemical composition of Earth's primitive mantle and its variance: 1. Method and results. Journal of Geophysical Research: Solid Earth, 112(B3).

Mazzucchelli M., Zanetti A., Rivalenti G., Vannucci R., Correia C.T., Gaeta Tassinari C.C. (2010) Age and geochemistry of mantle peridotites and diorite dykes from the Baldissero body: insights into the Paleozoic-Mesozoic evolution of the Southern Alps. Lithos 119:485–500

Montanini, A., & Tribuzio, R. (2001). Gabbro-derived granulites from the Northern Apennines (Italy): evidence for lower-crustal emplacement of tholeiitic liquids in post-Variscan times. Journal of Petrology, 42(12), 2259-2277.

Montanini, A., & Tribuzio, R. (2015). Evolution of recycled crust within the mantle: constraints from the garnet pyroxenites of the External Ligurian ophiolites (northern Apennines, Italy). Geology, 43(10), 911-914.

Müntener, O., Kelemen, P. B., & Grove, T. L. (2001). The role of H2O and composition on the genesis of igneous pyroxenites: An experimental study. Contrib. Mineral. Petrol, 141, 643-658.

Müntener, O., & Ulmer, P. (2006). Experimentally derived high-pressure cumulates from hydrous arc magmas and consequences for the seismic velocity structure of lower arc crust. Geophysical Research Letters, 33(21).

Nandedkar, R. H., Ulmer, P., & Müntener, O. (2014). Fractional crystallization of primitive, hydrous arc magmas: an experimental study at 0.7 GPa. Contributions to Mineralogy and Petrology, 167(6), 1015.

Niida, K. (1997). 12, Mineralogy of Mark peridotites: replacement through magma chaneling examined from Hole 920D, Mark area. In Proceedings of Ocean Drilling Program (Vol. 153).

Obata, M. (1974). The iron-magnesium partitioning between naturally occurring coexisting olivine and Ca-rich clinopyroxene: an application of the simple mixture model to olivine solid solution. Bull. Soc. fr. MinCristallogr., 97, 101-107.

Panjasawatwong, Y., Danyushevsky, L. V., Crawford, A. J., & Harris, K. L. (1995). An experimental study of the effects of melt composition on plagioclase-melt equilibria at 5 and 10 kbar: implications for the origin of magmatic high-An plagioclase. Contributions to Mineralogy and Petrology, 118(4), 420-432.

Peressini G, Quick JE, Sinigoi S, Hofmann AW, Fanning M. (2007) Duration of a large mafic intrusion and heat transfer in the lower crust: a SHRIMP U-Pb Zircon Study in the Ivrea-Verbano Zone (Western Alps, Italy). J Petrol 48:1185–1218

Pilet, S., Ulmer, P., & Villiger, S. (2010). Liquid line of descent of a basanitic liquid at 1.5 GPa: constraints on the formation of metasomatic veins. Contributions to Mineralogy and Petrology, 159(5), 621-643.

Polat, A., Fryer, B. J., Samson, I. M., Weisener, C., Appel, P. W., Frei, R., & Windley, B. F. (2012). Geochemistry of ultramafic rocks and hornblendite veins in the Fiskenæsset layered anorthosite complex, SW Greenland: Evidence for hydrous upper mantle in the Archean. Precambrian Research, 214, 124-153.

Putirka, K. (2016). Amphibole thermometers and barometers for igneous systems and some implications for eruption mechanisms of felsic magmas at arc volcanoes. American Mineralogist, 101(4), 841-858.

Quick J.E., Sinigoi S., Mayer A. (1995) Emplacement of mantle peridotite in the lower continental crust, Ivrea-Verbano zone, northwest Italy. Geology 23:739–742

Quick J.E., Sinigoi S., Snoke A.W., Kalakay T.J., Mayer A., Peressini G. (2003). Geologic Map of the Southern Ivrea-Verbano Zone, Northwestern Italy, Geologic Investigations Series Map I-2776 and booklet [22p]. Government Printing Office, US Geological Survey, U.S

Quick J. E., Sinigoi, S., & Mayer, A. (1994). Emplacement dynamics of a large mafic intrusion in the lower crust, Ivrea-Verbano Zone, northern Italy. Journal of Geophysical Research: Solid Earth, 99(B11), 21559-21573.

Rampone, E., Piccardo, G. B., Vannucci, R., Bottazzi, P., & Ottolini, L. (1993). Subsolidus reactions monitored by trace element partitioning: the spinel-to plagioclase-facies transition in mantle peridotites. Contributions to Mineralogy and Petrology, 115(1), 1-17.

Redler C., Johnson TE, White RW, Kunz BE (2012). Phase equilibrium constraints on a deep crustal metamorphic field gradient: metapelitic rocks from the Ivrea Zone (NW Italy). J Metamorph Geol 30:235-254

Redler, C., White, R. W., & Johnson, T. E. (2013). Migmatites in the Ivrea Zone (NW Italy): Constraints on partial melting and melt loss in metasedimentary rocks from Val Strona di Omegna. Lithos, 175, 40-53.

Roeder, P. L., & Emslie, R. (1970). Olivine-liquid equilibrium. Contributions to mineralogy and petrology, 29(4), 275-289.

Rutter, E., Brodie, K., James, T., Blundell, D. J., & Waltham, D. A. (2003). Seismic Modeling of Lower and Mid-Crustal Structure as Exemplified by the Massiccio dei Laghi (Ivrea-Verbano Zone and Serie dei Laghi) Crustal Section, Northwestern Italy. In Heterogeneity in the Crust and Upper Mantle (pp. 67-97). Springer US.

Rutter, E. H., Brodie, K. H., & Evans, P. J. (1993). Structural geometry, lower crustal magmatic underplating and lithospheric stretching in the Ivrea-Verbano zone, northern Italy. Journal of Structural Geology, 15(3-5), 647-662.

Schmid, S. M., Kissling, E., Diehl, T., van Hinsbergen, D. J., & Molli, G. (2017). Ivrea mantle wedge, arc of the Western Alps, and kinematic evolution of the Alps–Apennines orogenic system. Swiss Journal of Geosciences, 110(2), 581-612.

Schnetger, B. (1994). Partial melting during the evolution of the amphibolite-to granulite-facies gneisses of the Ivrea Zone, northern Italy. Chemical Geology, 113(1-2), 71-101.

Shimizu, K., Liang, Y., Sun, C., Jackson, C. R., & Saal, A. E. (2017). Parameterized lattice strain models for REE partitioning between amphibole and silicate melt. American Mineralogist: Journal of Earth and Planetary Materials, 102(11), 2254-2267.

Siegesmund, S., Layer, P., Dunkl, I., Vollbrecht, A., Steenken, A., Wemmer, K., & Ahrendt, H. (2008). Exhumation and deformation history of the lower crustal section of the Valstrona di Omegna in the Ivrea Zone, southern Alps. Geological Society, London, Special Publications, 298(1), 45-68.

Sinigoi S, Quick JE, Mayer A, Budahn J (1996) Influence of stretching and density contrasts on the chemical evolution of continental magmas: an example from the Ivrea-Verbano zone. Contrib. Mineral. Petrol 123:238–250

Sisson, T. W., & Grove, T. L. (1993). Experimental investigations of the role of H 2 O in calc-alkaline differentiation and subduction zone magmatism. Contributions to mineralogy and petrology, 113(2), 143-166.

Solano, J. M. S., Jackson, M. D., Sparks, R. S. J., Blundy, J. D., & Annen, C. (2012). Melt segregation in deep crustal hot zones: a mechanism for chemical differentiation, crustal assimilation and the formation of evolved magmas. Journal of Petrology, 53(10), 1999-2026.

Spandler, C., & O'Neill, H. S. C. (2010). Diffusion and partition coefficients of minor and trace elements in San Carlos olivine at 1,300 C with some geochemical implications. Contributions to Mineralogy and Petrology, 159(6), 791-818.

Su, B., Chen, Y., Guo, S., & Liu, J. (2016). Origins of orogenic dunites: petrology, geochemistry, and implications. Gondwana Research, 29(1), 41-59.

Sun, S. S., & McDonough, W. S. (1989). Chemical and isotopic systematics of oceanic basalts: implications for mantle composition and processes. Geological Society, London, Special Publications, 42(1), 313-345.

Takazawa, E., Frey, F., Shimizu, N., & Obata, M. (1996). Evolution of the Horoman peridotite (Hokkaido, Japan): implications from pyroxene compositions. Chemical Geology, 134(1), 3-26.

Tiepolo, M., Oberti, R., Zanetti, A., Vannucci, R., & Foley, S. F. (2007). Trace-element partitioning between amphibole and silicate melt. Reviews in mineralogy and geochemistry, 67(1), 417-452.

Ulmer, P., Callegari, E., & Sonderegger, U. C. (1983). Genesis of the mafic and ultramafic rocks and their genetical relations to the tonalitic-trondhjemitic granitoids of the southern part of the Adamello batholith (Northern Italy). Memorie della Società Geologica Italiana, 26(1), 171-222.

Van Orman, J. A., Grove, T. L., & Shimizu, N. (2001). Rare earth element diffusion in diopside: influence of temperature, pressure, and ionic radius, and an elastic model for diffusion in silicates. Contributions to Mineralogy and Petrology, 141(6), 687-703.

Voshage, H., Hofmann, A. W., Mazzucchelli, M., Rivalenti, G., Sinigoi, S., Raczek, I., & Demarchi, G. (1990). Isotopic evidence from the Ivrea Zone for a hybrid lower crust formed by magmatic underplating. Nature, 347(6295), 731-736.

Watson, E. B. (1990). Distribution of fluid in the continental mantle. Continental mantle, 111-125.

Witt-Eickschen, G., & O'Neill, H. S. C. (2005). The effect of temperature on the equilibrium distribution of trace elements between clinopyroxene, orthopyroxene, olivine and spinel in upper mantle peridotite. Chemical Geology, 221(1-2), 65-101.

Yao, L., Sun, C., & Liang, Y. (2012). A parameterized model for REE distribution between low-Ca pyroxene and basaltic melts with applications to REE partitioning in low-Ca pyroxene along a mantle adiabat and during pyroxenite-derived melt and peridotite interaction. Contributions to Mineralogy and Petrology, 164(2), 261-280.

Zaccarini, F., Garuti, G., Fiorentini, M. L., Locmelis, M., Kollegger, P., & Thalhammer, O. A. (2014). Mineralogical hosts of platinum group elements (PGE) and rhenium in the magmatic Ni-Fe-Cu sulfide deposits of the Ivrea Verbano Zone (Italy): An electron microprobe study. Neues Jahrbuch für Mineralogie-Abhandlungen: Journal of Mineralogy and Geochemistry, 191(2), 169-187.

Zanetti A., Giovanardi T., Langone A., Tiepolo M., Wu F.Y., Dallai L., Mazzucchelli M. (2016). Origin and age of zircon-bearing chromitite layers from the Finero phlogopite peridotite (Ivrea-Verbano Zone, Western Alps) and geodynamic consequences. Lithos, 262, pp. 58-74

Zanetti, A., Tiepolo, M., Oberti, R., & Vannucci, R. (2004). Trace-element partitioning in olivine: modelling of a complete data set from a synthetic hydrous basanite melt. Lithos, 75(1-2), 39-54.

APPENDIX
TABLE DATA

Sample	AC1D	BC4A	MC27B	MC8/3	MC8/1	MC25A	BC5B	MC8B	MC22A	MC20/1	BC2A	MC26A	MC24A	MC27/1 B	MC20/2	AC1B	MC4B	MC27A	MC7/4
Rock Type	Dunite	Dunite	Dunite	-bearing Perido	-bearing Perido	-bearing Perido	-bearing Perido	l-free Pyroxenit	l-free Pyroxenit	l-free Pyroxenit	bearing Pyroxe	bearing Pyroxe	bearing Pyroxe	Hornblendite	Hbl-rich gabbro	Hbl-rich gabbro	Hbl-rich gabbro	Ibl Gabbronorit	Ibl Gabbronorit
Major elements (wt%)																			
SiO_2	38.3	38.4	38.5	38.7	39.2	39.0	43.1	46.4	51.2	50.0	51.9	50.8	50.1	42.5	41.1	41.5	41.7	46.0	46.4
TiO_2	0.04	0.04	0.08	0.06	0.11	0.06	0.30	1.26	0.34	0.36	0.36	0.34	0.38	1.44	2.80	2.86	3.03	1.54	1.65
Al_2O_3	1.33	1.24	1.69	1.66	1.82	1.38	3.37	7.50	4.77	4.90	5.20	6.74	6.83	13.8	17.3	19.6	18.6	17.2	17.7
Fe_2O_3 (T)	16.7	16.5	16.7	16.2	17.5	17.0	14.7	12.5	13.6	12.4	12.3	13.9	13.6	8.89	9.47	8.39	9.01	9.73	9.41
MnO	0.19	0.20	0.20	0.19	0.20	0.19	0.20	0.20	0.22	0.20	0.20	0.21	0.21	0.11	0.15	0.10	0.10	0.14	0.14
MgO	42.1	42.2	40.3	41.2	40.4	39.3	31.4	22.6	26.0	25.6	24.0	23.5	23.8	18.9	12.9	10.8	11.6	9.73	9.90
CaO	0.38	0.47	0.73	0.76	1.11	1.00	6.20	7.44	2.89	4.78	4.33	3.67	3.39	10.2	11.6	12.4	12.0	11.3	11.7
Na_2O	0.08	0.02	0.07	0.05	0.10	0.08	0.17	0.98	0.16	0.17	0.20	0.25	0.32	1.87	2.29	2.45	2.57	2.03	2.51
K_2O	0.01	< 0.01	< 0.01	< 0.01	0.02	< 0.01	< 0.01	0.18	0.02	0.01	< 0.01	0.02	0.03	0.28	0.51	0.39	0.39	0.36	0.21
P_2O_5	0.01	< 0.01	0.01	0.01	< 0.01	0.02	0.01	0.01	< 0.01	0.01	< 0.01	< 0.01	< 0.01	< 0.01	0.02	< 0.01	< 0.01	0.03	0.03
LOI	0.04	0.66	0.40	0.33	-0.12	0.40	0.93	1.22	0.95	1.73	0.98	1.17	1.81	1.80	2.00	1.75	0.65	1.91	1.13
Total	99.1	99.6	98.7	99.1	100	98.5	100	100	100	100	99.5	101	101	99.6	100	100	99.6	100	101
Mg#	83.4	83.5	82.7	83.4	82.0	82.1	80.9	78.1	79.1	80.4	79.4	77.0	77.6	80.8	73.0	71.9	71.8	66.5	67.6
Ca#	84.0	96.3	92.0	94.4	92.5	93.3	97.6	89.4	95.2	96.9	96.0	94.2	92.1	85.7	84.8	84.8	83.8	86.0	83.8

Table 2: Whole rock major element compositions of selected samples.

	Olivine																	
Sample	AC1D		BC4A		MC27B		MC27/1 A		MC8/3		MC8/1		MC25A		BC5B		MC8B		MC22A	
Rock Type	Dunite		Dunite		Dunite		Dunite		Px-bearing Peridotite		Px-bearing Peridotite		Px-bearing Peridotite		Px-bearing Peridotite		Pl-free Pyroxenite		Pl-free Pyroxenite	
n.	9	std	16	std	14	std	5	std	17	std	7	std	14	std	6	std	5	std	7	std
SiO2	39.7	0.54	39.8	1.14	39.9	1.13	40.3	0.25	39.6	1.10	38.8	1.03	39.2	0.75	39.8	1.31	39.5	0.73	38.9	0.28
TiO2	0.02	0.03	0.02	0.03	0.02	0.02	0.01	0.01	0.02	0.03	0.02	0.03	0.04	0.03	0.01	0.01	0.03	0.03	0.01	0.03
Al2O3	0.02	0.03	0.02	0.03	0.01	0.02	0.00	0.01	0.01	0.01	0.02	0.02	0.01	0.02	0.02	0.02	0.00	0.00	0.00	0.00
Cr2O3	0.03	0.04	0.01	0.02	0.01	0.01	0.02	0.02	0.02	0.02	0.01	0.01	0.01	0.02	0.01	0.02	0.01	0.02	0.01	0.02
FeO	14.9	0.58	15.3	0.30	15.4	0.32	16.2	0.42	16.1	0.29	16.9	0.34	16.0	0.67	19.0	0.45	20.9	0.39	20.4	0.53
MnO	0.22	0.08	0.23	0.06	0.23	0.08	0.21	0.04	0.20	0.04	0.18	0.06	0.20	0.06	0.27	0.04	0.25	0.05	0.23	0.02
NiO	0.06	0.03	0.09	0.04	0.08	0.05	0.09	0.06	0.14	0.05	0.11	0.03	0.12	0.04	0.11	0.04	0.07	0.04	0.05	0.03
MgO	45.4	1.07	45.0	2.05	45.1	0.87	44.9	0.38	45.1	0.80	44.6	1.42	44.5	2.07	41.6	0.93	40.8	1.20	41.0	0.50
CaO	0.04	0.03	0.03	0.02	0.03	0.02	0.01	0.01	0.02	0.02	0.03	0.03	0.04	0.07	0.03	0.01	0.02	0.01	0.00	0.01
Na2O	0.06	0.03	0.04	0.05	0.05	0.06	0.01	0.01	0.01	0.01	0.12	0.09	0.08	0.17	0.06	0.07	0.06	0.12	0.00	0.01
K2O	0.02	0.02	0.02	0.02	0.01	0.01	0.00	0.01	0.00	0.00	0.05	0.04	0.03	0.05	0.04	0.03	0.02	0.02	0.00	0.00
Total	100	1.46	100	1.81	101	1.75	102	0.10	101	1.69	101	1.85	100	2.03	101	1.28	102	1.14	101	0.32
Fo (mol%)	84.5	0.62	83.9	0.72	83.9	0.45	83.2	0.47	83.3	0.37	82.5	0.51	83.2	0.52	79.6	0.66	77.7	0.81	78.1	0.64

Table 3: a) Major element olivine compositions. b) Major element orthopyroxene compositions. c) Major element clinopyroxene compositions. d) Major element amphibole compositions. e) Major element spinel compositions. f) Major element plagioclase compositions.

	Orthopyroxene																							
Sample	MC8/3		MC25A		BC5B		MC8B		MC22A		MC20/1		MC26A		BC2A		MC24A		MC27/1 B		MC27A		MC7/4	
Rock Type	Px-bearing Peridotite		Px-bearing Peridotite		Px-bearing Peridotite		Pl-free Pyroxenite		Pl-free Pyroxenite		Pl-free Pyroxenite		Pl-bearing Pyroxenite		Pl-bearing Pyroxenite		Pl-bearing Pyroxenite		Hornblendite		Hornblende Gabbronorite		Hornblende Gabbronorite	
n.	7	std	7	std	6	std	7	std	9	std	9	std	10	std	8	std	6	std	12	std	7	std	3	std
SiO2	56.0	0.88	55.7	0.46	55.3	0.78	54.7	2.43	53.8	0.34	53.4	0.84	53.9	0.54	53.6	0.86	53.2	0.38	54.7	0.44	53.9	0.95	53.2	0.71
TiO2	0.10	0.03	0.12	0.03	0.15	0.07	0.17	0.04	0.16	0.04	0.18	0.07	0.15	0.07	0.12	0.04	0.16	0.10	0.14	0.04	0.08	0.04	0.11	0.03
Al2O3	1.87	0.86	2.62	0.20	3.21	0.67	2.99	0.30	3.37	0.10	4.37	0.47	4.03	0.41	5.14	0.30	4.79	0.30	4.40	0.46	3.06	0.35	2.20	0.54
Cr2O3	0.14	0.08	0.21	0.04	0.10	0.03	0.10	0.05	0.15	0.04	0.33	0.08	0.26	0.03	0.22	0.04	0.16	0.03	0.10	0.07	0.05	0.03	0.02	0.03
FeO	10.7	0.15	10.8	0.15	12.1	0.23	13.2	0.18	12.6	0.13	12.2	0.54	13.9	0.36	12.6	0.30	14.2	0.56	11.0	0.60	16.9	0.94	20.3	0.58
MnO	0.26	0.03	0.22	0.04	0.21	0.09	0.34	0.07	0.24	0.03	0.23	0.07	0.23	0.08	0.25	0.04	0.27	0.12	0.27	0.03	0.41	0.05	0.46	0.05
NiO	0.04	0.02	0.05	0.01	0.02	0.02	0.02	0.02	0.02	0.03	0.02	0.03	0.03	0.04	0.04	0.04	0.05	0.04	0.03	0.04	0.01	0.01	0.00	0.00
MgO	31.7	0.31	31.4	0.30	29.7	1.23	28.4	0.70	28.9	0.26	29.4	0.84	28.4	0.47	28.3	0.64	27.6	0.70	30.3	0.69	25.9	0.69	23.8	0.20
CaO	0.30	0.08	0.38	0.05	0.39	0.03	0.45	0.07	0.38	0.03	0.45	0.08	0.35	0.06	0.33	0.07	0.35	0.04	0.41	0.14	0.42	0.05	0.46	0.07
Na2O	0.01	0.01	0.02	0.02	0.46	0.99	0.04	0.06	0.01	0.01	0.03	0.03	0.03	0.03	0.05	0.04	0.04	0.03	0.01	0.01	0.04	0.03	0.02	0.02
K2O	0.01	0.00	0.01	0.01	0.03	0.03	0.02	0.02	0.00	0.00	0.01	0.01	0.01	0.01	0.02	0.01	0.02	0.01	0.00	0.00	0.02	0.02	0.01	0.00
Total	101	1.31	101	0.61	102	1.26	100	2.67	99.7	0.45	101	0.57	101	0.46	101	1.53	101	1.19	101	0.29	101	0.66	101	0.33
Mg#	84.1	0.20	83.9	0.18	81.5	0.48	79.3	0.48	80.3	0.13	81.1	1.00	78.5	0.52	80.0	0.54	77.6	0.29	83.0	1.07	73.2	1.47	67.7	0.79

Table 3: continued

	Clinopyroxene																					
Sample	BC4A		MC8/1		MC25A		BC5B		MC8B		MC22A		MC20/1		MC26A		BC2A		MC7/4	
Rock Type	Dunite		Px-bearing Peridotite		Px-bearing Peridotite		Px-bearing Peridotite		Pl-free Pyroxenite		Pl-free Pyroxenite		Pl-free Pyroxenite		Pl-bearing Pyroxenite		Pl-bearing Pyroxenite		Hornblende Gabbronorite	
n.	8	std	3	std	9	std	2	std	3	std	4	std	9	std	5	std	4	std	3	std		
SiO2	53.2	1.26	52.6	0.75	52.8	1.04	53.1	-	51.6	0.35	52.8	0.39	50.4	0.65	50.6	0.93	50.7	1.07	50.9	0.59		
TiO2	0.43	0.19	0.55	0.18	0.32	0.09	0.57	-	0.92	0.13	0.36	0.02	0.85	0.11	0.80	0.14	0.74	0.09	0.84	0.11		
Al2O3	2.02	0.69	3.02	0.71	1.79	0.66	2.88	-	4.35	0.52	1.98	0.24	5.52	0.38	5.08	1.20	5.51	1.06	4.71	0.49		
Cr2O3	0.21	0.11	0.36	0.16	0.21	0.17	0.07	-	0.15	0.07	0.10	0.02	0.52	0.08	0.40	0.04	0.34	0.05	0.05	0.02		
FeO	2.60	0.30	3.71	0.22	2.99	0.38	3.59	-	4.63	0.24	3.70	0.10	3.86	0.28	4.35	0.25	3.94	0.10	6.68	0.22		
MnO	0.07	0.02	0.03	0.02	0.08	0.03	0.11	-	0.19	0.01	0.07	0.03	0.12	0.06	0.11	0.04	0.12	0.03	0.19	0.05		
NiO	0.01	0.01	0.03	0.03	0.04	0.03	0.02	-	0.02	0.03	0.03	0.02	0.02	0.02	0.03	0.02	0.03	0.04	0.01	0.01		
MgO	16.6	0.31	16.0	0.23	16.5	0.47	14.7	-	15.3	0.32	16.2	0.14	14.6	0.43	14.6	0.42	14.2	0.50	13.0	0.22		
CaO	24.8	0.35	23.6	0.23	24.7	0.39	23.3	-	23.5	0.28	23.7	0.10	23.4	0.43	23.4	0.26	23.1	0.13	22.2	0.50		
Na2O	0.11	0.05	0.26	0.07	0.13	0.05	0.25	-	0.24	0.02	0.11	0.02	0.32	0.08	0.37	0.09	0.38	0.03	0.71	0.14		
K2O	0.01	0.01	0.01	0.01	0.01	0.01	0.07	-	0.02	0.01	0.01	0.01	0.02	0.02	0.00	0.01	0.01	0.01	0.01	0.00		
Total	100	0.44	100	0.33	99.6	0.75	98.7	-	101	0.24	99.0	0.42	99.6	0.76	99.7	0.48	99.1	0.80	99.2	0.80		
Mg#	91.9	0.94	88.5	0.71	90.8	1.27	88.0	-	85.5	0.47	88.6	0.36	87.1	1.03	85.7	0.99	86.5	0.57	77.6	0.81		

Table 3: Continued

	Amphibole																			
Sample	BC4A		MC27B		MC8/3		MC8/1		MC25A		BC5B		MC8B		MC22A		MC20/1		MC26A	
Rock Type	Dunite		Dunite		Px-bearing Peridotite		Px-bearing Peridotite		Px-bearing Peridotite		Px-bearing Peridotite		Pl-free Pyroxenite		Pl-free Pyroxenite		Pl-free Pyroxenite		Pl-bearing Pyroxenite	
n.	15	std	4	std	14	std	7	std	4	std	4	std	3	std	10	std	3	std	2	std
SiO2	44.8	1.05	43.8	0.77	44.2	1.00	43.7	0.70	43.9	1.08	43.6	2.26	42.5	0.60	43.3	0.84	42.4	1.88	43.5	0.25
TiO2	1.37	0.21	1.53	0.08	1.54	0.19	1.64	0.28	1.48	0.20	1.68	0.14	1.99	0.17	1.65	0.19	2.15	0.13	2.45	0.21
Al2O3	12.9	1.02	13.0	0.16	13.5	0.60	13.3	0.42	13.2	0.61	14.3	1.00	14.0	0.60	14.1	0.52	14.8	0.44	14.8	0.66
Cr2O3	0.85	0.11	0.87	0.02	0.80	0.08	0.78	0.18	0.81	0.10	0.44	0.05	0.29	0.04	0.52	0.08	0.95	0.04	0.79	0.08
FeO	5.21	0.24	5.41	0.20	5.80	0.20	6.24	0.08	5.73	0.10	6.53	0.26	7.24	0.53	6.31	0.24	6.44	0.10	7.41	0.06
MnO	0.05	0.03	0.05	0.02	0.05	0.03	0.06	0.06	0.08	0.04	0.08	0.05	0.07	0.05	0.06	0.03	0.10	0.04	0.04	-
NiO	0.03	0.04	0.04	0.03	0.04	0.04	0.05	0.03	0.03	0.02	0.02	0.01	0.01	0.01	0.01	0.03	0.08	0.01	0.01	0.01
MgO	17.0	0.83	16.1	0.17	16.7	0.41	16.2	0.63	16.2	0.85	16.4	0.82	14.8	0.60	15.6	0.22	15.8	0.07	15.4	0.20
CaO	12.5	0.30	12.5	0.17	12.6	0.09	12.3	0.16	12.2	0.21	12.2	0.15	12.0	0.21	12.1	0.11	12.1	0.08	11.8	0.11
Na2O	2.18	0.21	2.20	0.19	1.97	0.17	2.17	0.14	2.23	0.02	2.29	0.25	2.59	0.07	2.23	0.10	1.99	0.21	2.44	0.04
K2O	0.16	0.03	0.59	0.02	0.45	0.07	0.92	0.08	0.60	0.10	0.30	0.03	0.50	0.10	0.42	0.05	0.34	0.07	0.36	0.01
Total	97.1	0.92	96.0	0.44	97.6	0.48	97.3	0.70	96.4	1.69	97.9	0.81	95.9	1.83	96.4	0.93	97.2	1.75	98.9	0.35
Mg#	85.3	0.99	84.1	0.48	83.7	0.67	82.2	0.52	83.4	0.54	81.7	1.08	78.5	0.81	81.5	0.66	81.4	0.27	78.7	0.34

Table 3: Continued

Amphibole																
BC2A		MC24A		MC27/1 B		MC20/2		AC1B		MC4B		MC27A		MC7/4		
Pl-bearing Pyroxenite		Pl-bearing Pyroxenite		Hornblendite		Hbl-rich gabbro		Hbl-rich gabbro		Hbl-rich gabbro		Hornblende Gabbronorite		Hornblende Gabbronorite		
7	std	6	std	12	std	7	std	14	std	6	std	18	std	6	std	
43.0	0.56	42.2	1.31	43.4	0.35	42.2	0.63	42.4	0.72	40.6	0.53	42.3	0.79	42.0	0.47	
1.98	0.19	2.65	0.22	1.68	0.24	2.50	0.20	2.23	0.17	2.11	0.11	2.73	0.27	3.14	0.16	
15.3	0.46	15.4	0.63	15.4	0.42	15.6	0.47	15.2	0.38	15.1	0.31	14.6	0.60	13.7	0.40	
0.62	0.06	0.33	0.09	0.10	0.05	0.03	0.03	0.02	0.02	0.02	0.02	0.13	0.03	0.06	0.03	
6.12	0.26	7.80	0.19	6.38	0.28	8.68	0.07	8.71	0.38	8.15	0.10	9.44	0.67	11.5	0.14	
0.09	0.03	0.05	0.07	0.08	0.03	0.12	0.07	0.10	0.02	0.11	0.03	0.13	0.03	0.17	0.01	
0.02	0.03	0.03	0.03	0.03	0.03	0.05	0.04	0.03	0.02	0.01	0.02	0.02	0.02	0.03	0.04	
15.0	0.32	14.5	0.35	16.0	0.23	13.7	0.60	13.8	0.30	13.7	0.14	13.5	0.42	12.3	0.25	
12.0	0.14	11.9	0.13	12.5	0.07	11.2	0.12	11.3	0.11	11.6	0.10	11.4	0.12	11.3	0.27	
2.67	0.10	2.51	0.16	2.34	0.07	2.81	0.16	2.83	0.14	2.55	0.11	2.70	0.12	2.82	0.14	
0.15	0.03	0.57	0.07	0.31	0.04	0.49	0.02	0.50	0.04	0.41	0.01	0.47	0.04	0.45	0.02	
97.0	0.75	97.9	0.57	98.2	0.37	97.4	0.68	97.1	0.65	94.3	0.62	97.5	0.75	97.6	0.73	
81.4	0.81	76.9	0.57	81.7	0.74	73.7	0.83	73.8	1.11	74.9	0.41	71.9	1.97	65.5	0.65	

Table 3: Continued

	Spinel																	
Sample	AC1D		BC4A		MC27B		MC8/3		MC8/1		MC25A		BC5B		MC22A		MC20/1	
Rock Type	Dunite		Dunite		Dunite		Px-bearing Peridotite		Px-bearing Peridotite		Px-bearing Peridotite		Px-bearing Peridotite		Pl-free Pyroxenite		Pl-free Pyroxenite	
n.	7	std	3	std	4	std	8	std	3	std	2	std	4	std	3	std	2	std
SiO2	0.02	0.03	0.14	0.08	0.06	0.09	0.04	0.03	0.05	0.07	0.09	0.04	0.10	0.05	0.01	0.01	0.06	0.05
TiO2	0.10	0.08	0.08	0.08	0.18	0.06	0.09	0.05	0.23	0.06	0.06	0.08	0.06	0.06	0.05	0.04	0.07	0.06
Al2O3	46.0	2.00	47.0	2.05	39.9	1.76	48.4	1.04	44.6	1.40	45.8	4.04	55.1	2.25	58.1	2.16	52.6	2.47
Cr2O3	16.5	0.88	16.5	0.60	18.7	1.44	15.3	0.63	18.0	1.33	16.6	0.62	5.99	0.38	6.14	1.80	12.7	0.36
FeO	25.1	0.91	25.5	1.00	29.5	2.11	24.6	1.01	26.3	0.23	25.0	1.85	22.0	1.69	20.0	1.02	22.8	2.49
MnO	0.15	0.03	0.17	0.07	0.18	0.05	0.16	0.06	0.13	0.05	0.13	0.00	0.13	0.03	0.10	0.02	0.08	0.01
NiO	0.05	0.04	0.08	0.04	0.07	0.06	0.14	0.04	0.12	0.04	0.15	0.08	0.15	0.05	0.08	0.02	0.01	0.01
MgO	12.3	0.94	12.4	0.70	10.0	0.69	12.8	0.58	11.2	0.45	12.1	1.85	13.8	0.67	15.0	0.32	13.1	0.86
CaO	0.02	0.03	0.02	0.01	0.03	0.03	0.01	0.01	0.02	0.02	0.04	0.03	0.04	0.03	0.01	0.01	0.00	0.00
Na2O	0.06	0.06	0.12	0.05	0.09	0.08	0.02	0.03	0.17	0.08	0.07	0.00	0.13	0.11	0.02	0.01	0.09	0.01
K2O	0.02	0.02	0.03	0.03	0.00	0.01	0.00	0.00	0.03	0.03	0.01	0.02	0.02	0.01	0.00	0.00	0.01	0.02
Total	100	1.80	102	3.02	98.7	3.97	102	1.38	101	3.12	100	3.40	97.5	3.89	99.5	0.39	102	1.25
Mg#	51.8	2.50	51.8	1.54	44.4	2.44	48.1	1.79	48.0	0.37	51.4	4.81	57.7	1.45	57.2	1.77	53.3	2.36
Cr#	19.4	1.31	19.0	1.02	23.9	1.21	17.5	0.82	21.3	1.07	19.6	1.98	6.79	0.30	6.63	2.02	14.0	0.22

Table 3: Cotinued

	Plagioclase															
Sample	MC26A		BC2A		MC24A		MC20/2		AC1B		MC4B		MC27A		MC7/4	
Rock Type	Pl-bearing Pyroxenite		Pl-bearing Pyroxenite		Pl-bearing Pyroxenite		Hbl-rich gabbro		Hbl-rich gabbro		Hbl-rich gabbro		Hornblende Gabbronorite		Hornblende Gabbronorite	
n.	6	std	6	std	7	std	6	std	8	std	9	std	13	std	13	std
SiO2	45.1	1.26	45.0	0.57	45.5	1.21	45.9	0.99	46.4	0.59	44.5	0.67	48.4	1.17	51.3	0.96
TiO2	0.04	0.03	0.01	0.01	0.03	0.04	0.05	0.05	0.01	0.01	0.01	0.02	0.02	0.02	0.01	0.02
Al2O3	35.1	0.97	34.9	0.47	34.6	0.89	33.4	0.83	34.2	0.48	33.2	0.99	32.5	0.54	30.6	0.71
Cr2O3	0.01	0.02	0.03	0.02	0.00	0.01	0.02	0.02	0.01	0.01	0.01	0.02	0.01	0.01	0.01	0.01
FeO	0.23	0.04	0.04	0.03	0.12	0.08	0.10	0.07	0.03	0.03	0.03	0.03	0.06	0.04	0.04	0.03
MnO	0.03	0.04	0.01	0.02	0.03	0.02	0.02	0.03	0.01	0.01	0.01	0.01	0.01	0.01	0.01	0.02
NiO	0.03	0.03	0.01	0.02	0.02	0.03	0.03	0.03	0.02	0.03	0.02	0.02	0.02	0.02	0.01	0.02
MgO	0.07	0.09	0.01	0.01	0.04	0.04	0.02	0.02	0.01	0.01	0.01	0.01	0.01	0.01	0.02	0.02
CaO	18.4	0.79	18.1	0.35	17.9	0.65	17.5	0.28	17.0	0.57	18.5	0.34	15.4	0.67	13.2	0.57
Na2O	1.10	0.36	1.00	0.18	1.29	0.34	1.54	0.13	1.72	0.29	0.96	0.21	2.67	0.40	3.94	0.38
K2O	0.06	0.03	0.04	0.02	0.05	0.03	0.06	0.02	0.05	0.01	0.01	0.01	0.05	0.02	0.08	0.02
Total	100	0.77	99.1	0.54	99.7	1.11	98.6	1.43	99.4	0.50	97.3	1.39	99.2	0.88	99.3	0.66
An (mol%)	89.9	3.21	90.7	1.59	88.2	3.08	85.9	1.30	84.3	2.59	91.4	1.84	75.9	3.53	64.6	3.07

Table 3: Continued

Sample	AC1D	BC4A	MC27B	MC8/3	MC8/1	MC25A	BC5B	MC8B	MC22A	MC20/1	MC26A	BC2A	MC24A	MC27/1 B	MC20/2	AC1B	MC4B	MC27A	MC7/4
Rock Type	Dunite	Dunite	Dunite	-bearing Perido	-bearing Perido	-bearing Perido	-bearing Perido	l-free Pyroxeni	l-free Pyroxeni	l-free Pyroxeni	bearing Pyroxe	bearing Pyroxe	bearing Pyroxe	Hornblendite	Hbl-rich gabbro	Hbl-rich gabbro	Hbl-rich gabbro	blende Gabbro	blende Gabbro
Amp	1014 °C	979 °C	985 °C	967 °C	986 °C	984 °C	995 °C	1001 °C	990 °C	1009 °C	1009 °C	1017 °C	1021 °C	1005 °C	1014 °C	1005 °C	1012 °C	1004 °C	998 °C
Pl-Amp	-	-	-	-	-	-	-	-	-	-	979 °C	954 °C	964 °C	-	957 °C	937 °C	980 °C	905 °C	886 °C
Ca in Opx	-	-	-	-	-	803 °C	843 °C	866 °C	836 °C	-	-	-	-	-	-	-	-	-	-

Table 4: Temperature estimates based on: (i) the Ca-in-orthopyroxene geothermometer of Brey and Kohler (1990), (ii) the amphibole-plagioclase geothermometer of Holland and Blundy (2009), and (iii) the amphibole geothermometer of Putirka (2016, equation 6). A confining pressure of 11 kbar was assumed in the calculations, in agreement with pressure estimates obtained from granulite facies metasediments in the study area (Redler et al., 2012).

	Amphibole																			
Sample	BC4A		MC27B		MC8/3		MC8/1		MC25A		BC5B		MC8B		MC22A		MC20/1			
Rock Type	Dunite		Dunite		Px-bearing peridotite		Px-bearing peridotite		Px-bearing peridotite		Px-bearing peridotite		Plagioclase-free pyroxenite		Plagioclase-free pyroxenite		Plagioclase-free pyroxenite			
n.	7	std	6	std	4	std	13	std	13	std	7	std	16	std	4	std	13	std		
Sc	207	13.3	162	3.76	145	2.04	112	4.20	143	5.29	132	9.28	66.8	3.03	144	8.95	108	3.80		
Ti	8024	887	8672	329	9359	791	8153	631	8749	555	9586	517	12931	754	9742	1602	12442	615		
V	611	24.5	556	11.9	651	9.93	488	8.03	586	21.4	714	39.0	470	14.5	743	31.3	652	15.6		
Cr	5908	432	5396	220	5356	158	4851	153	5564	331	2798	212	2006	364	3501	217	6026	294		
Co	32	1.26	32.75	1.34	38	0.73	36.8	1.25	37.2	1.55	38.4	1.63	46.8	1.46	42.3	1.30	41.8	2.43		
Ni	160	7.08	194	3.26	332	4.91	291	6.91	277	13.66	231	11.5	185	8.89	128	7.68	199	16.5		
Zn	17.4	3.78	18.9	4.47	20.9	3.05	21.2	3.11	30.3	5.74	17.4	7.38	43.1	2.97	17.8	2.04	34.4	3.72		
Rb	4.10	1.22	19.7	7.23	13.0	0.56	32.7	4.78	21.8	1.97	7.05	0.77	3.73	0.36	9.94	1.18	4.42	0.59		
Sr	287	32.3	202	11.1	274	20.1	204	12.7	236	15.92	171	10.3	255	8.98	277	36.7	206	13.8		
Y	53.4	2.46	57.0	3.11	35.6	0.39	28.2	1.37	35.3	2.43	41.9	3.37	34.1	1.54	56.8	4.79	40.5	3.02		
Zr	66	3.81	109	3.37	74.5	1.94	93.8	7.65	118	7.92	37.9	2.58	65.2	2.43	83.7	4.76	36.7	1.24		
Nb	1.26	0.47	3.57	0.50	3.96	0.39	4.10	0.53	6.54	0.51	2.59	0.25	5.12	0.33	2.68	0.93	2.53	0.36		
Ba	77.9	13.5	115	24.6	189	13.6	173	54.1	229	32.35	120	13.2	125	6.61	141	25.8	93.3	14.8		
La	4.44	0.48	8.10	0.29	8.74	0.17	19.1	0.58	10.5	0.53	4.16	0.47	6.12	0.20	12.9	0.53	3.63	0.16		
Ce	15.2	0.76	22.6	0.67	20.7	0.14	44.4	1.22	24.9	1.32	11.2	0.94	17.0	0.49	31.7	0.95	10.9	0.54		
Pr	2.71	0.11	3.87	0.19	3.02	0.05	5.83	0.20	3.43	0.20	1.91	0.17	2.77	0.07	4.36	0.19	1.90	0.10		
Nd	16.5	0.71	22.6	1.39	15.4	0.44	26.3	1.37	17.6	1.27	11.8	0.91	15.4	0.38	21.4	1.02	11.5	0.54		
Sm	5.77	0.40	7.56	0.63	4.28	0.32	6.07	0.35	5.07	0.55	4.48	0.30	5.06	0.21	6.11	0.67	4.44	0.36		
Eu	2.20	0.17	2.55	0.14	1.68	0.18	1.59	0.11	1.60	0.14	1.72	0.17	1.75	0.07	1.89	0.14	1.60	0.08		
Gd	7.16	0.42	8.93	0.77	5.46	0.28	5.28	0.35	5.49	0.49	6.05	0.58	5.92	0.24	7.39	0.44	5.75	0.40		
Tb	1.34	0.06	1.55	0.14	0.97	0.05	0.88	0.06	0.98	0.08	1.13	0.08	1.04	0.06	1.44	0.04	1.05	0.09		
Dy	8.89	0.60	10.3	0.83	6.31	0.42	5.40	0.35	6.35	0.58	7.53	0.61	6.64	0.34	9.93	0.68	7.27	0.50		
Ho	2.06	0.14	2.26	0.16	1.43	0.06	1.13	0.09	1.34	0.12	1.71	0.11	1.38	0.08	2.26	0.12	1.61	0.12		
Er	6.26	0.29	6.18	0.28	4.07	0.17	3.05	0.22	3.86	0.22	4.66	0.26	3.67	0.29	6.52	0.54	4.55	0.47		
Tm	0.97	0.05	0.92	0.06	0.58	0.03	0.45	0.04	0.56	0.05	0.64	0.08	0.51	0.04	0.94	0.10	0.64	0.07		
Yb	7.45	0.51	6.47	0.08	4.29	0.35	3.09	0.24	4.00	0.32	4.43	0.46	3.37	0.22	6.49	0.74	4.32	0.38		
Lu	1.16	0.07	0.99	0.07	0.62	0.05	0.45	0.03	0.58	0.04	0.62	0.06	0.46	0.04	0.87	0.08	0.61	0.05		
Hf	2.39	0.26	3.25	0.16	2.19	0.21	2.29	0.25	3.33	0.27	1.52	0.20	2.20	0.14	2.82	0.47	1.33	0.09		
Ta	0.08	0.04	0.19	0.04	0.21	0.01	0.22	0.04	0.35	0.05	0.12	0.02	0.24	0.02	0.16	0.07	0.12	0.02		
Pb	1.72	0.28	3.09	0.21	4.07	0.44	8.29	0.81	3.52	0.42	2.21	0.19	2.61	0.20	3.71	0.64	1.54	0.10		
Th	0.09	0.04	0.90	0.06	0.99	0.07	3.04	0.37	1.18	0.16	0.41	0.13	0.68	0.06	2.09	0.38	0.35	0.03		
U	0.01	0.01	0.22	0.04	0.25	0.03	0.59	0.09	0.27	0.04	0.08	0.02	0.15	0.02	0.37	0.08	0.10	0.01		
Eu/Eu*	1.04		0.94		1.05		0.85		0.92		1.00		0.97		0.85		0.96			
La_N/Sm_N	0.49		0.68		1.30		2.01		1.33		0.59		0.77		1.34		0.52			
Gd_N/Yb_N	0.77		1.10		1.02		1.37		1.10		1.09		1.41		0.91		1.06			
Th/Nb	0.07		0.25		0.25		0.74		0.18		0.16		0.13		0.78		0.14			
Th/Y	0.00		0.02		0.03		0.11		0.03		0.01		0.02		0.04		0.01			
U/Ta	0.14		1.16		1.17		2.70		0.78		0.64		0.62		2.25		0.85			

Table 5: Trace element amphibole compositions.

	Amphibole																					
Sample	BC4A		MC27B		MC8/3		MC8/1		MC25A		BC5B		MC8B		MC22A		MC20/1					
Rock Type	Dunite		Dunite		Px-bearing peridotite		Px-bearing peridotite		Px-bearing peridotite		Px-bearing peridotite		Plagioclase-free pyroxenite		Plagioclase-free pyroxenite		Plagioclase-free pyroxenite					
n.	7	std	6	std	4	std	13	std	13	std	7	std	16	std	4	std	13	std				
Sc	207	13.3	162	3.76	145	2.04	112	4.20	143	5.29	132	9.28	66.8	3.03	144	8.95	108	3.80				
Ti	8024	887	8672	329	9359	791	8153	631	8749	555	9586	517	12931	754	9742	1602	12442	615				
V	611	24.5	556	11.9	651	9.93	488	8.03	586	21.4	714	39.0	470	14.5	743	31.3	652	15.6				
Cr	5908	432	5396	220	5356	158	4851	153	5564	331	2798	212	2006	364	3501	217	6026	294				
Co	32	1.26	32.75	1.34	38	0.73	36.8	1.25	37.2	1.55	38.4	1.63	46.8	1.46	42.3	1.30	41.8	2.43				
Ni	160	7.08	194	3.26	332	4.91	291	6.91	277	13.66	231	11.5	185	8.89	128	7.68	199	16.5				
Zn	17.4	3.78	18.9	4.47	20.9	3.05	21.2	3.11	30.3	5.74	17.4	7.38	43.1	2.97	17.8	2.04	34.4	3.72				
Rb	4.10	1.22	19.7	7.23	13.0	0.56	32.7	4.78	21.8	1.97	7.05	0.77	3.73	0.36	9.94	1.18	4.42	0.59				
Sr	287	32.3	202	11.1	274	20.1	204	12.7	236	15.92	171	10.3	255	8.98	277	36.7	206	13.8				
Y	53.4	2.46	57.0	3.11	35.6	0.39	28.2	1.37	35.3	2.43	41.9	3.37	34.1	1.54	56.8	4.79	40.5	3.02				
Zr	66	3.81	109	3.37	74.5	1.94	93.8	7.65	118	7.92	37.9	2.58	65.2	2.43	83.7	4.76	36.7	1.24				
Nb	1.26	0.47	3.57	0.50	3.96	0.39	4.10	0.53	6.54	0.51	2.59	0.25	5.12	0.33	2.68	0.93	2.53	0.36				
Ba	77.9	13.5	115	24.6	189	13.6	173	54.1	229	32.35	120	13.2	125	6.61	141	25.8	93.3	14.8				
La	4.44	0.48	8.10	0.29	8.74	0.17	19.1	0.58	10.5	0.53	4.16	0.47	6.12	0.20	12.9	0.53	3.63	0.16				
Ce	15.2	0.76	22.6	0.67	20.7	0.14	44.4	1.22	24.9	1.32	11.2	0.94	17.0	0.49	31.7	0.95	10.9	0.54				
Pr	2.71	0.11	3.87	0.19	3.02	0.05	5.83	0.20	3.43	0.20	1.91	0.17	2.77	0.07	4.36	0.19	1.90	0.10				
Nd	16.5	0.71	22.6	1.39	15.4	0.44	26.3	1.37	17.6	1.27	11.8	0.91	15.4	0.38	21.4	1.02	11.5	0.54				
Sm	5.77	0.40	7.56	0.63	4.28	0.32	6.07	0.35	5.07	0.55	4.48	0.30	5.06	0.21	6.11	0.67	4.44	0.36				
Eu	2.20	0.17	2.55	0.14	1.68	0.18	1.59	0.11	1.60	0.14	1.72	0.17	1.75	0.07	1.89	0.14	1.60	0.08				
Gd	7.16	0.42	8.93	0.77	5.46	0.28	5.28	0.35	5.49	0.49	6.05	0.58	5.92	0.24	7.39	0.44	5.75	0.40				
Tb	1.34	0.06	1.55	0.14	0.97	0.05	0.88	0.06	0.98	0.08	1.13	0.08	1.04	0.06	1.44	0.04	1.05	0.09				
Dy	8.89	0.60	10.3	0.83	6.31	0.42	5.40	0.35	6.35	0.58	7.53	0.61	6.64	0.34	9.93	0.68	7.27	0.50				
Ho	2.06	0.14	2.26	0.16	1.43	0.06	1.13	0.09	1.34	0.12	1.71	0.11	1.38	0.08	2.26	0.12	1.61	0.12				
Er	6.26	0.29	6.18	0.28	4.07	0.17	3.05	0.22	3.86	0.22	4.66	0.26	3.67	0.29	6.52	0.54	4.55	0.47				
Tm	0.97	0.05	0.92	0.06	0.58	0.03	0.45	0.04	0.56	0.05	0.64	0.08	0.51	0.04	0.94	0.10	0.64	0.07				
Yb	7.45	0.51	6.47	0.08	4.29	0.35	3.09	0.24	4.00	0.32	4.43	0.46	3.37	0.22	6.49	0.74	4.32	0.38				
Lu	1.16	0.07	0.99	0.07	0.62	0.05	0.45	0.03	0.58	0.04	0.62	0.06	0.46	0.04	0.87	0.08	0.61	0.05				
Hf	2.39	0.26	3.25	0.16	2.19	0.21	2.29	0.25	3.33	0.27	1.52	0.20	2.20	0.14	2.82	0.47	1.33	0.09				
Ta	0.08	0.04	0.19	0.04	0.21	0.01	0.22	0.04	0.35	0.05	0.12	0.02	0.24	0.02	0.16	0.07	0.12	0.02				
Pb	1.72	0.28	3.09	0.21	4.07	0.44	8.29	0.81	3.52	0.42	2.21	0.19	2.61	0.20	3.71	0.64	1.54	0.10				
Th	0.09	0.04	0.90	0.06	0.99	0.07	3.04	0.37	1.18	0.16	0.41	0.13	0.68	0.06	2.09	0.38	0.35	0.03				
U	0.01	0.01	0.22	0.04	0.25	0.03	0.59	0.09	0.27	0.04	0.08	0.02	0.15	0.02	0.37	0.08	0.10	0.01				
Eu/Eu*	1.04		0.94		1.05		0.85		0.92		1.00		0.97		0.85		0.96					
La_N/Sm_N	0.49		0.68		1.30		2.01		1.33		0.59		0.77		1.34		0.52					
Gd_N/Yb_N	0.77		1.10		1.02		1.37		1.10		1.09		1.41		0.91		1.06					
Th/Nb	0.07		0.25		0.25		0.74		0.18		0.16		0.13		0.78		0.14					
Th/Y	0.00		0.02		0.03		0.11		0.03		0.01		0.02		0.04		0.01					
U/Ta	0.14		1.16		1.17		2.70		0.78		0.64		0.62		2.25		0.85					

Table 5: Continued

	Clinopyroxene							
Sample	MC8B		MC20/1		BC2A		MC7/4	
Rock Type	Plagioclase-free pyroxenite		Plagioclase-free pyroxenite		Plagioclase-bearing pyroxenite		Hornblende gabbronorite	
n.	3	std	11	std	3	std	8	std
Sc	60.53	0.90	88.7	2.33	97.4	0.58	75.9	2.44
Ti	4810	112	4746	302	4633	50.7	4378	329
V	259	6	387	8.68	439	10.0	344	17.5
Cr	1133	116	3608	74.7	2641	38.3	217	14.8
Co	30.4	2.44	23.6	2.33	28.8	0.70	29.5	1.12
Ni	82.3	5.80	85.6	5.93	90.3	4.87	33.5	1.80
Zn	81.6	46.8	28.2	16.1	28.9	1.92	51.1	3.56
Sr	30.1	2.67	24.6	3.22	35.7	4.38	21.9	1.28
Y	15.8	0.53	17.9	1.82	21.4	0.70	18.9	1.58
Zr	53.8	1.02	33.8	1.07	42.2	0.43	76.8	3.43
Nb	0.07	0.05	0.03	0.01	0.01	-	0.04	0.01
La	2.39	0.12	1.59	0.24	2.39	0.12	1.38	0.16
Ce	7.43	0.38	5.24	0.67	7.42	0.26	5.99	0.51
Pr	1.27	0.07	0.99	0.14	1.27	0.04	1.20	0.11
Nd	7.49	0.27	6.15	0.83	7.41	0.92	7.60	0.53
Sm	2.57	0.20	2.22	0.37	2.34	0.39	2.91	0.39
Eu	0.77	0.06	0.76	0.13	0.84	0.16	0.91	0.14
Gd	2.87	0.02	2.81	0.36	3.33	0.22	3.24	0.36
Tb	0.52	0.02	0.52	0.08	0.61	0.02	0.58	0.03
Dy	3.23	0.12	3.52	0.41	4.09	0.07	3.97	0.36
Ho	0.67	0.02	0.77	0.07	0.84	0.09	0.78	0.06
Er	1.68	0.16	2.02	0.19	2.55	0.43	2.18	0.24
Tm	0.24	0.02	0.28	0.03	0.33	0.05	0.30	0.02
Yb	1.59	0.05	1.85	0.23	2.35	0.32	2.06	0.28
Lu	0.21	0.01	0.25	0.04	0.29	0.07	0.29	0.03
Hf	1.94	0.11	1.35	0.17	1.71	0.10	2.73	0.20
Ta	0.02	0.00	0.02	0.00	-	-	0.01	0.00
Pb	0.39	0.05	0.19	0.03	-	-	0.21	0.06
Eu/Eu*	0.86		0.92		0.91		0.90	
La_N/Sm_N	0.59		0.46		0.65		0.30	
Gd_N/Yb_N	1.44		1.22		1.13		1.26	

Table 6: Trace element clinopyroxene compositions.

Sample	AC1D	MC27B	MC8/3	MC8/1	MC8B	MC22A	MC26A	BC2A	MC27A	AC1B	MC4B
Rock Type	Dunite	Dunite	-bearing Perido	-bearing Perido	clase-free Pyro	clase-free Pyro	lase-bearing Py	lase-bearing Py	blende Gabbro	mblende rich ga	mblende rich ga
Whole Rock Analyses											
Rb (ppm)	0.13	0.34	0.19	0.89	3.51	0.58	0.77	0.61	7.30	4.33	2.72
Sr (ppm)	3.00	12.6	6.14	12.0	43.8	20.6	66.3	28.3	391	404	350
$^{87}Sr/^{86}Sr$	0.707369	0.70749	0.706987	0.708408	0.707059	0.70748	0.706646	0.707509	0.706404	0.707149	0.707087
2 s	0.000008	0.000008	0.00001	0.00001	0.000008	0.000008	0.000008	0.000008	0.000008	0.00001	0.000008
Sm (ppm)	0.05	0.14	0.13	0.25	2.28	0.52	0.41	0.71	3.17	3.22	3.47
Nd (ppm)	0.18	0.42	0.41	1.04	7.02	1.84	1.17	1.79	9.75	8.69	9.29
$^{143}Nd/^{144}Nd$	0.512523	0.512605	0.512516	0.512341	0.512506	0.512351	0.512558	0.5125	0.512626	0.512557	0.512565
2 s	0.000012	0.000008	0.000008	0.000008	0.000006	0.000006	0.000006	0.000008	0.000004	0.000006	0.000008
Age corrected Isotope ratios at 315 Ma (Whole Rock)											
$^{87}Sr/^{86}Sr$ (i)	0.706807	0.707139	0.706585	0.707442	0.706018	0.707115	0.706495	0.707229	0.706162	0.707010	0.706986
$^{143}Nd/^{144}Nd$ (i)	0.512145	0.512190	0.512130	0.512034	0.512098	0.511997	0.512116	0.512001	0.512217	0.512091	0.512096
ε_{Nd}	-1.70	-0.82	-2.00	-3.87	-2.63	-4.60	-2.28	-4.52	-0.29	-2.75	-2.67
Age corrected Isotope ratios at 290 Ma (Whole Rock)											
$^{87}Sr/^{86}Sr$ (i)	0.706852	0.707167	0.706617	0.707519	0.706101	0.707144	0.706507	0.707251	0.706181	0.707021	0.706994
$^{143}Nd/^{144}Nd$ (i)	0.512175	0.512223	0.512161	0.512058	0.512130	0.512025	0.512151	0.512041	0.512250	0.512128	0.512133
ε_{Nd}	-1.74	-0.81	-2.03	-4.02	-2.62	-4.68	-2.22	-4.37	-0.29	-2.66	-2.57
Age corrected Isotope ratios at 200 Ma (Whole Rock)											
$^{87}Sr/^{86}Sr$ (i)	0.707013	0.707267	0.706732	0.707795	0.706399	0.707248	0.706550	0.707331	0.706250	0.707061	0.707023
$^{143}Nd/^{144}Nd$ (i)	0.512283	0.512342	0.512271	0.512146	0.512247	0.512126	0.512277	0.512183	0.512367	0.512261	0.512267
ε_{Nd}	-1.90	-0.76	-2.14	-4.57	-2.61	-4.97	-2.02	-3.85	-0.27	-2.32	-2.21
Amphibole Analyses											
Rb (ppm)	-	-	-	-	3.74	5.93	6.77	-	5.37	6.44	2.88
Sr (ppm)	-	-	-	-	230	250	167	-	192	203	183
$^{87}Sr/^{86}Sr$	-	-	-	-	0.707054	0.707279	0.706989	-	0.706448	0.707342	0.707028
2 s	-	-	-	-	0.000010	0.000008	0.000010	-	0.000010	0.000008	0.000010
Sm (ppm)	-	-	-	-	4.93	4.96	4.00	-	4.75	4.14	4.16
Nd (ppm)	-	-	-	-	15.1	17.4	11.8	-	15.9	11.4	11.0
$^{143}Nd/^{144}Nd$	-	-	-	-	0.512512	0.512359	0.512506	-	0.512617	0.512543	0.512571
2 s	-	-	-	-	0.000006	0.000008	0.000008	-	0.000006	0.000006	0.000004
Age corrected Isotope ratios at 315 Ma (Amphibole)											
$^{87}Sr/^{86}Sr$ (i)	-	-		-	0.706843	0.706972	0.706463	-	0.706085	0.706931	0.706823
$^{143}Nd/^{144}Nd$ (i)	-	-		-	0.512102	0.512001	0.512080	-	0.512242	0.512087	0.512096
ε_{Nd}	-	-		-	-2.55	-4.52	-2.97	-	0.18	-2.84	-2.67
Age corrected Isotope ratios at 290 Ma (Amphibole)											
$^{87}Sr/^{86}Sr$ (i)	-	-	-	-	0.706860	0.706996	0.706505	-	0.706114	0.706963	0.706840
$^{143}Nd/^{144}Nd$ (i)	-	-	-	-	0.512134	0.512029	0.512114	-	0.512271	0.512123	0.512134
ε_{Nd}	-	-	-	-	-2.54	-4.59	-2.94	-	0.13	-2.77	-2.56
Age corrected Isotope ratios at 200 Ma (Amphibole)											
$^{87}Sr/^{86}Sr$ (i)	-	-	-	-	0.706920	0.707084	0.706655	-	0.706218	0.707081	0.706898
$^{143}Nd/^{144}Nd$ (i)	-	-	-	-	0.512252	0.512132	0.512236	-	0.512379	0.512253	0.512269
ε_{Nd}	-	-	-	-	-2.52	-4.86	-2.83	-	-0.04	-2.48	-2.17

Table 7: Nd and Sr isotopic ratios, and Sm-Nd isotopic and Rb-Sr dilution data of selected whole rocks and amphiboles.

Sample	BC4A	MC27B	MC8/3	MC8/1	MC25A	BC5B	MC8B	MC22A	MC20/1	MC26A	BC2A	MC24A	MC27/1 B	MC20/2	AC1B	MC4B	MC27A	MC7/4
Rock Type	Dunite	Dunite	-bearing Perido	-bearing Perido	-bearing Perido	-bearing Perido	l-free Pyroxeni	l-free Pyroxeni	l-free Pyroxeni	bearing Pyroxe	bearing Pyroxe	bearing Pyroxe	Hornblendite	nblende rich ga	blende rich ga	blende rich ga	blende Gabbro	blende Gabbron
La	0.24	0.21	0.26	0.17	0.19	0.20	0.19	0.22	0.23	0.21	0.22	0.20	0.20	0.18	0.18	0.20	0.22	0.21
Ce	0.40	0.36	0.45	0.29	0.33	0.34	0.32	0.37	0.40	0.36	0.36	0.33	0.34	0.31	0.30	0.33	0.37	0.36
Pr	0.63	0.55	0.71	0.45	0.51	0.53	0.49	0.58	0.63	0.56	0.55	0.51	0.53	0.48	0.47	0.51	0.57	0.57
Nd	0.90	0.77	1.02	0.64	0.72	0.77	0.70	0.83	0.91	0.81	0.78	0.73	0.76	0.68	0.67	0.73	0.81	0.82
Sm	1.40	1.16	1.59	0.99	1.11	1.21	1.05	1.27	1.42	1.26	1.17	1.11	1.18	1.05	1.02	1.11	1.25	1.28
Eu	1.56	1.28	1.79	1.10	1.24	1.36	1.17	1.41	1.60	1.41	1.29	1.24	1.32	1.17	1.14	1.24	1.39	1.44
Gd	1.67	1.36	1.91	1.17	1.32	1.46	1.24	1.51	1.72	1.52	1.36	1.32	1.41	1.25	1.22	1.32	1.48	1.55
Tb	1.71	1.37	1.96	1.20	1.34	1.51	1.26	1.54	1.77	1.56	1.38	1.35	1.45	1.28	1.25	1.35	1.51	1.60
Dy	1.67	1.33	1.92	1.17	1.31	1.49	1.22	1.51	1.76	1.54	1.35	1.32	1.42	1.25	1.22	1.32	1.48	1.58
Y	1.62	1.28	1.86	1.13	1.26	1.45	1.18	1.46	1.71	1.50	1.30	1.28	1.38	1.21	1.18	1.27	1.43	1.54
Ho	1.58	1.24	1.82	1.10	1.24	1.42	1.15	1.42	1.68	1.47	1.27	1.25	1.35	1.19	1.16	1.24	1.40	1.51
Er	1.45	1.14	1.67	1.01	1.14	1.32	1.06	1.31	1.56	1.36	1.16	1.15	1.25	1.10	1.07	1.15	1.29	1.40
Tm	1.32	1.02	1.51	0.92	1.03	1.21	0.95	1.19	1.42	1.24	1.05	1.05	1.13	1.00	0.97	1.04	1.17	1.28
Yb	1.18	0.91	1.36	0.82	0.92	1.09	0.85	1.06	1.29	1.12	0.94	0.94	1.02	0.90	0.87	0.93	1.05	1.15
Lu	1.05	0.81	1.21	0.73	0.82	0.98	0.76	0.95	1.16	1.01	0.84	0.84	0.92	0.80	0.78	0.84	0.94	1.04
Temperature estimates																		
T °C	979	985	967	986	984	995	1001	990	1009	1009	1017	1021	1005	1014	1005	1012	1004	998

Table 8: Amphibole/melt REE partition coefficients calculated based on amphibole major element compositions and crystallization temperature conditions, following the method of SHIMIZU ET AL. (2017). For the crystallization temperatures, we assumed those calculated following PUTIRKA (2016).

Reactive melt migration controls the trace element budget of the lower oceanic crust: insights from the troctolite-olivine gabbro association of the Pineto ophiolite (Corsica, France)

Tables of Contents

1. Introduction

Mid-ocean ridge basalts (MORB), the most common volcanic rocks on earth, from through the decompression of the astenospheric mantle and, due to buoyant forces and compact driven stresses, start to migrate upwards fractionating in multiple magma chambers. The products of these processes are a variety of gabbroic rocks that form the lower oceanic crust. Since MORB magmas form directly by decompression melting and don't traverse old and thick crust, the interactions with host rocks are limited and their compositions reflect directly the compositions of the mantle sources, assuming that the crustal evolution is essentially controlled by fractional crystallization (e.g. Klein & Langmuir, 1987). Fractional crystallization was considered for decades the main-driving force behind the crustal evolution of the lower oceanic crust (e.g. Grove et al., 1992). However, numerous studies in the last years have provided evidences that this crustal evolution is an extremely complex process that involves more than the fractional crystallization alone (Meyer et al., 1989; Coogan et al., 2000; Dick et al., 2002; Gao et al., 2007; Lissenberg et al., 2013; Sanfilippo et al., 2015a). In particular, evidence in gabbros indicate that melts can migrate through the forming crystal mushes, partly assimilating the crystal matrix, and crystallizing new minerals (e.g.: Lissenberg and MacLeod, 2017). The chemical consequence of these processes can be investigated using the variability of the mineral phases involved in the reaction.

The present study provides new geochemical insights about the troctolites and gabbros exposed in the ophiolitic section of the Pineto gabbroic sequence (central Corsica, France). Based on microstructural evidence and geochemical compositions of olivine it was previously suggested that the lithological transition from troctolite to olivine gabbro is the consequence of melt-rock reaction processes where a melt saturated in Cpx assimilates the olivine-plagioclase matrix, crystallizing new Cpx (Sanfilippo and Tribuzio 2013; Sanfilippo et al., 2015b). Here, we now focus on the plagioclase and on the whole rock compositions of a subset of sampled previously characterized.

2. Geology of the Pineto ophiolite

The Pineto ophiolite is located near the tectonic lineament separating the Alpine tectonic stack from Corsica (Alpine Corsica) from the Upper Carboniferous-Lower Permian continental basement (e.g., Rossi et al., 1994; Renna et al., 2007). This ophiolite is situated at the top of the Alpine Corsica and it is essentially unaffected by the Alpine metamorphism. Previous structural and geochemical studies of the Pineto ophiolite (Beccaluva et al., 1977; Saccani et al., 2000; Sanfilippo and Tribuzio, 2013) document that it exposes a lower crustal section similar to those forming the gabbroic oceanic core complexes from Mid-Atlantic and the Southwest Indian Ridges (e.g., Dick et al., 2000; Ildefonse et al., 2007; Smith et al., 2014).

The Pineto lower crust covers an area ~10 km2 (Fig. 1), into two main sectors displaying different bulk compositions (Sanfilippo and Tribuzio, 2013). The northern sector (~500 m thick) mostly consists of clinopyroxene-rich gabbros to gabbronorites, displaying a weak grain-size layering and in places crosscut by basalts dykes and amphibole veins. These gabbros also contain a troctolite body, which in turn locally includes up to m-scale thick, olivine-rich (>70 vol%) troctolite intercalations. The gabbros retain primary contacts with a basalt-sedimentary cover that is few meters in thickness. This cover comprises Middle-Upper Jurassic radiolarian cherts and Cretaceous shaly pelagites (Durand-Delga et al., 2005). Between the gabbros and the sedimentary cover, Sanfilippo and Tribuzio (2013) documented polygenic breccias containing angular gabbro and minor basalt clasts. A discontinuous cover of N-MORB pillowed basalts (Saccani et al., 2008) also characterizes the contact between the gabbros and the sedimentary cover. The gabbros were therefore exhumed to the seafloor during the Middle-Upper Jurassic. Close to the contact with the basalt-sedimentary cover, the gabbros show rare centimeter-scale shear zones characterized by porphyroclastic to mylonitic fabrics.

The southern sector of the Pineto ophiolite exposes a lower crustal sequence mainly made up of troctolites, with minor olivine-gabbro and sparse olivine-rich troctolite intercalations. The physical continuity with the gabbros from the northern sector and the geometry of the magmatic layering allowed Sanfilippo and Tribuzio (2013) to infer that this sector represents a stratigraphically lower portion of the crustal sequence. On the basis of the geometry of the grain size layering, which is locally accompanied by slight changes in modal composition, Sanfilippo and Tribuzio (2013) estimated a thickness of ~1 km for this troctolite/olivine gabbro association. The olivine-gabbros form discrete layers (tens of meters in thickness) within the troctolites, constituting ~20 vol% of the association (see also Sanfilippo et al., 2015). Irregular clinopyroxene-rich veins locally occur within the troctolites near the olivine-gabbros. It was argued that the troctolites including

the clinopyroxene veins represent the lithological transition from troctolite to olivine-gabbros. The olivine-rich troctolite intercalations (up to m-scale thick) are mostly located towards the base of the troctolite/olivine-gabbro sequence.

The contact between the southern and the northern lower crust sequences is characterized by up to 50 m thick serpentinized peridotite slivers, interpreted as mantle portions entrapped during pluton growth (Sanfilippo and Tribuzio, 2013). The serpentinite protoliths consist of spinel-plagioclase-bearing clinopyroxene-poor lherzolites to harzburgites with porphyroclastic structure. The occurrence of variably evolved gabbros randomly distributed at different stratigraphic heights (Fig. 1) and the Ca-in olivine cooling rate estimates (-2.2 to -1.7 ºC/year log units) led Sanfilippo and Tribuzio (2013) to propose an accretion process ruled by multiple intrusions within a relatively cold mantle lithosphere.

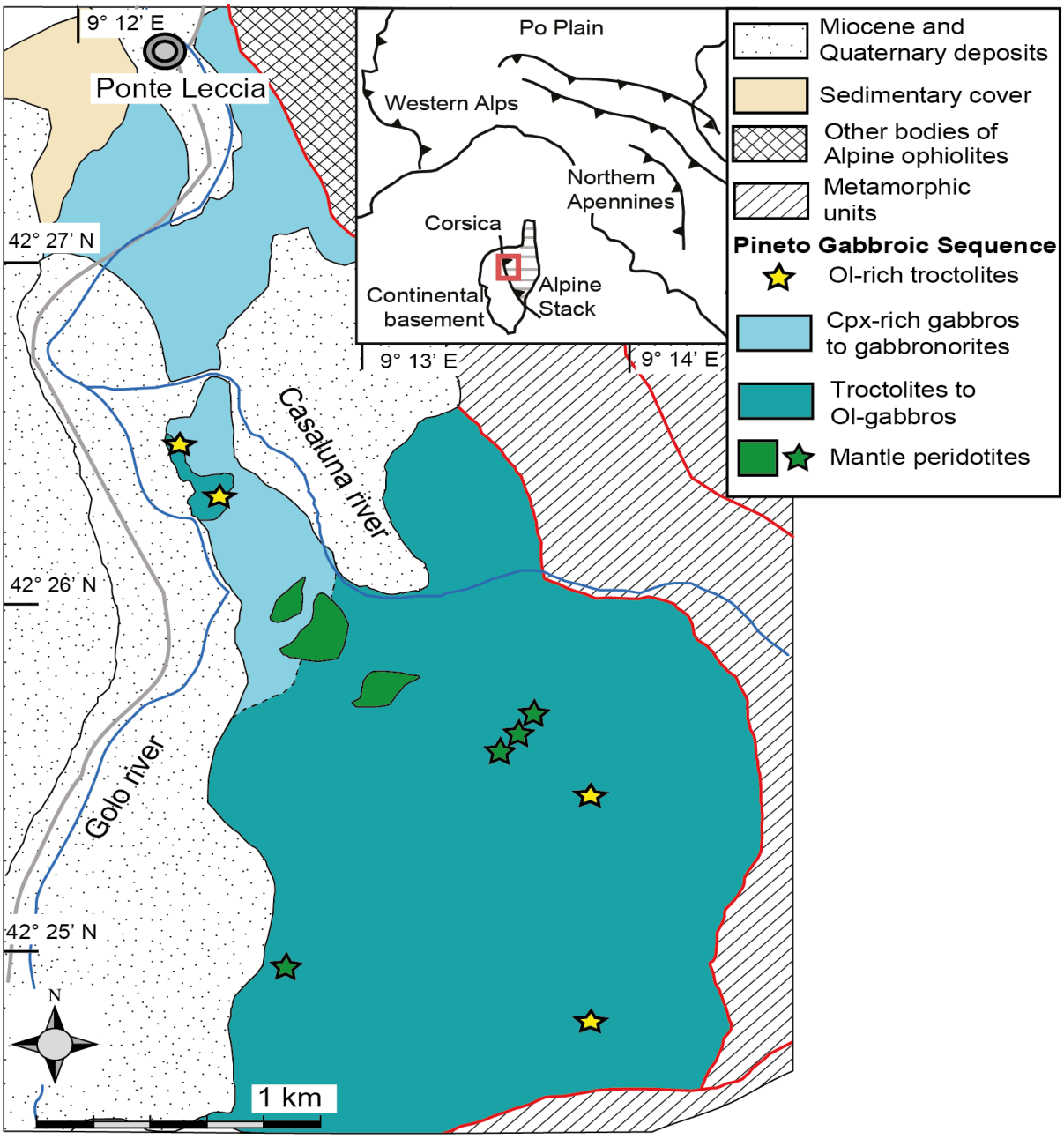

Figure 1: Simplified geological map of the Pineto gabbroic sequence (modified after SANFILIPPO AND TRIBUZIO, 2013).

3. Analytical methods

This study includes major and trace element whole-rock and mineral analyses of three olivine-rich troctolites, seven troctolites, two clinopyroxene-rich troctolites and three olivine-gabbros from the Pineto gabbroic sequence. Sample locations, main micro-structural characteristics and major element whole-rock and mineral compositions are reported in Sanfilippo and Tribuzio (2013). New major element mineral compositions were obtained for two samples and were achieved using a JEOL JXA-8200 electron microprobe located at Dipartimento di Scienze della Terra, Università degli Studi di Milano (Italy). Conditions of analyses were 15 kV accelerating voltage and 15 nA beam current; counting time were 30 s on the peak and 10 s on the background.

Whole rock trace element determinations were carried out by inductively coupled plasma atomic emission spectroscopy at Activation laboratories (Ancaster, Ontario). The samples were melted through a lithium metaborate/tetraborate fusion and then analyzed with ICP-MS. This method was used to determine major and some trace element (Sc, Ti, V, Cr, Co, Ni, Cu, Zn, Rb, Sr, Y, Zr, Nb, Cs, Ba, Rare Earth Elements, Hf, Ta, Pb, Th, U and W) concentrations. Detection limits are estimated to be 0.01% for most major and trace elements. Further details of the analytical technique are available on the company website (www.actlabs.com).

Trace element determinations of clinopyroxene and plagioclase cores were measured using a laser ablation inductively coupled plasma mass spectroscopy (ICPMS) at C.N.R., Istituto di Geoscienze e Georisorse (Unità di Pavia). This instrument couples a YAG laser operating at 266mm with a quadrupole ICPMS (DRc-e, PerkinElmer). Analyses were carried out with a spot of 30 μm. Data reduction was performed with the "Glitter" software package (Van Acterbergh et al., 2001). NIST SRM 612 was used as external standard while BRC2-g as reference glass for the accuracy testing. Olivine trace element compositions of ten samples (Sanfilippo et al. 2014; 2015) are also considered in this study.

4. Main petrological characteristics and whole-rock compositions

Modal compositions of selected rock samples are reported in Table 1. The reported stratigraphic heights and the locations of the samples are taken from Sanfilippo & Tribuzio (2013). The mineral modes are estimated on the basis of whole rock and mineral compositions using MODAN software (from Pactunk, 1997) with the following mineral densities: Ol=3.32, Pl=2.68-2.72, Cpx=3.40-3.30, Opx=3.20 and Ilm=4.72.

4.1 Olivine-rich troctolites

The olivine-rich troctolites show poikilitic texture, characterized by fine to medium grained (<100-500 nm) polygonal olivine (Fo_{89-88}), typically included in plagioclase (An_{72-68}) and clinopyroxene oikocrysts. The latter have Mg# [molar Mg/(Mg+Fe)] ranging from 89 to 90. Spinel (Cr# = 52-55 and TiO2 ~1.9 wt%) occurs as accessory phase, mostly included in clinopyroxene and plagioclase. Ti-rich amphibole and/or phlogopite are locally found within the spinel.

These rocks have high Mg# (~88), Ni (1200-1700 ppm) and Co (100-110 ppm). Cr concentrations range from 640 to 3320 ppm, most likely in relation to different spinel modal amounts (Fig. 2). The contents of Al_2O_3, CaO, Na_2O and TiO_2 are low (3-6 wt%, ~2 wt%, 0.2-0.4 wt%, and 0.03-0.08 wt%, respectively). The olivine-rich troctolites have also low concentrations of incompatible trace elements (e.g., Y = 0.7-1.3 ppm and Zr ~3 ppm). The concentrations of incompatible trace elements normalized to primitive mantle (PM, from Sun & McDonough, 1995) yield nearly flat patterns at ~0.2 times PM (Fig. 3). The patterns indeed display small positive Sr and Eu anomalies, and a slight enrichment of LREE with respect to MREE and HREE.

4.2 Troctolites

The troctolites are mainly made up of euhedral to subhedral plagioclase (An_{73-65}) and olivine (Fo_{88-84}). The clinopyroxene is present as films (Mg# = 86-90) around olivine or as small interstitial grains locally interconnected to form oikocrysts (Mg# = 88). Most troctolites contain orthopyroxene, which occurs as films or interstitial grains, typically associated with clinopyroxene, Ti-rich amphibole and/or ilmenite. Accessory spinel (Cr# = 50-66 and TiO_2 = 0.7-2.8 wt%) is also locally present.

The troctolites have Mg# ranging from 88 to 83, and higher Al_2O_3 (20-22 wt%), CaO (10-11 wt%) and NaO_2 (1.81-2.68 wt%) than the olivine-rich troctolites. The troctolite whole-rock compositions document a rough positive correlation between Mg# and compatible trace elements (e.g., Ni and Co), whereas moderately incompatible (Sc, V, Cu) and incompatible trace elements

(e.g., Y and Zr) are negatively correlated with Mg# (Fig. 2). Cr concentrations range from 110 to 500 ppm and do not correlate with Mg#. The troctolites have PM normalized patterns overall similar to those of the olivine-rich troctolites, although the former typically have higher absolute concentrations (up to 0.5 times PM, Fig. 4). The troctolites show positive Sr-Eu anomalies, which decrease with increasing REE and Y contents (Fig. 5); the LREE fractionation is variable, with CeN/YN ranging from 0.9 to 4.5.

4.3 Olivine-gabbros

The olivine-gabbros have a poikilitic texture with euhedral to subhedral olivine (Fo_{81-84}) and plagioclase (An_{65-63}) locally included within clinopyroxene oikocrysts (Mg# = 86-87). Orthopyroxene films and small orthopyroxene anhedral grains are also locally present, in places associated with Ti-rich amphibole and ilmenite.

The olivine-gabbros have relatively low Mg# (82-84). They show lower Al_2O_3 (16-18 wt%) and higher CaO (~14 wt%), Na_2O (2.18-2.54 wt%) and TiO_2 (0.21-0.26 wt%) than the troctolites. The olivine gabbros are also distinct in the high concentrations of Sc (27-37 ppm), V (96-118 ppm), Y (5.4-6.9 ppm) and REE. Although Ni in the olivine-gabbros is lower than in the troctolites, the former are enriched in Cr, with concentrations variable from 840 to 1690 ppm. The C1 (Lyubetskaya & Korenaga, 2007) normalized incompatible trace element patterns of the olivine-gabbros are characterized by depletion of LREE with respect to MREE and HREE (Ce_N/Y_N = 0.4-0.8), and small positive Sr-Eu anomalies (Fig. 6). The absolute REE concentrations of the olivine-gabbros are higher than in the troctolites.

	Sample Initial	Mineral modes (vol%)				Avarage Grain size (mm)				Accessory Spinel	Location	Estimated Stratigraphic height (m)
		Pl	Ol	Cpx	Opx	Pl	Ol	Cpx	Opx			
Ol-rich Trocolites	PI41a#	15	82	3	-	Oikocryst up to 10	Rounded to polygonal 0.3	Films up to 0.2	-	§	42°26' 21.51"N 9°12'28.09"E	1300
	PI85#	23	76	1	-	Oikocryst up to 5	Rounded to polygonal 0.5	Interstitial up to 1	-	§	42°24' 47.57"N 9°13'58.27"E	150
	PI80	20	79	1	-	-	-	-	-	§	-	-
Troctolites	PI44#	74	20	6	§	4.0	2.5	Discrete grain up to 1	Discrete grain up to 1	§	42°26' 21.51"N 9°12'28.09"E	1350
	PI62#	72	20	8	§	2.0	1.5	Oikocryst up to 15	Films up to 0.2	-	42°26' 15.61"N 9°13'27.14"E	1000
	PI56	70	25	5	§	3.0	2.0	Discrete grain up to 1	Films up to 0.2	§	42°26' 08.78"N 9°13'35.02"E	900
	PI31#	76	17	7	§	1.5	1.0	Films up to 0.1	Films up to 0.1	§	42°26' 03.67"N 9°13'25.20"E	850
	PI54#	74	22	4	§	7.0	4.0	Discrete grain up to 1	Films up to 0.3	§	42°25' 41.81"N 9°13'44.36"E	600
	PI33#	73	22	5	§	3.0	2.0	Films up to 0.2	Films up to 0.2	§	42°25' 12.37"N 9°13'54.48"E	450
	PI49#	74	20	6	-	0.7	0.2	Oikocryst up to 5	-	§	42°25' 02.08"N 9°13'53.47"E	250
	PI19#	68	22	10	§	3.5	2.5	Oikocryst up to 25	-	§	42°24' 46.08"N 9°13'59.61"E	125
	PI16#	75	24	1	-	1.5	0.7	Films up to 0.1	-	§	42°24' 44.14"N 9°13'57.58"E	120
Olivine gabbros	PI32#	63	10	27	§	4.0	2.0	Oikocryst up to 30	Films up to 0.3	-	42°26' 03.67"N 9°13'25.20"E	850
	PI34#	64	13	23	§	7.0	2.0	Oikocryst up to 30	Discrete grain up to 1	-	42°25' 00.57"N 9°13'27.98"E	400
	PI18#	60	10	31	-	2.5	1.0	Oikocryst up to 15	Films up to 0.1	-	42°24' 46.08"N 9°13'59.61"E	130

Table 1: Locations and petrography of the studied samples. Mineral modes are visually estimated (vol%). Coordinates are in WSGS. Classification and nomenclature after Streckeisen (1967). Symbology and mineral abbreviations: §<3%; -, mineral not present; Ol = Olivine; Opx = Orthopyroxene; Cpx = Clinopyroxene; Amp = Amphibole. The stratigraphic distances from the base of the sequence are given in metres and were evaluated on the basis of the average orientation of the grain-size/modal layering.

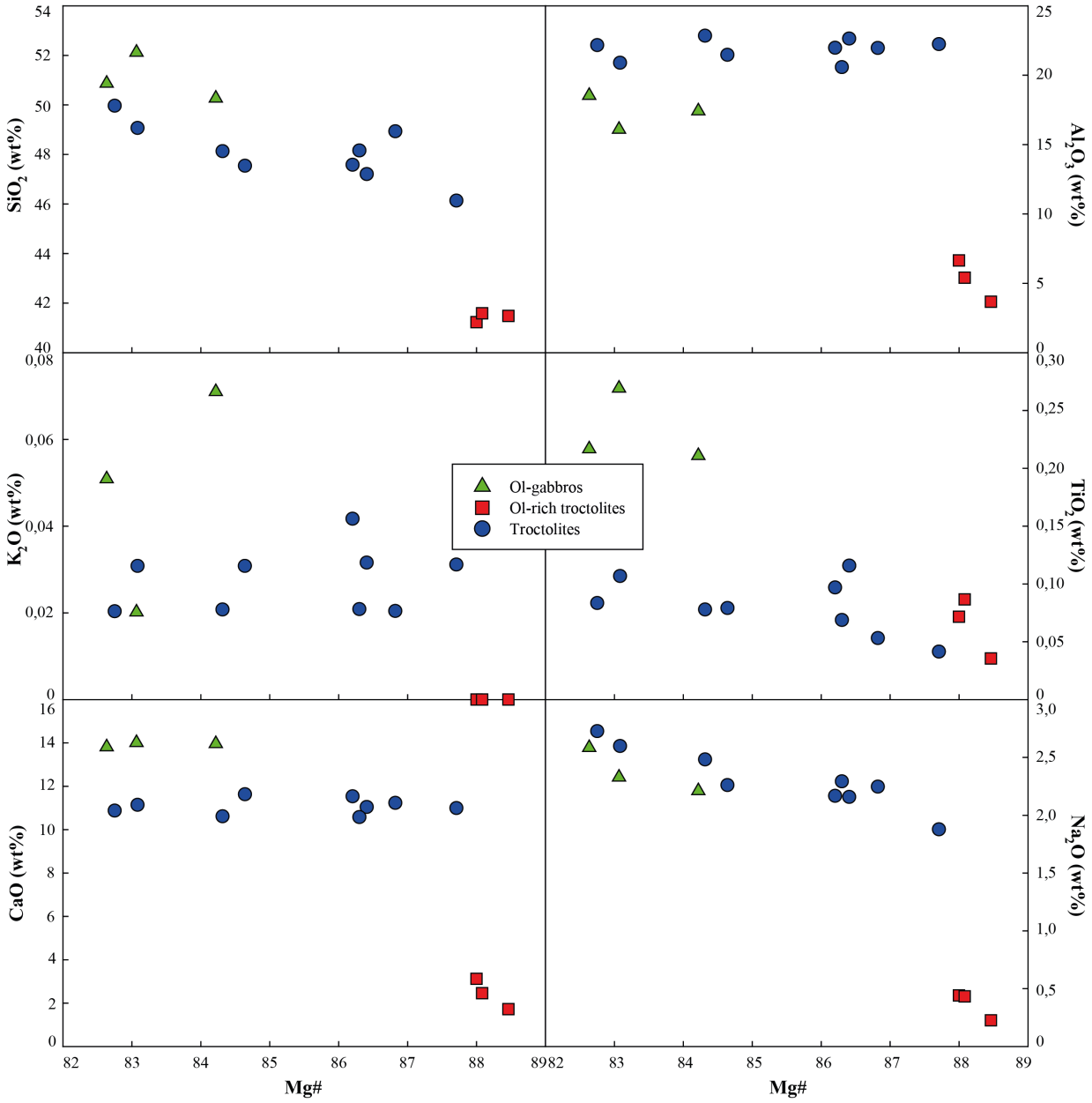

Figure 2: Whole rock diagrams showing the compositional variations of the major elements (CaO, SiO_2, Al_2O_3, K_2O, Na_2O and TiO_2 vs. Mg# [molar Mg/(Mg+Fe^{2+}tot) × 100]) between the various rock types.

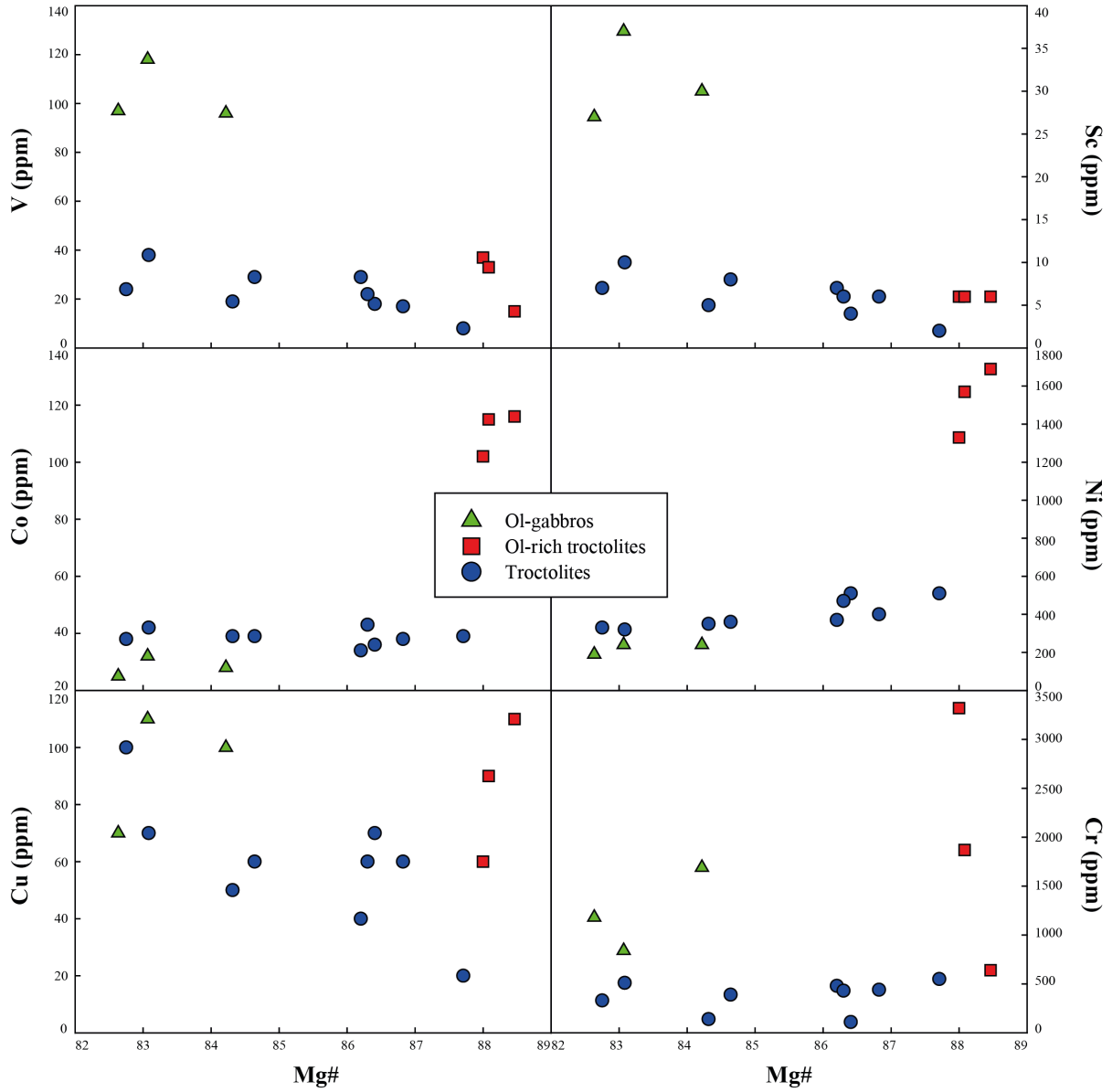

Figure 3: Whole rock diagrams showing the compositional variations of the trace elements (V, Sc, Co, Ni, Cu and Cr vs. Mg# [molar Mg/(Mg+Fe²+tot) × 100]) between the various rock types.

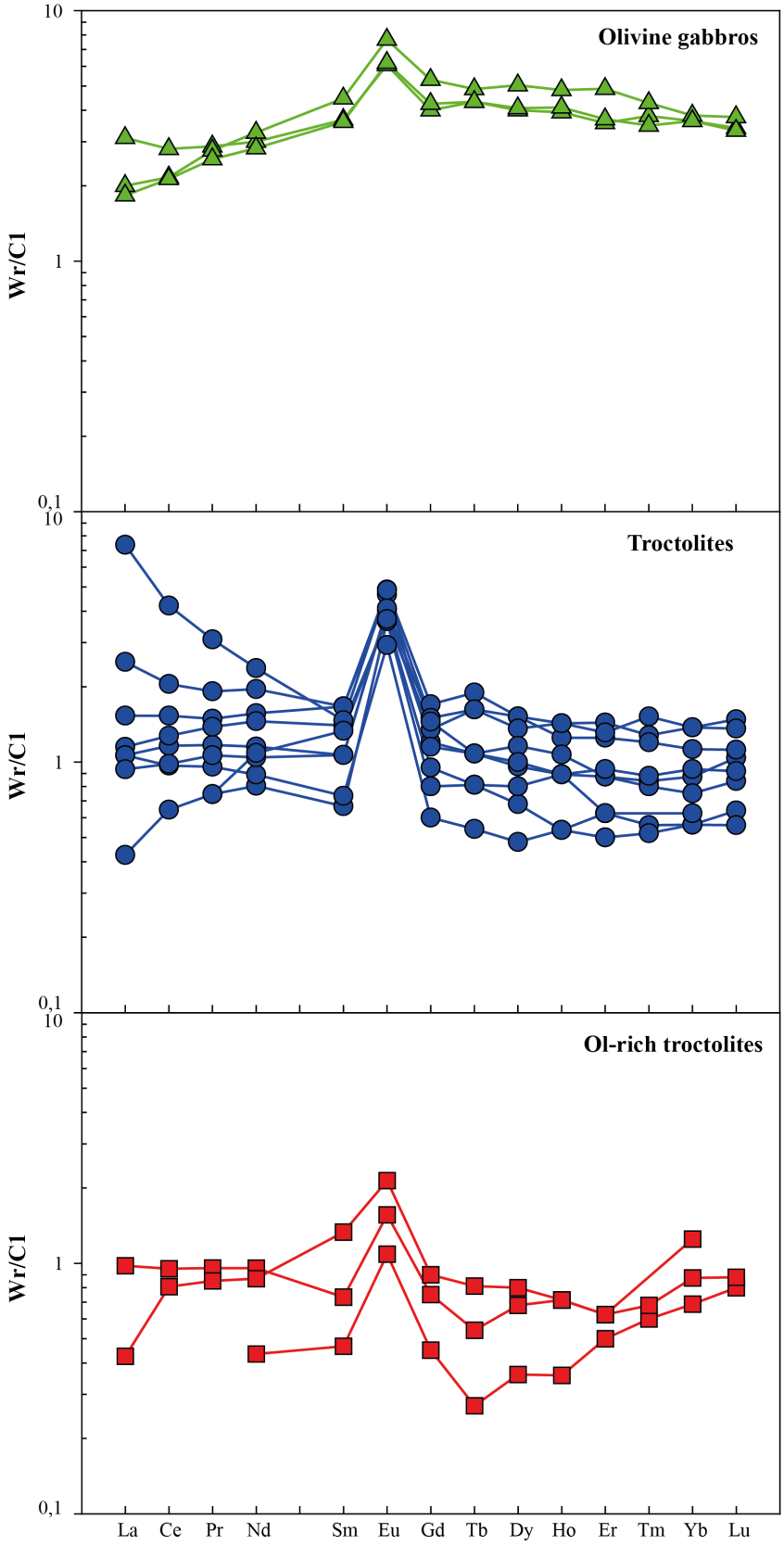

Figure 4: REE patterns for whole rocks normalised to C1 chondrite (Lyubetskaya & Korenaga, 2007).

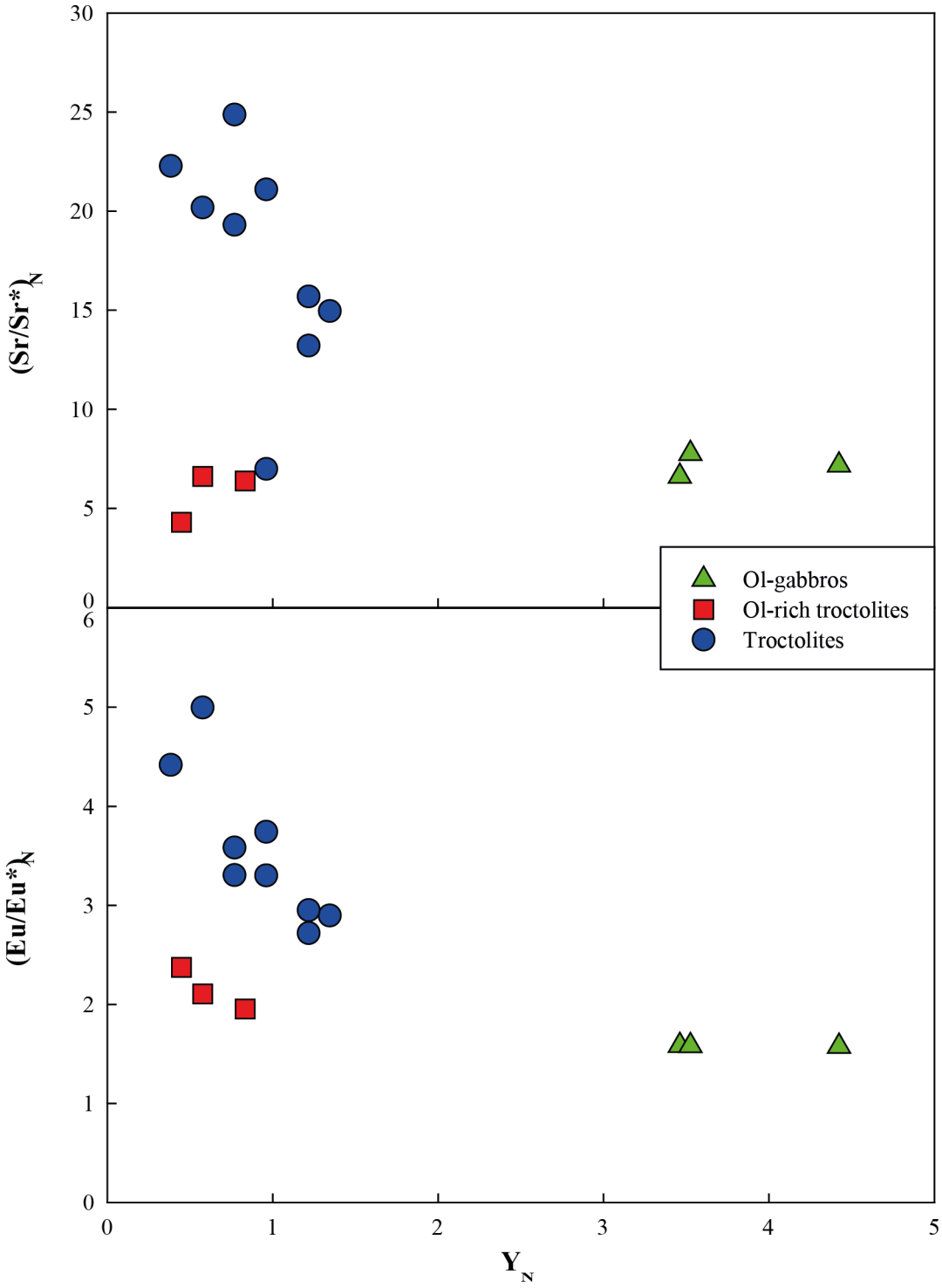

Figure 5: Plot of (Sr/Sr*) and (Eu/Eu*) vs. Y for whole rocks normalised to C1 chondrite (Lyubetskaya & Korenaga, 2007).

5. Minor and trace element compositions of minerals

5.1 Olivine

Minor and trace element compositions of olivine are reported in previous studies (Sanfilippo et al., 2014; 2015) and will be hereafter summarized. Olivine shows gradual variations in forsterite component and Ni (1900 to 1350 ppm) contents, which gradually decrease from the olivine-rich troctolites to the troctolites and the olivine-gabbros. Mn (1900-1350 ppm) and Co (1900-1350 ppm) are negatively correlated with forsterite molar proportions and Ni. The incompatible trace elements (Ti, Y, HREE and Zr) in olivine from the olivine-rich troctolites and the troctolites display positive correlation with Mn. Olivine from the olivine-gabbros is characterized by a relative depletion in incompatible elements, which at given Mn contents are lower than those in the troctolites.

5.2 Plagioclase

The chondrite-normalized pattern of plagioclase invariably displays slight enrichment in LREE with respect to Y (La_N/Y_N=1.8-6.0), positive Sr-Eu anomalies, and slight Ba depletion with respect to La (Fig. 7). The highest and the lowest LREE enrichment was typically observed for plagioclase from the olivine-rich troctolites and the troctolites, respectively. Plagioclase from the olivine-gabbros overall has slightly lower Y than plagioclase from the olivine-rich troctolites and the troctolites.

5.3 Clinopyroxene

The cores of clinopyroxene oikocrysts from the different rock-types have high Cr contents (2013-8630 ppm) and low incompatible trace element concentrations (Table 4). Their chondrite-normalized patterns display LREE depletion with respect to MREE and HREE (La_N/Sm_N = 0.04-0.11, Gd_N/Yb_N = 0.8-1.2). The small interstitial clinopyroxenes have REE patterns overall parallel to those of oikocrystic clinopyroxenes (Fig. 8), but at higher absolute concentrations. The small clinopyroxenes are also distinct in the Eu and Sr depletions relative to adjacent elements (Fig. 9), and in the absence of negative Zr anomaly (Zr_N/Nd_N = 2.1-2.3, compared to 0.4-0.9 in oikocrystic clinopyroxenes). There is no correlation between Cr and incompatible element contents in clinopyroxene from the different rock-types. Taken as a whole, clinopyroxene from the Pineto gabbroic sequence (see also Sanfilippo et al., 2014; 2015) is chemically indistinguishable from clinopyroxene in modern abyssal gabbros (e.g., Drouin et al., 2009), thereby testifying chemical equilibrium with melts closely similar to MORB.

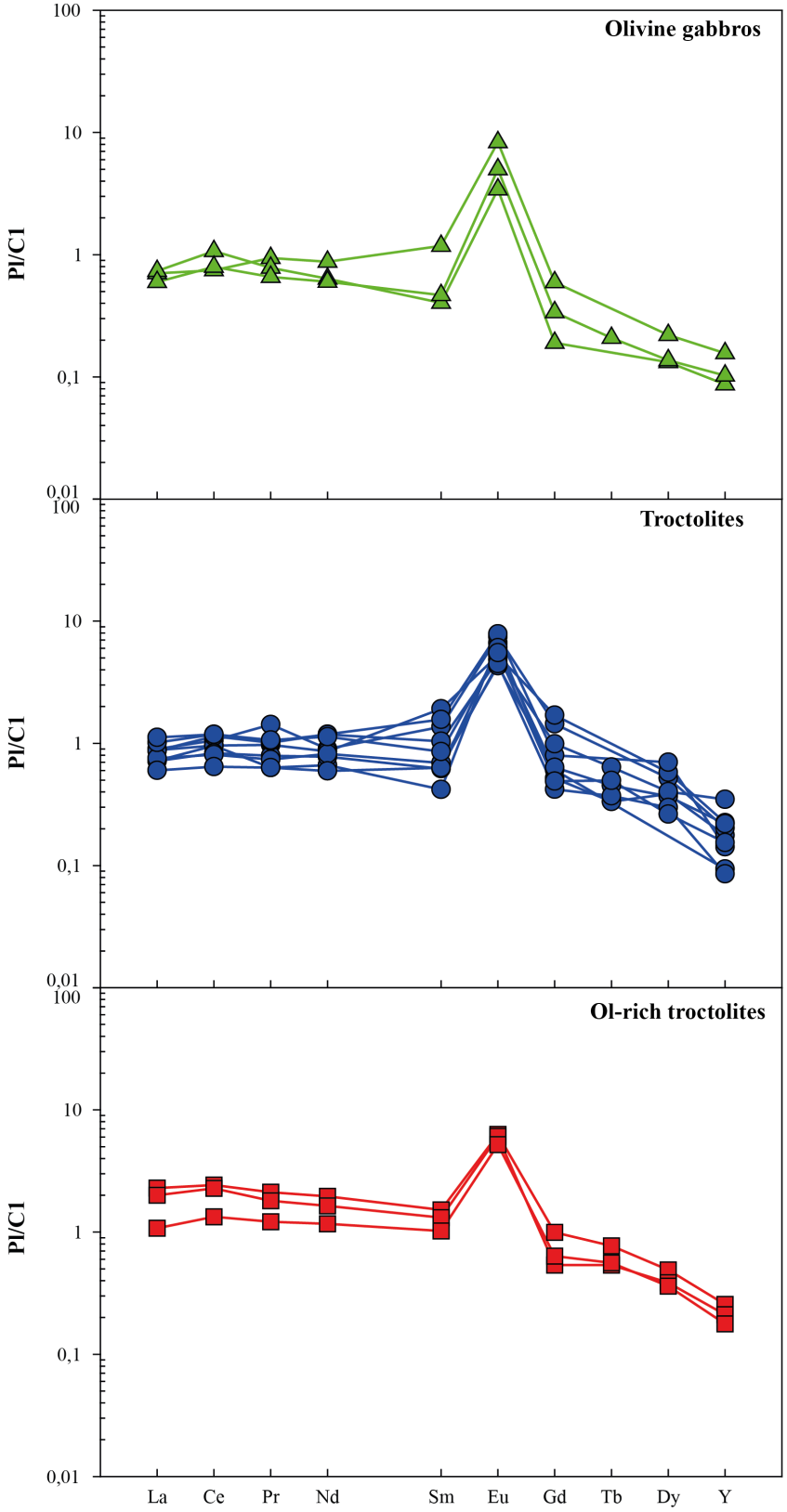

Figure 6: REE patterns for plagioclase cores normalised to C1 chondrite (Lyubetskaya & Korenaga, 2007).

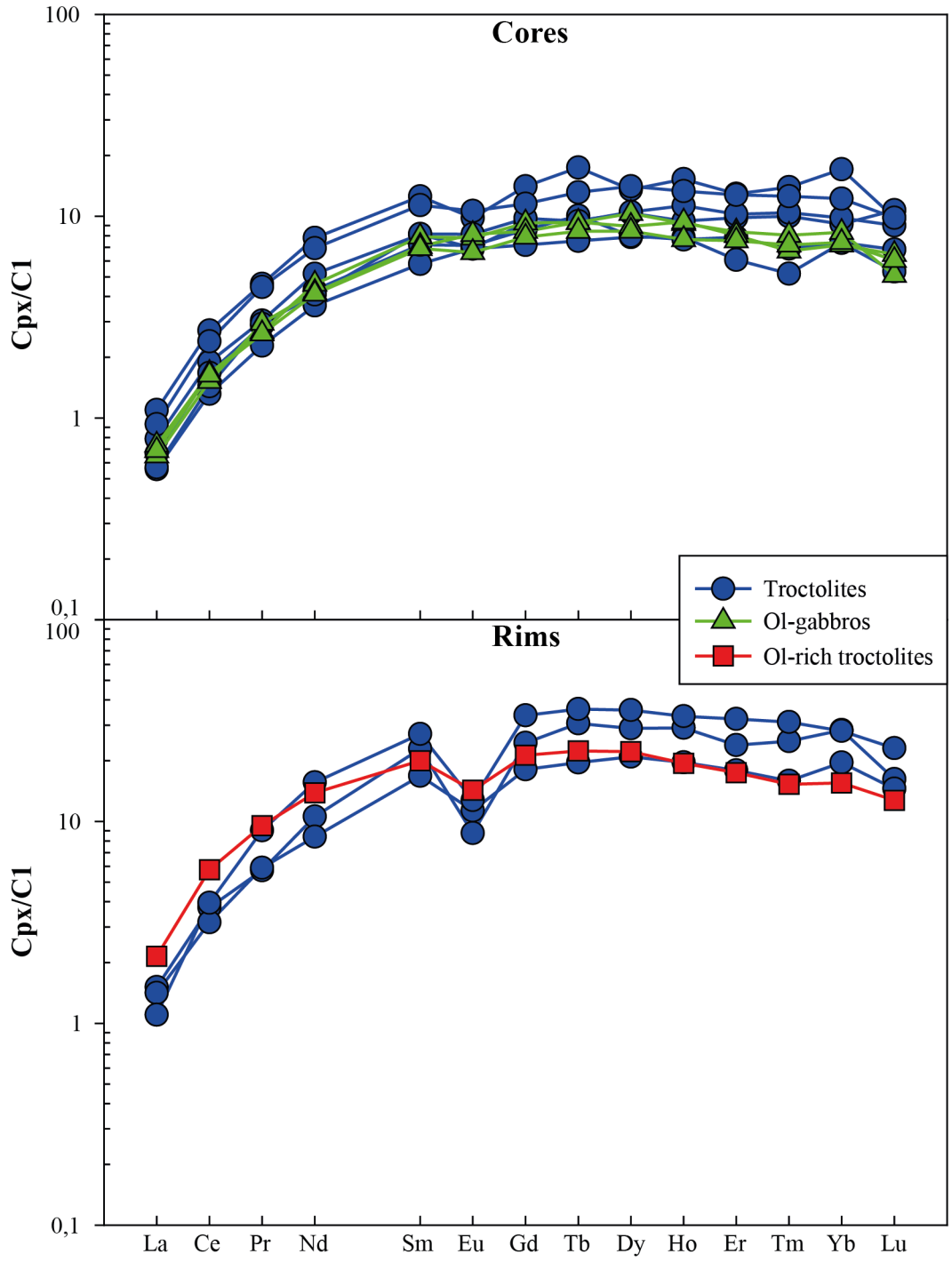

Figure 7: REE patterns for clinopyroxene cores and rims normalised to C1 chondrite (Lyubetskaya & Korenaga, 2007).

6. Geothermometry

The REE in plagioclase-clinopyroxene geothermometer from Sun and Liang (2017) was applied to selected rock samples. A pressure of 0.2 GPa and a water content of 0.2 wt% were assumed in the calculations. The REE partitioning between plagioclase and clinopyroxene is reported in figure 10. The results are reported in Table 2 together with the estimates from Sanfilippo and Tribuzio (2013) obtained on the basis of the Ca-in-olivine method by Brey and Kohler (1990). We also calculated temperature estimates on the basis of the Ca-in-orthopyroxene method by Brey and Kholer (1990).

The REE in plagioclase-clinopyroxene geothermometer (Sun and Liang, 2017) gave values ranging 1120 to 1170 °C, with no correlation with rock type. These temperature estimates are higher than those obtained on the basis of Ca concentrations in orthopyroxene and olivine (Brey and Kohler, 1990), which yielded a temperature interval of 970-900 and 950-840 °C, respectively. The high values of the equilibrium temperature of REE between Cpx and Pl are close to the solidus temperatures for the two phases and suggest that subsolidus re-equilibration did not affected the REE budget of these minerals. On the contrary, the diffusion of Ca between olivine, clinopyroxene and orthopyroxene occurred at subsolidus conditions. These data confirm that the REE-in plagioclase-clinopyroxene thermometer can be used to constrain the crystallization temperature of plunotic rocks (Sun and Liang, 2017).

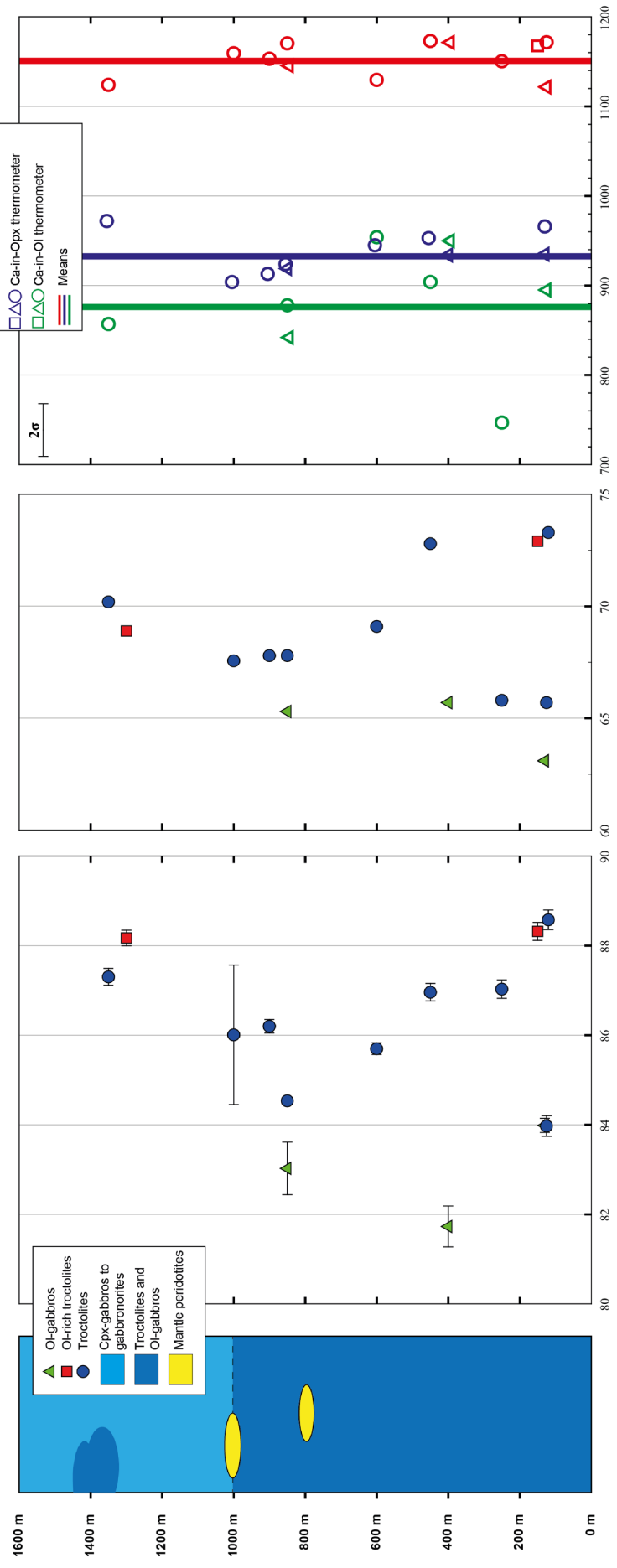

Figure 8: Forsterite proportion of olivines (mol%) (Sanfilippo & Tribuzio, 2013), anorthite content of plagioclases (mol%) (Sanfilippo & Tribuzio, 2013) and temperature estimates for the Pineto gabbroic sequence as a function of the stratigraphic height. The temperature estimates were obtained through the REE-in-Pl-Cpx geothermometer of Sun and Liang (2017) and the Ca-in-Opx geothermometer of Brey and Kohler (1990). The figure also reports the Ca-in-Ol temperature estimates from Sanfilippo & Tribuzio (2013). Data are averaged per sample; the error bars represent one SD of the mean value.

7. Discussion

7.1 Evidence for an open system magmatic evolution

The whole-rock major element compositions discriminate the different rock-types. For instance, although the most evolved troctolites and the olivine-gabbros have comparable Mg#, the latter are distinguished in the lower Al_2O_3 and NaO, and the higher CaO and TiO_2 contents, in response to the lower plagioclase/clinopyroxene ratios. Similarly, the troctolites and the olivine-gabbros display sharply different incompatible trace elements compositions, especially for those elements preferentially incorporated within the clinopyroxene (Cr, Sc, V, Y, REE and Zr). Major and trace elements whole-rock compositions are therefore controlled by the modal compositions of the different rock types. Nevertheless, the troctolites show: (i) a rough positive correlation between Ni and Mg#, and (ii) rough negative correlations between incompatible elements (e.g., Na_2O, TiO_2, Y, Zr, Sc, V) and Mg#. This documents that the whole-rock compositions are also constrained by the chemistry of the melts crystallizing these rocks.

The whole-rock incompatible trace element compositions cannot discriminate the olivine-rich troctolites from the troctolites. This is counterintuitive, as one would expect the olivine-rich troctolites having lower concentrations of incompatible trace elements than the troctolites, where plagioclase is up to 70 wt%. This is related to the fact that plagioclase from the olivine-rich troctolites is typically enriched in incompatible elements compared to plagioclase from the troctolites (and the olivine-gabbros). In addition, the concentrations of incompatible trace elements in the olivine-rich troctolites and the troctolites radically change in conjunction with the clinopyroxene modal amounts.

The Cr contents of the olivine-gabbros are higher than those of the troctolite at same Mg#. Among the different phases contained in these rocks, chromium is compatible in spinel, where it represents a major element, and clinopyroxene. Consistently, the olivine-rich troctolites have the highest spinel modal amounts and the highest Cr concentrations among the rocks considered in this study. However, spinel in not present in the olivine-gabbros, thereby implying that clinopyroxene is the only Cr repository in these rocks. The Cr enrichment of the olivine-gabbros agrees with the previous observation that clinopyroxene from these rocks has anomalously high Cr contents. Sanfilippo and Tribuzio (2013) used this observation to suggest that the clinopyroxene in olivine-gabbros from the Pineto ophiolite formed by melts enriched in Cr by the local assimilation of spinel from a previous olivine-plagioclase-spinel, i.e. troctolitic, matrix (see also Lissenberg and Dick, 2008). This hypothesis is further sustained here, where the addition of a Cr-rich component

is necessary to explain the high Cr contents in olivine-gabbros.

The concentration of incompatible trace elements in plagioclase are positively correlated with the anorthite molar proportion. This is inconsistent with crystallization of plagioclase from a melt following the typical fractionation line of MORB melt under low pressure conditions (olivine → olivine + plagioclase → olivine + plagioclase + clinopyroxene; Grove et al., 1992), which implies that plagioclase is gradually more enriched in incompatible elements as crystallization proceeds. We modeled a fractional crystallization process documenting that the most primitive troctolite (PI16) may be produced by fractionation of a primitive melt saturated in olivine + plagioclase (Fig. 9). The model also predicts an Y increase in the melt, thereby implying an Y increase in the crystallizing plagioclase. Variations in anorthite molar proportions may lead to change in Y partition coefficient between plagioclase and melt. However, that the restricted variations in anorthite component of the plagioclase considered in this study are not expected to produce substantial changes in plagioclase/melt Y partitioning. Hence, the chemical evolution of the plagioclase cannot be related to fractional crystallization alone, starting from parental melts with similar compositions.

Olivine from the olivine-gabbros and troctolite PI56 have lower incompatible trace elements than olivine from troctolites free of clinopyroxene oikocrysts, although the latter have slightly higher forsterite amounts (Sanfilippo et al., 2015). Similar to what discussed for plagioclase, this characteristic is inconsistent with formation of the olivine-gabbros from the same melt crystallizing the troctolites. The low incompatible trace element compositions of olivine from the olivine-gabbros was interpreted to be produced by local dissolution of an olivine + plagioclase matrix (and consequent depletion of the olivine) and concomitant crystallization of clinopyroxene.

In summary, the major element bulk rock and mineral compositions of the troctolite/olivine-gabbro association from the Pineto ophiolite are inconsistent with formation by MORB melts crystallizing following a typical low-pressure crystal line of descent. The trace elements compositions of olivine, plagioclase and clinopyroxene document that the trace element budget of these rocks is controlled by crystallization in an open evolution system. Hereafter, we will discuss how interaction between pre-existing crystals and migrating melts led to redistribution of the trace elements among the different mineral phases.

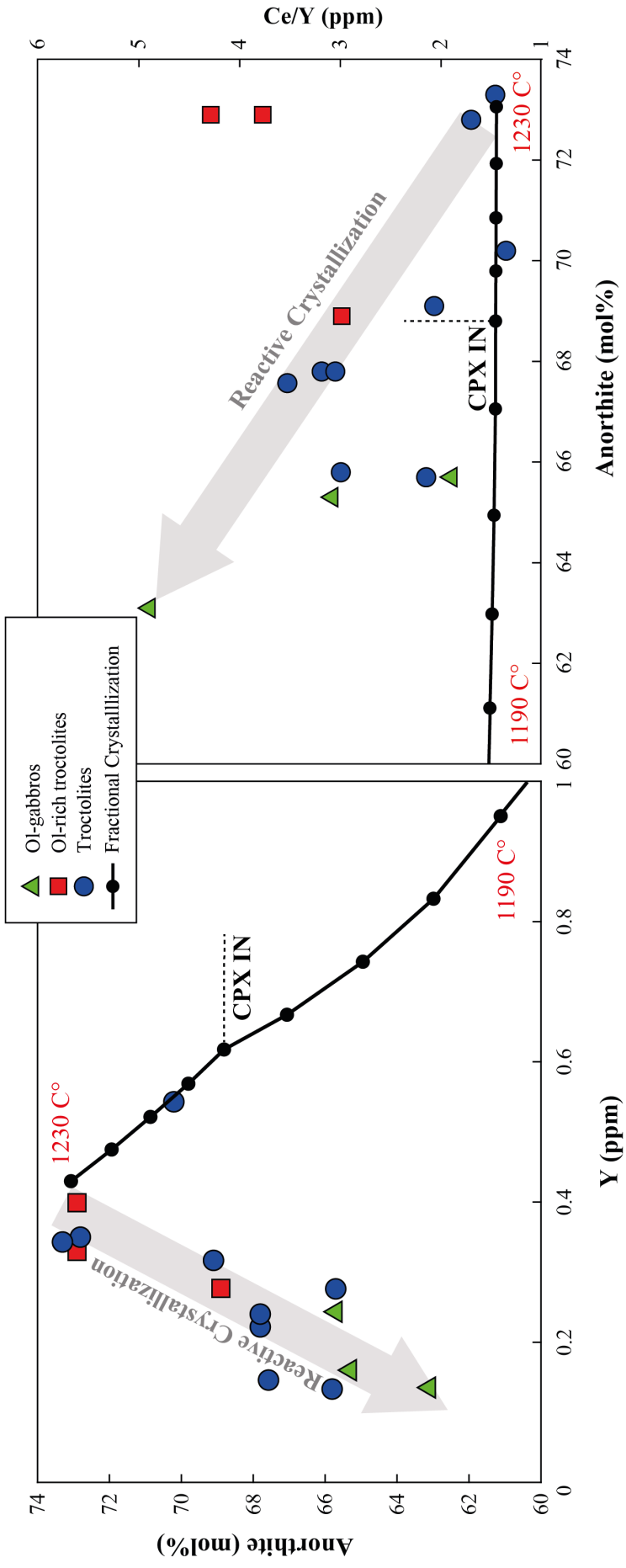

Figure 9: Anorthite contents of plagioclase vs. Y (ppm) and Ce/Y concentrations. The figures also report the composition of plagioclase in equilibrium with melt obtained by fractional crystallization model using the thermodynamic program PELE (Boudreau, 1999). Parental melt has major elements compositions of experimentally derived basalt from Kinzler and Grove (1993) (SiO_2 = 48.54; TiO_2 = 0.9; Al_2O_3 = 17.1; FeO = 6.97; MgO = 11.57; CaO = 11.22; Na_2O = 2.48 wt%) and Y and Ce compositions (18.15 and 5.7 ppm respectively) of the melt in chemical equilibrium with the mean Y and Ce contents of the most primitive plagioclase (troctolite sample PI16). Each step consists in a decrease of 5 °C in temperature at constant pressure of 2.5 kbar. The dashed lines represent the appearance of clinopyroxene as crystallizing phase. The grey arrow indicates the theoretical path of the reactive crystallization identified by the sample suite.

7.2 Origin of the trace element variability in olivine, plagioclase and clinopyroxene

Previous studies proposed that the trace element compositions of olivine from the troctolite/olivine-gabbro association of the Pineto ophiolite are inconsistent with a lithological evolution constrained by fractional crystallization alone (Sanfilippo et al., 2014; 2015). A two-stage model in which a crystal mush including olivine + plagioclase + spinel (± clinopyroxene) experienced reactive melt migration was instead proposed. During the early phase of melt migration, olivine experienced dissolution-recrystallization, thereby producing subhedral olivine with a large variability in incompatible trace element compositions (i.e., Ti, Zr and Y). When the migration process proceeded, the migrating melts evolved through a process of assimilation-fractional crystallization (DePaolo, 1981). The melts started to follow a liquid line of descent distinct from that expected by fractional crystallization alone, thereby leading to the early clinopyroxene saturation. The formation of Mg-rich clinopyroxene at the expenses of the dissolved olivine enabled olivine with depleted trace element signature to be preserved, as observed in the olivine-gabbros and the troctolites with clinopyroxene oikocrysts.

The olivine reactive dissolution evolution could be associated with dissolution-recrystallization of plagioclase. Evidence for plagioclase dissolution-recrystallization was provided by chemical maps of abyssal olivine-gabbros and troctolites, where resorbed cores enriched in anorthite component are locally present within plagioclase grains embedded in clinopyroxene oikocrysts (Lissenberg et al, 2014; Lissenberg and MacLeod, 2016). A process of dissolution of anorthite-rich plagioclase followed by reprecipitation of anorthite-poor plagioclase may explain the anomalous incompatible element compositions of the plagioclase from the troctolites and the olivine-gabbros.

Among the troctolite suite, sample PI16 has plagioclase and olivine with the highest amount of anorthite and forsterite component, and the highest whole-rock Mg# and Ni values. In addition, troctolite PI16 lacks clinopyroxene, orthopyroxene, amphibole and Fe-Ti-oxide phases, and has the lowermost concentrations of incompatible trace elements. However, plagioclase from this sample has relatively high concentrations of incompatible trace elements and no pronounced positive Eu anomaly. Similarly, olivine from troctolite PI16 is relatively rich in incompatible trace elements compared to olivine from the olivine-gabbros. Hence, we assume this sample as the one that crystallized from the most primitive meltor, under a melt-rock reaction perspective, the least reacted with the migrating melts.

A crystal-mush with a composition similar to sample PI16 could be percolated by a melt dissolving olivine and plagioclase and crystallizing the same phases (± clinopyroxene) with

sligthly lower amounts of forsterite and anorthite component. This process produces a variation in the incompatible element ratio of the crystallizing phases (Coogan et al, 2000; Gao et al., 2007; Sanfilippo et al., 2014; Lissenberg et al., 2013). This process leads to a sharp increase in the highly incompatible elements (Zr, Ti, LREE) compared to moderately incompatible elements (Y, HREE), thereby explaining the Zr/REE fractionation typically observed in clinopyroxene core-rim traverses (see also Coogan, 2007; Lissenberg and MacLeod, 2016).

At high mass assimilated/mass crystallized ratio (M~1), this process may lead to a gradual decrease in moderately incompatible trace elements, such as Y, thereby forming melts gradually depleted in these elements as the melt mass decreases. This process may explain why Y contents in plagioclase from the troctolites and the olivine-gabbros decreases with decreasing anorthite component, whereas highly incompatible elements such as La and Ce remain nearly constant.

In summary, we propose a reactive scenario where a crystal mush formed by olivine and plagioclase is locally absorbed by percolating melts, which re-crystallize olivine and plagioclase at lower Fo and An contents. This process can possibly form mineral retaining no textural evidence of dissolution processes, but with the composition gradually shifted towards that of the migrating magma (e.g., Kvassens and Grove, 2008; Lissenberg and MacLeod, 2016).The interacting melt follows a liquid line of descent different to that typically inferred for fractional crystallization processes, favoring the formation of high-Mg# clinopyroxene. Our data therefore sustain the idea that the lithological transition from troctolites to Ol-gabbros in the Pineto gabbroic sequence was controlled by magmatic evolution in an open system.

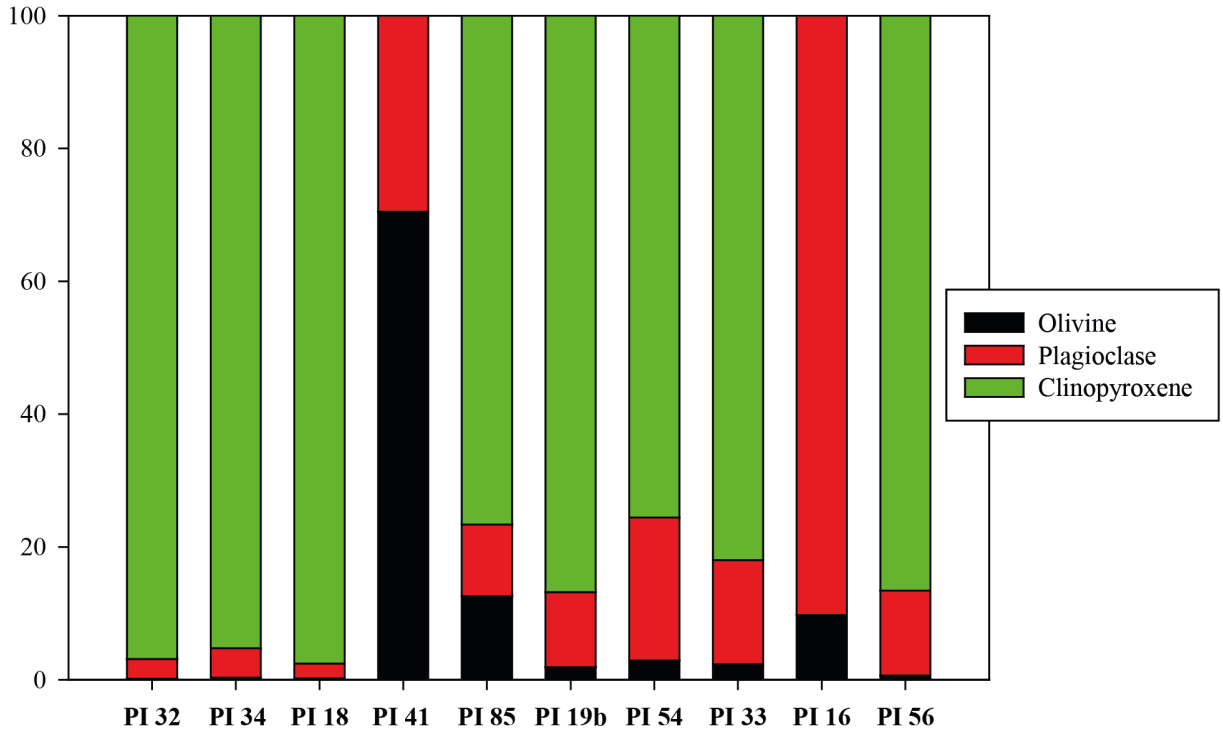

Figure 10: Y distribution between three different mineral phases for multiple samples.

7.3 Role of reactive migration process on the bulk-rock trace element compositions

Fig. 10 shows a mass balance calculation used to quantify the role of each mineral phase into the trace element budget of the different rock-types. To avoid any error related to analytical uncertainties (especially in olivine), we used Y to represent the incompatible trace elements. The calculation considers the modal compositions, as computed on the basis of major element compositions of whole-rocks and minerals (Sanfilippo and Tribuzio, 2013a), and trace elements mineral analyses in this and previous studies (Sanfilippo et al., 2014; 2015). The calculation shows that clinopyroxene has the main control on the incompatible trace element budget of these rocks. However, there are large differences in the trace element partitioning in the different rock-type. In the troctolites and the olivine-rich troctolites, clinopyroxene incorporates 75-85% of the whole-rock Y budget, whereas in the olivine-gabbros Y is almost entirely incorporated into clinopyroxene (more than 95%). Olivine and plagioclase respectively include 0.6-12% and 10-20% of the whole-rock Y budget in the troctolites and the olivine-rich troctolites, whereas they contribute only to a minor extent in the olivine-gabbros (<0.3% for olivine and 2-4% for plagioclase). Note that the weighted sum of the Y contents of the different phases is often lower than the whole-rock Y compositions. This can be related to (i) the role of interstitial accessory phases (such as amphibole) and/or (ii) to the trace element zoning of clinopyroxene (i.e. rims typically Y-enriched with repsect to to the cores), as documented in MOR-type olivine-gabbros worldwide (e.g., Tribuzio et al., 1999). The difference between calculated and observed whole-rock values reaches 50% in the olivine-gabbros. However, the mass balance calculations document that the distribution of incompatible trace elements among olivine, plagioclase and clinopyroxene varies in conjunction with the rock-type. In the olivine-gabbros, they are more preferentially incorporated by clinopyroxene (relative to plagioclase and olivine) compared to the same minerals in the troctolites. This observation is consistent with the fact that plagioclase and olivine from the olivine gabbros have lower concentrations of incompatible trace elements than expected if the magmatic evolution was ruled by fractional crystallization. The high temperature of equilibration of the trace elements between the different phases (Fig. 8) excludes that these feature can be related to post-cumulus diffusion processes. Reactive melt migration was thereby responsible to redistribute the incompatible trace elements amongst this section of lower oceanic crust.

8. Conclusions

This study underlines the importance of a complete characterization of gabbroic samples to understand their geochemical evolution. Based on major element bulk rock and mineral compositions we confirm the idea that the troctolite/olivine-gabbro association from the Pineto ophiolite formed as cumulate from the crystallization of MORB-type melts. These melt evolved in shallow magma chambers following the typical low-pressure crystal line of descent of abyssal gabbros exposed at modern slow spreading ridge. However, the trace elements compositions of olivine, plagioclase and clinopyroxene document that the trace element budget of these rocks was controlled by crystallization in an open system. Interaction between the pre-existing crystal matrix and migrating melts led to substantial modifications in the incompatible elements composition, causing deviation from trends expected during fractional crystallization process. In addition, here, we show that reactive melt migration process also controlled the whole rock budget of the different lithologies and produced variation unexpected if based on fractional crystallization hypothesis. In particular, independently on the overall bulk composition of the rock, the relative amount of incompatible trace elements incorporated in olivine/plagioclase and clinopyroxene varies significantly with the rock type, showing a preferential uptake of trace elements in clinopyroxene in the olivine gabbros compared to the troctolites. This suggests that reactive melt migration processes tend to redistribute the incompatible trace elements throughout the lower oceanic crust.

9. References

Beccaluva L, Ohnenstetter D, Ohnenstetter M, Venturelli G (1977) The trace element geochemistry of corsican ophiolites. Contrib Miner Petrol 64:11–3

Brey, G. P., & Köhler, T. (1990). Geothermobarometry in four-phase lherzolites II. New thermobarometers, and practical assessment of existing thermobarometers. Journal of Petrology, 31(6), 1353-1378.

Coogan, L. A., Jenkin, G. R. T., & Wilson, R. N. (2007). Contrasting cooling rates in the lower oceanic crust at fast-and slow-spreading ridges revealed by geospeedometry. Journal of Petrology, 48(11), 2211-2231.

Coogan, L. A., Saunders, A. D., Kempton, P. D., & Norry, M. J. (2000). Evidence from oceanic gabbros for porous melt migration within a crystal mush beneath the Mid-Atlantic Ridge. Geochemistry, Geophysics, Geosystems, 1(9).

Dick HJB et al (2000) A long in-situ section of the lower ocean crust: results of ODP Leg 176 drilling at the Southwest Indian Ridge. Earth Planet Sci Lett 179:31–51. doi:10.1016/S0012-821X (00)00102-3

DePaolo, D. J. (1981). Trace element and isotopic effects of combined wallrock assimilation and fractional crystallization. Earth and planetary science letters, 53(2), 189-202.

Durand-Delga M, Fondecave-Wallez MJ, Rossi P (2005) L'unite ´ ophiolitique de Pineto (Corse): signification du de ´tritisme continental dans sa couverture de flysch albo-ce ´nomanien. CR Geosci 337:1084–1095

Gale, A., Dalton, C. A., Langmuir, C. H., Su, Y., & Schilling, J. G. (2013). The mean composition of ocean ridge basalts. Geochemistry, Geophysics, Geosystems, 14(3), 489-518.

Gao, Y., Hoefs, J., Hellebrand, E., von der Handt, A., & Snow, J. E. (2007). Trace element zoning in pyroxenes from ODP Hole 735B gabbros: diffusive exchange or synkinematic crystal fractionation? Contributions to Mineralogy and Petrology, 153(4), 429-442.

Hamada M, Fujii T (2007) H2O-rich island arc low-K tholeiite magma inferred from Ca-rich plagioclase-melt inclusion equilibria. Geochem J, 41.

Ildefonse B, Blackman DK, John BE, Ohara Y, Miller DJ, MacLeod CJ, Party IODPES (2007) Oceanic core complexes and crustal accretion at slow spreading ridges. Geology 35:623–626

Kvassnes, A. J., & Grove, T. L. (2008). How partial melts of mafic lower crust affect ascending magmas at oceanic ridges. Contributions to Mineralogy and Petrology, 156(1), 49-71.

Lissenberg, C. J., & MacLeod, C. J. (2016). A reactive porous flow control on mid-ocean ridge magmatic evolution. Journal of Petrology, 57(11-12), 2195-2220.

Lissenberg, C. J., MacLeod, C. J., Howard, K. A., & Godard, M. (2013). Pervasive reactive melt migration through fast-spreading lower oceanic crust (Hess Deep, equatorial Pacific Ocean). Earth and Planetary Science Letters, 361, 436-447.

Lyubetskaya, T., & Korenaga, J. (2007). Chemical composition of Earth's primitive mantle and its variance: 1. Method and results. Journal of Geophysical Research: Solid Earth, 112(B3).

McDonough, W. F., & Sun, S. S. (1995). The composition of the Earth. Chemical geology, 120(3-4), 223-253.

Nimis P., Ulmer P. (1998) Clinopyroxene geobarometry of magmatic rocks. Part 1. An expanded structural geobarometer for anhydrous and hydrous, basic and ultrabasic systems, Contributions to Mineralogy and Petrology, vol. 133 (pg. 122-135)

Putirka, K. (2016). Amphibole thermometers and barometers for igneous systems and some implications for eruption mechanisms of felsic magmas at arc volcanoes. American Mineralogist, 101(4), 841-858.

Renna M.R., Tribuzio R., Ottolini L. (2016). New perspectives on the origin of olivine-rich troctolites and associated harrisites from the Ligurian ophiolites (Italy), J. Geol. Soc.

Renna MR, Tribuzio R (2007) Lower crustal cumulus pyroxenites from the external Liguride Units (Northern Appennine, Italy). Epitome 2007 (2):114

Rossi P, Durand-Delga M, Caron JM, Guieu G, Conchon O, Libourel G, Loy ¨e-Pilot MD (1994) Carte Ge ´ologique del la France et notice explicative de la feuille ‘‘Corte’’: BRGM n 1110, Orle ´an, France, scale 1:50000

Saccani E, Bortolotti V, Marroni M, Pandolfi L, Photiades A (2008a) The Jurassic association of backarc basin ophiolites and calc-alkaline volcanics in the Guevgueli Complex (Northern Greece): implication for the evolution of the Vardar Zone. Ofioliti 33:209–227

Saccani E, Padoa E, Tassinari R (2000) Preliminary data on the Pineto gabbroic Massif and Nebbio basalts: progress toward the geochemical characterization of Alpine Corsica ophiolites. Ofioliti 25:75–85

Saccani E, Photiades A, Beccaluva L. (2008b) Petrogenesis andtectonic significance of IAT magma-types in the Hellenideophiolites as deduced from the Rhodiani ophiolites (Pelagonian zone, Greece). Lithos 104:71–84

Saccani E, Photiades A, Santato A, Zeda O (2008c) New evidence for supra-subduction zone ophiolites in the Vardar zone of Northern Greece: implications for the tectono-magmatic evolution of the Vardar oceanic basin. Ofioliti 33:65–85

Sanfilippo A, Tribuzio R (2013a) Origin of olivine-rich troctolites from the oceanic lithosphere: a comparison between the Alpine Jurassic ophiolites and modern slow spreading ridges. Ofioliti 38:89–99

Sanfilippo A, Tribuzio R (2013b) Building of the deepest crust at a fossil slow-spreading centre (Pineto gabbroic sequence, Alpine Jurassic ophiolites). Contrib Mineral Petrol 165:705–721

Sanfilippo, A., Tribuzio, R., Tiepolo, M., & Berno, D. (2015). Reactive flow as dominant evolution process in the lowermost oceanic crust: evidence from olivine of the Pineto ophiolite (Corsica). Contributions to Mineralogy and Petrology, 170, 1–12.

Shimizu, K., Liang, Y., Sun, C., Jackson, C. R., & Saal, A. E. (2017). Parameterized lattice strain models for REE partitioning between amphibole and silicate melt. American Mineralogist, 102(11), 2254-2267.

Sun, C., & Liang, Y. (2012). Distribution of REE between clinopyroxene and basaltic melt along a mantle adiabat: effects of major element composition, water, and temperature. Contributions to Mineralogy and Petrology, 163(5), 807-823.

Sun, C., & Liang, Y. (2017). A REE-in-plagioclase–clinopyroxene thermometer for crustal rocks. Contributions to Mineralogy and Petrology, 172(4), 24.

Smith, D. K., et al. (2014), Development and evolution of detachment faulting along 50 km of the Mid-Atlantic Ridge near 16.5N, Geochem. Geophys. Geosyst. 15, 4692–4711

Streckeisen, A. L. (1973). Plutonic rocks: Classification and nomenclature recommended by the IUGS Subcommission on the systematics of igneous rocks. Geotimes, 18, 26-30.

Tribuzio, R., Tiepolo, M., Vannucci, R. & Bottazzi, P. (1999). Trace element distribution within olivine-bearing gabbros from the Northern Apennine ophiolites (Italy): evidence for post-cumulus crystallization in MOR-type gabbroic rocks. Contributions to Mineralogy and Petrology 134, 123–133.

Whitney, D. L., & Evans, B. W. (2010). Abbreviations for names of rock-forming minerals. American mineralogist, 95(1), 185-187.

APPENDIX
TABLE DATA

Sample	PI41a#	PI85#	PI80	PI44#	PI62#	PI56	PI31#	PI54#	PI33#	PI49#	PI19#	PI16#	PI32#	PI34#	PI18#
Rock Type	Ol-rich troctolit	Ol-rich troctolit	Ol-rich troctolit	Troctolite	Troctolite	Troctolite	Troctolite	Troctolite	Troctolite	Troctolite	Troctolite	Troctolite	Ol-Gabbro	Ol-Gabbro	Ol-Gabbro
Major elements (wt%)															
SiO2	38.48	37.37	38.38	44.84	46.28	46.21	49.1	46.34	45.66	47.92	47.78	44.48	49.99	51.69	49.56
Al2O3	3.41	6.03	4.99	21.5	20.89	19.74	21.78	21.99	21.08	21.5	20.34	21.43	18.21	15.96	17.17
Fe2O3(T)	9.95	9.24	9.79	3.69	4.12	4.17	4.15	4.33	3.84	3.59	4.78	3.67	3.88	4.43	3.82
FeO(T)	9.0	8.3	8.8	3.3	3.7	3.8	3.7	3.9	3.5	3.2	4.3	3.3	3.5	4.0	3.4
MnO	0.139	0.121	0.141	0.055	0.064	0.063	0.06	0.067	0.057	0.053	0.075	0.051	0.066	0.088	0.071
MgO	38.51	34.2	36.52	11.84	11.46	13.26	10.05	11.75	12.11	11.94	11.85	13.22	9.32	10.97	10.29
CaO	1.6	2.83	2.27	10.49	11.32	10.15	10.69	10.22	11.07	11	10.85	10.6	13.58	13.9	13.77
Na2O	0.21	0.4	0.4	2.05	2.2	2.2	2.68	2.39	2.08	2.2	2.53	1.81	2.54	2.31	2.18
K2O	< 0.01	< 0.01	< 0.01	0.03	0.03	0.02	0.02	0.02	0.04	0.02	0.03	0.03	0.05	0.02	0.07
TiO2	0.033	0.065	0.08	0.11	0.077	0.066	0.082	0.075	0.093	0.052	0.104	0.04	0.213	0.267	0.208
P2O5	0.01	0.02	< 0.01	0.02	< 0.01	0.01	< 0.01	< 0.01	0.02	< 0.01	< 0.01	0.01	< 0.01	< 0.01	0.01
LOI	7.21	9.33	7.74	4.99	2.63	4.04	1.73	3.75	4.04	2.08	2.65	3.55	1.72	0.83	1.39
Total	99.56	99.62	100.3	99.61	99.08	99.93	100.3	100.9	100.1	100.4	101	98.91	99.58	100.5	98.54
Trace elements (ppm)															
Sc	6	6	6	4	8	6	7	5	7	6	10	2	27	37	30
Be	< 1	< 1	< 1	< 1	< 1	< 1	< 1	< 1	< 1	< 1	< 1	< 1	< 1	< 1	< 1
V	15	37	33	18	29	22	24	19	29	17	38	8	97	118	96
Cr	640	3320	1870	110	390	430	330	140	480	440	510	550	1180	840	1690
Co	116	102	115	36	39	43	38	39	34	38	42	39	25	32	28
Ni	1690	1330	1570	510	360	470	330	350	370	400	320	510	190	240	240
Cu	110	60	90	70	60	60	100	50	40	60	70	20	70	110	100
Zn	70	50	50	50	< 30	< 30	< 30	40	< 30	30	< 30	< 30	< 30	< 30	< 30
Ga	2	3	3	9	9	9	11	9	9	10	10	9	11	10	9
Ge	1	0.8	0.8	0.8	0.7	0.7	0.9	0.5	0.8	0.9	0.8	0.8	0.9	1.4	1.4
As	< 5	< 5	< 5	< 5	< 5	< 5	< 5	< 5	< 5	< 5	< 5	< 5	< 5	< 5	< 5
Rb	< 1	< 1	< 1	< 1	< 1	< 1	< 1	< 1	< 1	< 1	< 1	< 1	2	< 1	< 1
Sr	26	46	39	193	156	152	161	163	156	160	169	151	140	139	139
Y	0.7	0.9	1.3	1.9	1.5	1.2	1.5	1.2	1.9	0.9	2.1	0.6	5.4	6.9	5.5
Zr	3	3	3	8	2	3	3	14	10	2	3	4	21	10	16
Nb	< 0.2	0.6	< 0.2	< 0.2	< 0.2	< 0.2	0.3	4.1	1.1	< 0.2	< 0.2	1.2	2.2	< 0.2	1.3
Mo	< 2	< 2	< 2	< 2	< 2	< 2	< 2	< 2	< 2	< 2	< 2	< 2	< 2	< 2	< 2
Ag	< 0.5	< 0.5	< 0.5	< 0.5	< 0.5	< 0.5	< 0.5	< 0.5	< 0.5	< 0.5	< 0.5	< 0.5	< 0.5	< 0.5	< 0.5
In	< 0.1	< 0.1	< 0.1	< 0.1	< 0.1	< 0.1	< 0.1	< 0.1	< 0.1	< 0.1	< 0.1	< 0.1	< 0.1	< 0.1	< 0.1
Sn	2	1	< 1	< 1	< 1	< 1	< 1	6	< 1	< 1	< 1	< 1	1	< 1	< 1
Sb	0.7	0.3	< 0.2	0.6	< 0.2	< 0.2	0.6	< 0.2	< 0.2	0.5	< 0.2	< 0.2	< 0.2	0.5	< 0.2
Cs	< 0.1	< 0.1	< 0.1	< 0.1	< 0.1	< 0.1	< 0.1	< 0.1	< 0.1	< 0.1	< 0.1	< 0.1	< 0.1	< 0.1	< 0.1
Ba	< 3	< 3	< 3	5	< 3	< 3	3	< 3	4	< 3	3	< 3	< 3	< 3	5
La	-	0.23	0.1	0.59	0.22	0.1	1.73	0.25	0.27	-	0.36	0.25	0.73	0.47	0.43
Ce	-	0.59	0.5	1.27	0.61	0.4	2.61	0.72	0.79	-	0.95	0.6	1.74	1.34	1.32
Pr	-	0.09	0.08	0.18	0.1	0.07	0.29	0.11	0.13	0.07	0.14	0.09	0.27	0.26	0.24
Nd	0.2	0.44	0.4	0.9	0.48	0.5	1.09	0.53	0.67	0.37	0.72	0.41	1.38	1.5	1.3
Sm	0.07	0.11	0.2	0.25	0.16	0.2	0.22	0.16	0.21	0.10	0.25	0.11	0.55	0.67	0.54
Eu	0.06	0.09	0.12	0.27	0.23	0.21	0.28	0.23	0.21	0.21	0.28	0.17	0.35	0.44	0.35
Gd	0.09	0.15	0.18	0.3	0.29	0.19	0.23	0.24	0.27	0.16	0.34	0.12	0.8	1.06	0.85
Tb	0.01	0.02	0.03	0.06	0.04	0.03	0.04	0.04	0.06	0.03	0.07	0.02	0.16	0.18	0.16
Dy	0.09	0.17	0.2	0.38	0.29	0.2	0.25	0.24	0.34	0.17	0.38	0.12	1	1.26	1.02
Ho	0.02	0.04	0.04	0.07	0.06	0.05	0.05	0.05	0.08	0.03	0.08	0.03	0.22	0.27	0.23
Er	0.08	0.1	0.1	0.2	0.14	0.1	0.15	0.14	0.21	0.1	0.23	0.08	0.57	0.78	0.59
Tm	0.02	0.02	< 0.005	0.03	0.02	< 0.005	0.02	0.02	0.04	0.01	0.03	0.01	0.10	0.11	0.09
Yb	0.11	0.14	0.2	0.18	0.12	0.1	0.15	0.14	0.22	0.09	0.22	0.09	0.58	0.61	0.58
Lu	0.02	0.022	< 0.002	0.028	0.021	< 0.002	0.023	0.026	0.034	0.016	0.037	0.014	0.085	0.094	0.083
Hf	0.1	< 0.1	< 0.1	0.2	< 0.1	< 0.1	< 0.1	0.2	0.4	0.1	< 0.1	0.1	0.5	0.3	0.5
Ta	< 0.01	0.56	< 0.01	< 0.01	< 0.01	< 0.01	< 0.01	3.21	< 0.01	< 0.01	0.02	0.03	0.02	< 0.01	0.03
W	0.5	32.9	1.8	0.5	1.4	< 0.5	1	179	< 0.5	< 0.5	0.7	< 0.5	< 0.5	< 0.5	< 0.5
Tl	< 0.05	< 0.05	< 0.05	< 0.05	< 0.05	< 0.05	< 0.05	< 0.05	< 0.05	< 0.05	< 0.05	< 0.05	< 0.05	< 0.05	< 0.05
Pb	< 5	< 5	< 5	< 5	< 5	< 5	< 5	< 5	< 5	< 5	< 5	< 5	< 5	< 5	< 5
Bi	< 0.1	0.1	< 0.1	< 0.1	< 0.1	< 0.1	< 0.1	0.8	< 0.1	< 0.1	< 0.1	< 0.1	< 0.1	< 0.1	< 0.1
Th	< 0.05	< 0.05	< 0.05	< 0.05	< 0.05	< 0.05	< 0.05	< 0.05	0.15	< 0.05	< 0.05	0.33	0.36	< 0.05	0.38
U	< 0.01	< 0.01	< 0.01	< 0.01	< 0.01	< 0.01	0.04	0.1	0.16	< 0.01	< 0.01	0.22	0.12	< 0.01	0.27
Mg#	88.5	88.0	88.1	86.4	84.6	86.3	82.8	84.3	86.2	86.8	83.1	87.7	82.6	83.1	84.2

Table 2: Whole rock major and trace element compositions of selected samples.

	Plagioclase															
Sample	PI41a		PI85		PI80		PI44		PI62		PI56		PI31		PI54	
Rock Type	Ol-rich troctolite		Ol-rich troctolite		Ol-rich troctolite		Troctolite		Troctolite		Troctolite		Troctolite		Troctolite	
n.	15	std	13	std	8	std	9	std	5	std		std	11	std	15	std
Li	0.75	0.46	1.77	1.39	2.50	1.63	3.62	1.01	0.37	0.27	6.08	4.89	0.94	1.22	1.03	0.97
B	2.07	0.97	2.70	1.00	1.91	1.09	10.9	3.51	-	-	3.60	1.50	2.58	0.80	1.47	0.44
Sc	2.00	0.53	1.40	0.59	1.91	0.87	2.41	0.48	2.47	0.81	2.25	0.31	3.04	1.29	2.42	1.36
TiO2	219	45.35	285	75.8	263	29.9	244	68.4	254.73	28.79	326	77.19	330	109.57	292	117.87
V	2.08	1.00	1.36	0.41	1.46	0.28	3.40	0.78	6.39	5.27	3.16	0.70	4.70	2.10	3.35	1.66
Cr	4.10	1.25	4.85	1.33	4.84	0.47	2.63	0.84	-	-	2.83	1.16	46.15	50.98	10.06	3.54
Co	0.70	0.62	0.39	0.23	0.53	0.30	0.20	0.04	1.14	1.02	0.89	0.47	0.78	0.56	1.32	1.53
Ni	3.81	8.22	1.88	1.50	2.46	2.24	0.45	0.26	4.61	3.75	3.89	4.29	2.98	2.39	2.74	0.89
Zn	16.4	19.2	11.31	10.21	25.52	24.49	3.93	3.20	16.05	6.81	19.92	16.27	24.95	2.68	19.7	17.2
Rb	0.41	0.25	0.26	0.22	0.32	0.16	0.06	0.02	0.32	0.06	0.18	0.19	0.81	0.48	0.80	0.40
Sr	237	51.17	253	26.2	252	27.4	229	13.01	212	22.1	236	5.19	218	22.83	220	8.63
Y	0.28	0.12	0.33	0.09	0.40	0.14	0.54	0.13	0.15	0.02	0.24	0.03	0.22	0.09	0.32	0.15
Zr	1.52	1.97	0.23	0.15	0.52	0.67	0.07	0.04	0.12	-	0.04	0.02	0.30	0.08	1.07	0.88
Nb	0.06	0.03	0.06	0.05	0.06	0.01	0.02	0.01	0.08	-	-	-	0.21	0.12	0.25	0.20
Cs	0.03	0.01	0.02	0.02	0.01	0.00	0.01	0.00	-	-	0.0	-	0.05	0.02	0.04	0.02
Ba	3.15	2.53	1.91	0.60	2.05	1.04	1.24	0.23	0.96	0.29	1.40	0.47	0.94	0.63	1.65	1.53
La	0.25	0.10	0.47	0.09	0.54	0.12	0.24	0.07	0.17	0.09	0.26	0.06	0.20	0.10	0.21	0.15
Ce	0.83	0.19	1.41	0.20	1.50	0.17	0.74	0.24	0.52	0.06	0.73	0.14	0.71	0.26	0.66	0.30
Pr	0.11	0.03	0.17	0.05	0.20	0.03	0.10	0.04	0.07	0.03	0.10	0.02	0.10	0.04	0.13	0.05
Nd	0.54	0.18	0.75	0.23	0.90	0.27	0.54	0.20	0.36	0.11	0.52	0.15	0.55	0.24	0.41	0.13
Sm	0.15	0.06	0.20	0.08	0.23	0.14	0.16	0.07	0.09	0.00	0.13	0.04	0.24	0.02	0.21	0.13
Eu	0.30	0.12	0.35	0.10	0.36	0.15	0.28	0.06	0.35	0.10	0.31	0.04	0.45	0.17	0.42	0.30
Gd	0.13	0.06	0.11	0.05	0.20	0.10	0.20	0.09	0.12	-	0.10	0.03	0.16	0.08	0.29	0.16
Tb	0.02	0.00	0.02	0.01	0.03	0.00	0.02	0.01	-	-	0.02	0.01	-	-	-	-
Dy	0.09	0.04	0.10	0.06	0.12	0.05	0.10	0.05	-	-	0.07	0.02	0.18	0.05	0.13	-
Ho	0.02	0.01	0.02	0.01	0.02	0.01	0.02	0.01	0.01	0.00	0.01	0.00	0.02	0.01	0.03	0.00
Er	0.07	0.02	0.07	0.02	0.06	0.02	0.07	0.05	-	-	0.04	0.03	0.07	-	0.23	0.14
Tm	0.01	-	0.01	-	0.07	-	0.01	0.00	-	-	0.01	0.01	-	-	-	-
Yb	-	-	0.08	-	-	-	0.06	0.01	-	-	0.05	0.01	-	-	0.54	-
Lu	-	-	-	-	0.01	0.01	0.01	0.00	-	-	0.02	0.01	-	-	0.12	-
Hf	0.12	0.09	-	-	0.14	0.14	0.09	-	-	-	0.1	-	0.09	0.02	0.07	-
Ta	0.06	0.03	0.01	-	0.06	0.03	0.02	0.00	0.06	0.01	0.0	-	-	-	0.16	0.10
Pb	0.33	0.34	0.19	0.14	0.45	0.34	0.21	0.09	0.38	0.16	0.3	0.1	0.16	0.08	0.26	0.12
Th	0.05	0.05	0.02	0.00	0.02	0.02	0.01	0.00	0.01	0.00	0.002	0.001	0.02	0.01	0.03	0.00
U	0.03	0.02	0.01	-	0.01	-	-	-	0.005	-	0.006	0.004	0.01	0.00	0.02	-

Table 3: Trace element compositions of plagioclase (average values, ppm).

Plagioclase														
PI33		PI49		P19		PI16		PI32		PI34		PI18		
Troctolite		Troctolite		Troctolite		Troctolite		Ol-gabbro		Ol-gabbro		Ol-gabbro		
7	std	9	std	4	std	17	std	11	std	12	std	2	std	
1.01	-	6.22	3.47	0.94	0.24	4.90	5.19	1.54	0.82	0.38	0.31	1.11	0.24	
2.14	0.18	7.21	3.98	-	-	3.17	1.87	3.98	0.91	2.04	1.17	0.62	-	
2.99	1.28	2.26	0.37	2.42	0.37	2.06	0.64	2.47	0.13	2.40	0.83	1.14	0.01	
227.59	66.19	228	20.94	305.59	36.50	264	49.4	269	68.90	234	23.70	477	50.1	
3.62	1.13	2.43	0.88	3.94	0.74	4.61	1.01	4.28	0.82	4.23	1.24	3.79	0.75	
6.68	0.49	3.97	3.73	-	-	9.99	7.87	2.73	2.06	9.98	0.26	2.97	0.77	
0.65	0.28	0.37	0.18	0.55	0.27	0.43	0.18	0.33	0.08	0.53	0.27	0.16	0.03	
1.33	0.64	0.97	1.02	0.67	0.38	4.22	12.52	0.97	0.38	1.93	1.36	0.62	0.28	
20.33	5.88	8.17	5.07	6.57	4.15	5.24	4.57	10.91	3.77	11.2	11.4	3.32	0.49	
0.39	0.13	0.11	0.06	0.22	0.19	0.09	0.07	0.10	0.03	0.36	0.48	0.02	-	
220.78	9.64	221	8.53	237.43	4.21	210	22.3	222	6.62	219	13.90	187.21	4.25	
0.35	0.13	0.13	0.04	0.28	0.03	0.34	0.12	0.16	0.05	0.24	0.10	0.14	0.03	
0.29	0.10	0.06	0.03	0.23	0.29	0.12	0.10	0.03	0.01	0.22	0.18	0.06	0.01	
0.27	0.03	0.02	0.02	0.02	-	0.02	0.01	0.01	0.00	0.08	0.06	-	-	
0.03	0.02	0.01	0.00	0.01	0.00	0.01	0.01	0.01	0.00	0.01	0.01	0.01	-	
0.88	0.38	1.09	0.56	1.26	0.31	0.66	0.15	1.24	0.17	1.62	0.61	0.83	0.03	
0.21	0.05	0.14	0.02	0.17	0.02	0.18	0.04	0.14	0.03	0.17	0.10	0.17	0.03	
0.59	0.17	0.40	0.04	0.59	0.09	0.50	0.09	0.49	0.07	0.46	0.18	0.66	0.06	
0.09	0.04	0.06	0.02	0.06	0.02	0.07	0.02	0.06	0.01	0.09	0.05	0.07	0.00	
0.40	0.23	0.27	0.06	0.31	0.02	0.38	0.11	0.28	0.04	0.40	0.23	0.29	0.02	
0.29	0.12	0.09	0.03	0.06	0.01	0.10	0.04	0.07	0.02	0.18	0.08	0.06	0.02	
0.30	0.07	0.26	0.04	0.38	0.01	0.25	0.04	0.29	0.03	0.47	0.25	0.20	0.02	
0.34	0.07	0.08	0.04	0.10	0.02	0.13	0.05	0.07	0.03	0.12	0.06	0.04	-	
0.07	-	0.01	0.00	0.01	0.01	0.02	0.01	0.01	0.00	0.03	0.02	-	-	
0.15	0.04	0.07	0.02	0.10	0.00	0.09	0.05	0.03	0.01	0.06	0.02	0.03	0.01	
0.04	0.02	0.01	0.00	0.02	0.01	0.02	0.01	0.01	0.00	0.02	0.01	0.01	-	
-	-	0.04	0.02	0.04	0.01	0.07	0.04	0.02	0.00	0.04	-	-	-	
-	-	0.00	0.00	0.01	-	0.01	0.00	0.01	0.00	-	-	-	-	
-	-	0.05	0.01	0.05	0.00	0.06	0.02	0.03	0.02	0.04	-	-	-	
-	-	0.01	0.00	-	-	0.01	0.01	0.00	0.00	0.01	0.00	-	-	
-	-	0.05	0.02	0.04	0.00	0.04	0.01	0.37	-	0.15	0.15	-	-	
-	-	0.01	0.00	-	-	0.01	0.00	0.00	-	0.12	0.05	-	-	
0.21	0.09	0.33	0.26	0.10	0.05	0.20	0.18	0.33	0.15	0.38	0.27	0.13	0.05	
-	-	-	-	-	-	0.01	0.00	0.00	0.00	0.03	0.02	-	-	
-	-	0.00	0.00	0.01	-	0.01	-	0.00	0.00	0.01	0.00	-	-	

Table 3: continued

	Clinopyroxene															
Sample	PI85		PI44		PI62		PI56		PI31		PI54		PI54	
Rock Type	Ol-rich troctolite (Interstitial		Troctolite (Interstitial)		Troctolite		Troctolite		Troctolite		Troctolite (Oikocryst)		Troctolite (Interstitial)	
n.	4	std	3	std	5	std	6	std	5	std	6	std	2	std
Li	2.3	0.4	5.99	2.98	1.29	0.60	7.14	-	1.15	0.78	1.04	0.68	1.11	0.09
B	1.3	-	11.03	2.29	-	-	3.70	1.61	1.39	0.01	1.37	-	1.10	-
Sc	88.5	5.32	92.26	1.30	80.0	5.97	91.04	4.69	80.0	4.42	88.56	1.75	95.57	5.16
TiO2	5351	1878	6256	65.8	0.39	0.02	3322	193	0.40	0.05	0.62	0.03	1.03	0.09
V	368	35.0	448	21.8	287	4.30	321	9.49	268	12.7	372	9	491	20.5
Cr	8630	158	4385	265	5649	268	8337	881	4769	944	2266	151	2014	138
Co	23.5	1.9	21.58	0.17	33.39	1.58	25.98	1.99	25.72	0.36	29.22	1.58	25.93	0.44
Ni	243	9.8	235	11.7	217	13.1	204	11.05	151	10.07	194	11.45	164	4.70
Zn	14.0	2.0	19.53	0.72	29.7	4.37	31.56	8.20	31.08	15.60	24.71	6.75	16.03	1.38
Rb	0.0	0.0	0.03	0.00	0.16	-	0.08	0.03	0.33	-	0.33	0.06	0.34	0.09
Sr	11.6	1.1	9.83	0.36	9.26	0.35	9.14	0.61	8.76	0.93	9.28	0.47	9.01	0.10
Y	26.9	6.4	49.36	1.60	11.50	0.78	19.5	2.56	13.16	1.33	20.62	1.78	38.32	0.58
Zr	48.9	25.0	128.91	4.38	8.17	0.75	23.9	5.08	10.73	3.57	14.23	3.01	96.49	0.96
Nb	0.4	0.1	0.07	0.05	0.06	0.00	0.10	0.06	0.22	0.11	0.17	0.08	-	-
Cs	-	-	0.01	-	0.01	-	0.01	-	0.04	-	-	-	0.02	0.01
Ba	0.0	0.0	0.12	0.00	0.12	0.05	0.04	0.02	-	-	-	-	0.38	-
La	0.5	0.1	0.26	0.04	0.16	0.03	0.22	0.05	0.19	0.06	0.26	0.11	0.36	0.15
Ce	3.6	0.8	2.45	0.21	1.04	0.15	1.49	0.12	1.17	0.24	1.68	0.19	2.33	0.33
Pr	0.9	0.3	0.85	0.02	0.27	0.03	0.42	0.07	0.29	0.04	0.43	0.07	0.54	0.03
Nd	6.4	2.0	7.18	0.18	1.98	0.37	3.19	0.41	2.38	0.67	3.59	0.65	4.86	0.83
Sm	3.0	1.0	4.07	0.27	1.08	0.12	1.70	0.30	1.22	0.39	1.88	0.49	3.43	0.74
Eu	0.8	0.1	0.73	0.08	0.41	0.05	0.60	0.11	0.40	0.12	0.56	0.20	0.50	0.13
Gd	4.3	1.5	6.71	0.16	1.71	0.25	2.31	0.28	1.84	0.36	2.81	0.29	4.90	0.25
Tb	0.8	0.3	1.33	0.07	0.37	0.02	0.49	0.03	0.35	0.04	0.64	0.14	1.13	0.11
Dy	5.5	1.7	8.90	0.38	1.99	0.22	3.51	0.45	2.59	0.64	3.38	0.54	7.23	1.89
Ho	1.1	0.3	1.86	0.09	0.43	0.02	0.75	0.07	0.53	0.12	0.85	0.10	1.63	0.07
Er	2.8	0.5	5.15	0.23	1.26	0.25	2.04	0.37	1.57	0.29	2.07	0.28	3.82	0.24
Tm	0.4	0.1	0.78	0.04	0.17	0.06	0.31	0.04	0.25	0.04	0.35	0.14	0.63	0.16
Yb	2.5	0.5	4.50	0.20	1.18	0.29	1.95	0.41	1.46	0.15	2.73	0.49	4.54	0.29
Lu	0.3	0.0	0.58	0.04	0.17	0.05	0.25	0.05	0.27	0.05	0.25	0.09	0.41	0.05
Hf	1.8	1.2	4.15	0.31	0.45	0.12	0.72	0.10	0.33	0.12	0.63	0.19	3.37	0.69
Ta	0.02	0.01	0.01	0.00	-	-	0.01	0.00	-	-	-	-	0.12	-
Pb	0.03	0.01	0.23	0.10	0.14	0.09	0.20	0.05	0.12	0.06	0.21	0.26	0.09	0.04
Th	0.04	0.01	0.02	-	0.01	0.00	0.02	0.01	0.03	0.01	0.02	0.01	0.02	-
U	0.02	0.01	0.01	-	0.01	0.00	0.01	0.00	-	-	0.02	0.02	-	-

Table 4: Trace element compositions of clinopyroxene (average values, ppm).

Clinopyroxene												
PI33		PI49		P19		PI32		PI34		PI18		
Troctolite (Interstitial)		Troctolite		Troctolite		Ol-gabbro		Ol-gabbro		Ol-gabbro		
8	std	3	std	4	std	7	std	13	std	2	std	
1.18	0.49	5.27	-	1.96	0.79	2.20	1.77	1.39	0.47	1.06	0.38	
1.92	0.57	4.16	-	-	-	3.40	1.08	1.25	-	-	-	
93.52	3.63	81.72	0.90	79.92	2.25	85.80	3.91	81.30	3.26	90.03	1.12	
0.87	0.02	2345.24	233.97	2184.73	47.06	2271	220	2178	138	2943	98.7	
451	14.44	269.98	8.48	264.92	6.46	280.03	23.98	273	14	288	8.05	
5042	231.08	6688.39	109.35	7333.62	503	7169	1907	6859	1946	7092	512	
30.45	2.29	28.16	2.58	27.20	1.29	32.77	3.69	30.0	1.57	31.70	0.66	
259	21.18	190.90	17.91	184.03	15.51	208.86	20.92	195.63	12.80	196.02	4.62	
44.21	19.61	23.11	2.75	26.37	1.52	26.05	1.98	29.60	8.74	23.37	0.12	
0.38	0.20	0.06	0.03			0.06	0.03	0.26	0.16	-	-	
10.61	0.76	9.09	0.46	10.81	0.36	10.42	0.46	10.28	0.69	10.70	0.54	
26.67	2.20	14.90	0.28	9.62	0.45	12.17	1.53	11.26	1.21	11.81	0.11	
26.53	5.91	20.79	3.77	7.18	0.96	8.88	3.03	7.54	1.05	7.75	0.49	
0.12	0.02	0.11	0.02	0.02		0.02	0.01	0.06	0.04	0.02	-	
0.03	0.01	-	-	0.02	0.01	0.01	-	0.02	0.02	0.01	-	
0.60	0.34	0.10	0.05	0.11	0.06	0.07	0.02	0.23	0.11	0.05	0.00	
0.33	0.10	0.13	0.03	0.13	0.03	0.15	0.04	0.16	0.05	0.17	0.03	
1.96	0.14	0.89	0.07	0.82	0.05	0.94	0.22	1.01	0.22	1.03	0.03	
0.55	0.09	0.28	0.02	0.21	0.03	0.28	0.06	0.25	0.05	0.25	0.03	
3.87	0.42	1.88	0.33	1.66	0.24	1.93	0.33	1.89	0.27	2.12	0.20	
2.52	0.62	1.22	0.12	0.87	0.16	1.06	0.28	1.04	0.30	1.19	0.05	
0.65	0.14	0.46	0.07	0.39	0.07	0.46	0.09	0.38	0.07	0.44	0.02	
3.62	0.54	1.95	0.13	1.44	0.29	1.68	0.39	1.57	0.33	1.85	0.33	
0.72	0.13	0.35	0.02	0.28	0.06	0.35	0.08	0.31	0.06	0.34	0.06	
5.23	0.52	2.62	0.34	1.97	0.33	2.23	0.36	2.11	0.26	2.58	0.14	
1.10	0.09	0.63	0.03	0.44	0.02	0.52	0.05	0.43	0.08	0.52	0.06	
2.86	0.51	1.64	0.30	0.97	0.19	1.28	0.15	1.21	0.14	1.34	0.08	
0.40	0.09	0.26	0.04	0.13	0.05	0.17	0.02	0.18	0.01	0.20	0.01	
3.13	0.43	1.57	0.08	1.18	0.27	1.15	0.11	1.19	0.18	1.33	0.06	
0.36	0.08	0.22	0.01	0.13	0.01	0.16	0.05	0.15	0.02	0.13	0.03	
1.13	0.31	0.58	0.17	0.43	0.10	0.46	0.12	0.36	0.15	0.39	0.01	
-	-	0.01	-	-	-	0.01		0.06	0.03	-	-	
0.47	0.24	0.24	0.04	0.44	0.40	0.16	0.09	0.52	0.93	-	-	
0.02	0.01	0.02	-	-	-	0.01	0.00	0.02	0.00	-	-	
0.01	0.00	0.01	-	-	-	-	-	0.01	0.00	-	-	

Table 4: continued